Characterization and modeling of low frequencies noise in bipolar transistors developed in BiCMOS technology (55 nm node) for RF to THz applicationsés en technologie BiCMOS (nœud 55 nm) pour des applications RF et THz.

Johnny El Beyrouthy

THÈSE POUR OBTENIR LE GRADE DE DOCTEUR DE L'UNIVERSITÉ DE MONTPELLIER

En Électronique

École doctorale I2S

Unité de recherche IES UMR 5214

Characterization and modeling of low frequency noise in bipolar transistors developed in BiCMOS technology (55 nm node) for RF to THz applications

Présentée par Johnny EL BEYROUTHY
Le 07 Décembre 2020

Sous la direction de Fabien PASCAL
et Bruno SAGNES

Devant le jury composé de

Cristell MANEUX, Professeur, Université de Bordeaux	**Rapporteur**
Michel PRIGENT, Professeur, Université de Limoges	**Rapporteur**
Sébastien HAENDLER, Ingénieur, STMicroelectronics Crolles	**Examinateur**
Jérôme BOCH, Professeur, Université de Montpellier	**Président du jury**
Fabien PASCAL, Professeur, Université de Montpellier	**Directeur de thèse**
Bruno SAGNES, Maître de conférences, Université de Montpellier	**Co-directeur de thèse**

UNIVERSITÉ DE MONTPELLIER

Acknowledgment

After three years of work, I would like to thank all those who contributed, from near or far, to the realization of this project.

This thesis was carried out at the Institute of Electronics and Systems IES, University of Montpellier, as part of a European project in close collaboration with STMicroelectronics, Crolles.

This work was established in the frame of the TARANTO H2020 ECSEL project, co-funded by the French Ministry of Economy, Finance and Industry and the European community. Furthermore, the University of Montpellier PRESERVE platform, in which an important part of the thesis was initiated, was funded thanks to the financial support of the Region Occitanie and the European Regional Development Fund.

First, I would like to thank my thesis director Mr. **Fabien Pascal** and co-director Mr. **Bruno Sagnes** for their support, trust and guidance throughout these three years. In addition to their scientific support, despite their busy schedule, they always made themselves available to advise me during the elaboration of this thesis. However, their advice and suggestions were never overlapping with my freedom of action through each stage of this project, and for that I am grateful. Their guidance allowed me to grow and develop many skills on several levels, for which I am appreciative.

This work presented multiple collaborations with the RADIAC group in IES laboratory and the PUISSANCE group in IEMN laboratory to cover some of the established studies. In this context, I would like to thank **Christophe Gaquière**, **Etienne Okada**, and **Vanessa Avramovic** from the IEMN laboratory meanwhile **Jérôme Boch** and **Tadec Marein** from the IES laboratory.

During these years, I was part of the M@CSEE group at the IES laboratory. In this regard, I would like to thank the group's members with whom I was able to establish scientific discussions during this period. In particular, I would like to thank some of my team members **Rodolphe**, **Bastien**, **Joanna**, **Sébastien**, and **Maroua** for their remarkable support and assistance, both material and moral, that allowed me to succeed this thesis in good conditions.

Moreover, I thank all my friends back home in Lebanon, in Canada and the ones I was lucky enough to meet in France for their welcome, their friendship and their good humor. Their presence has given me the strength and the motivation to keep moving forward.

Finally, saving the best for last, I am most grateful for my family's support and love. Although no words can describe my gratitude, I address all my affection to my parents, my brother and both my sisters. Thank you for being always there for me despite the distance.

Table of contents

General introduction 15

Chapter 1 Low-Frequency Noise sources in bipolar transistor 19

1.1 Introduction 20

1.2 Low-Frequency Noise components in the bipolar transistors 21

1.2.1 White noise 21

1.2.1.1 Thermal noise 21

1.2.1.2 Shot noise 21

1.2.2 Excess noise 22

1.2.2.1 Generation-Recombination noise 22

1.2.2.2 RTS noise 23

1.2.2.3 Flicker noise (1/f noise) 23

1.3 Physical models of the excess noise sources in bipolar transistors 25

1.3.1 1/f noise physical models 25

1.3.1.1 I_B^2 models 25

1.3.1.1.1 Superposition of Generation-Recombination 25

1.3.1.1.2 Two-step tunneling model 26

1.3.1.1.3 Tunneling fluctuation model 27

1.3.1.1.4 Tunneling assisted trapping model 27

1.3.1.1.5 Surface noise due to carrier density fluctuations 27

1.3.1.1.6 Random walk model 28

1.3.1.2 I_B models 28

1.3.2 G-R physical models 29

1.4 Compact model of the excess noise sources 30

1.4.1 1/f SPICE model 30

1.4.2 G-R SPICE model 31

1.5 State of art of LFN for Si-Bipolar transistors 32

1.5.1 Si BJTs 32

1.5.2 Si PE-BJTs 32

1.5.3 Si/SiGe HBTs 33

1.6 Conclusion 34

Chapter 2 Test bench and Low-Frequency Noise measurements of Si/SiGe:C HBTs 37
2.1 Introduction 38
2.2 Low-Frequency Noise bench test 39
2.3 Studied technologies 41
2.3.1 Collector structures: HS, MV, HV 42
2.3.2 Dopant activation methods 43
2.4 HBTs configuration 44
2.5 DC characterization 46
2.5.1. Base current components 47
2.5.1.1 Generation-recombination current 47
2.5.1.2 Tunnel current 48
2.5.1.3 Diffusion current 48
2.5.1.4 High injection effects 49
2.5.2 DC results and analysis of the B55 comparing to the BiCMOS9MW 49
2.5.2.1 Comparison of the three collector structures 49
2.5.2.2 Performances of the B55 TH and DSA, comparison with BiCMOS9MW 50
2.6 Low-Frequency Noise: Spectral analysis 51
2.7 Dispersion effect on similar HBT geometries 53
2.8 Characterization and modeling of the input excess noise components 56
2.8.1 Spectral behavior 56
2.8.2 1/f noise analysis 58
2.8.2.1 Analysis in response to the collector structures 58
2.8.2.2 Analysis of the two flavors of the B55 compared to the BiCMOS9MW 60
2.8.2.2.1 1/f noise study as a function of I_B 61
2.8.2.2.2 1/f noise study as a function of A_E 61
2.8.2.2.3 1/f study as a function of P_E/A_E ratio 62
2.8.2.3 Localization of the 1/f noise source 63
2.8.2.4 Figure-Of-Merit fc/ft 64
2.8.3 G-R components analysis 66
2.8.3.1 G-R analysis 67
2.8.3.1.1 Plateau analysis in response to emitter geometries 68
2.8.3.1.2 Plateau magnitude analysis in response to I_B 69

2.9 Conclusion 71

Chapter 3 Heterojunction Bipolar Transistors response after exposure to radiative environments 74

3.1 Introduction 75

3.2 Radiation environments impact 75

3.2.1 Description of radiative environments 75

3.2.2 Interaction mechanism with the materials 77

3.2.3 Irradiation impact on electronics 78

3.3 Radiation facilities 79

3.4 Studied HBTs 80

3.5 X-ray Irradiation impact on HBTs 81

3.5.1 Time interval and measurement impacts on DC and LFN measurements 81

3.5.2 Methodology of the irradiation process 83

3.5.3 DC characteristics for the irradiated HBTs 83

3.5.3.1 Gummel-plot analysis 84

3.5.3.2 Discussion on the degradation impact 86

3.5.4 Low-Frequency Noise measurements for stressed HBTs 87

3.5.4.1 S_{IB} response towards X-ray exposure 87

3.5.4.2 Impact of TID on the 1/f noise 89

3.5.4.2.1 1/f noise study as a function of I_B 90

3.5.4.2.2 1/f noise study as a function of A_E 91

3.5.4.2.3 1/f noise study as a function of P_E 92

3.5.4.3 Impact of TID on G-R component 94

3.5.4.3.1 Cut-off frequency study 94

3.5.4.3.1.1 Cut-off frequency evolution of initial G-R as a function of TID 94

3.5.4.3.1.2 Comparison of initial versus induced cut-off frequencies 96

3.5.4.3.2 G-R plateau magnitude study 96

3.5.4.3.2.1 Plateau magnitude evolution of initial G-R as a function of TID 96

3.5.4.3.2.2 Comparison of initial and induced plateau magnitudes 97

3.5.4.3.2.3 Plateau magnitudes evolution in response to the geometrical parameters 98

3.5.4.3.2.4 Plateau magnitudes evolution in response to I_B 99

3.5.5 Annealing response after X-ray exposure 101

3.5.5.1 Time effect before annealing 101
3.5.5.2 Thermal annealing effect 101
3.5.5.2.1 DC analysis 102
3.5.5.2.2 LFN analysis 103
3.6 Irradiation impact on both High-Frequency and Low-Frequency domain 103
3.6.1 HF analysis 104
3.6.2 LF analysis at high current bias 105
3.7 Irradiation impact of the Cobalt60 source on HBTs 106
3.7.1 Methodology 106
3.7.2 DC characteristics for the irradiated HBTs 107
3.7.2.1 Gummel plot analysis 107
3.7.2.2 Discussion 108
3.7.3 Low-Frequency Noise measurements of stressed HBTs 109
3.7.3.1 S_{IB} response after exposure to Gamma-ray 109
3.7.3.2 Impact of TID on the 1/f noise 110
3.7.3.2.1 Irradiation response of the 1/f noise level as a function of I_B 111
3.7.3.2.2 Irradiation response of the 1/f noise level as a function of A_E 112
3.7.3.2.3 Irradiation response of the 1/f noise level as a function of P_E 114
3.7.3.3 Impact of TID on G-R component 115
3.7.3.3.1 Cut-off frequency study 115
3.7.3.3.1.1 Evolution of initial G-R components depending on I_B 115
3.7.3.3.1.2 Evolution of initial G-R component depending on A_E 116
3.7.3.3.1.3 Comparison of initial versus induced cut-off frequencies 117
3.7.3.3.2 G-R plateau magnitude study 117
3.7.3.3.2.1 Plateau magnitude evolution of initial G-R as a function of TID 117
3.7.3.3.2.2 Comparison of initial and induced plateau magnitudes 118
3.7.3.3.2.3 Plateau magnitudes evolution in response to A_E 119
3.7.3.3.2.4 Plateau magnitudes evolution in response to P_E 120
3.7.3.3.2.5 Plateau magnitudes evolution in response to I_B 120
3.7.4 Annealing response after Gamma-ray exposure 121
3.7.4.1 Time effect before annealing 122
3.7.4.2 Thermal annealing effect 122

3.7.4.2.1 DC analysis 122
3.7.4.2.2 LFN analysis 123
3.8 Comparison of X-ray and Gamma ray impacts on HBTs 124
3.8.1.1 Comparison of the DC characterization 124
3.8.1.2 Comparison of the LFN characterization 127
3.8.1.2.1 1/f noise analysis 127
3.8.1.2.2 G-R analysis 128
3.9 Conclusion 128
General conclusion 131
Perspectives 134
ANNEX 135
References 140
Publications 151

General introduction

This thesis derives from the European TARANTO H2020 ECSEL project co-funded by the French Ministry of Economy, Finance and Industry and the European Community. It was initiated in April 2017. This project is a sequence of a previous European CATRENE project called RF2THZ Si-SOC initiated in 2012.

The aim of this project is to establish an advanced BiCMOS technology platform with improved Si/SiGe:C HBT performances and interaction levels. The devices derive from two BiCMOS technology issued from a 130 nm CMOS node for mm-waves application developed by Infineon and IHP and from a 55/28 nm CMOS node for high integrated RF applications developed by STMicroelectronics.

Three work packages were highlighted in the context of the project distributed on 33 European partners among research laboratories and industries. The first work package is responsible for the technological development process to provide the next generation of the BiCMOS technology. The aim of this process is to reach bipolar transistors frequency responses above 400 GHz. The second work package corresponds to TCAD simulations, characterization and compact modeling (HICUM) for the developed technology where the IES laboratory is actually involved. TCAD simulations as well as compact models allowed defining the accuracy and the reliability of the investigated components. While the third work package handled ICs designing processes for smart systems and test systems. The ICs blocks built are designed for mobile communication, front end transceiver, IOT smart sensing, automotive radars, etc.

The topic of this thesis derives from the second work package more precisely the characterization and the modeling section. The established characterizations are narrowed on DC electrical characterization and especially on Low-Frequency Noise measurements. One of the requested objectives is to evaluate the technological advancement of the newest STMicroelectronics BiCMOS generation with a 55 nm CMOS node known as the B55. To evaluate this technological advancement, a previous mature generation known as the BiCMOS9MW will be stated as a reference in this study. The second objective of the thesis presents a new field of study for the Low-Frequency Noise team where the impact of X-ray and γ–ray irradiations will be investigated on the two BiCMOS technologies. This study leads to characterize and model the induced defects and to highlight the behavior of the bipolar transistors in extreme environment conditions.

To result the established work during this thesis, three chapters will be depicted. The first chapter will present a general introduction of the Low-Frequency domain, the multiple noise components/sources found in semiconductor devices will be presented. Through the literature, several physical noise models were deduced while investigating the noise components. Hence, the physical models of the excess noise, 1/f and Generation-Recombination components, will be listed by focusing on the 1/f noise which is considered the main investigated noise component in the Low-Frequency domain. Furthermore, compact models describing the two excess noise components will be introduced. The 1/f compact model, known as SPICE model, is highly needed

by circuit designers in the study of the up-conversion phenomenon. The parameters' extraction will be briefly introduced for both 1/f and G-R compact model. Eventually, a state of art of the established research will be resumed to point out some of the element conclusion concerning the bipolar transistors in this field of study.

The second chapter will be initiated by a description of the employed test bench needed to establish a proper Low-Frequency noise measurement. The investigated bipolar transistors compatible with the 55 nm CMOS node issued from the BiCMOS technology will be the main devices studied in this thesis. An overview of some of the technological developments that highlights the distinct behavior of the newest BiCMOS generation will be listed. Two technological developments, responsible for the fabrication of several devices' types, will be detailed. The heterojunction bipolar transistors characterization is systematically established by a DC electrical characterization followed by a noise measurement. Experimental results will be presented in this chapter to distinct the technological developments impact on the performance of the 55 nm BiCMOS technology. The established study will be divided into two categories based on two developed technological parameters. Alongside, the previous mature technology with a 130 nm CMOS node, BiCMOS9MW, will be taken as a reference to compare the devices performances. Analysis of each excess noise component will be examined as a function of emitter geometries and current bias to extract the compact models' parameters. Moreover, Figures-Of-Merit, for both static and Low-Frequency Noise measurements, will be extracted to compare their frequency response and comment the technological advancement of the BiCMOS technology. Based on the literature and experimental studies, the localization of the excess noise components will be introduced as a discussed subject in this chapter.

Moving toward the third chapter, the reliability and the tolerance of BiCMOS technologies will be challenged by exposing these technologies to extreme environment conditions. These conditions will be generated through exposing the technologies to radiative environments: X and Gamma irradiations. These conditions will be imposed by two irradiation sources, an X-ray generator and a Cobalt60 source. The irradiation sources are located at the IES facility in the PRESEVE platform that was funded thanks to the financial support of the Occitanie Region and the European Regional Development Fund. The content of this chapter will present the novelty which discriminate the established work in this thesis. At first, an introduction to the irradiation domain presenting multiple irradiation types that occur in a radiative environment will be given. The degradation mechanisms induced by the irradiation exposure of semiconductor devices will be presented. A particular interest for some of the degradation mechanisms will occur based on the ones generated by the two irradiation sources employed. The two BiCMOS technologies, 55 nm and 130 nm CMOS node, were exposed to each source while respecting a proper irradiation process. This study was initiated by the X-ray irradiations to select an experimental process that will be respected during the entire irradiation procedure. The irradiation processes were maintained till a well-defined Total Ionizing Dose (TID). Both electrical characterization and noise measurements were investigated in response to the irradiation exposure. The irradiation response will be investigated as a function of several technological parameters and bias conditions and will allow to highlight the defected area of each technology. Each irradiation exposure will be followed by an annealing process to uncover any possible healing effect for the induced defects. This process

will investigate two distinct annealing mechanisms. Eventually, a comparison of the induced degradation mechanisms by each irradiation source will be investigated.

Chapter 1 Low-Frequency Noise sources in bipolar transistor

1.1 Introduction

The recent explosion in wireless and information technologies was one of the most dramatic applications of the semiconductor technology in the past decade. Therefore, it was necessary to develop more efficient and reliable devices and circuits. The Low-Frequency Noise (LFN) analysis is an important study that needs to be examined for analog and RF applications. Moreover, due to its sensitivity, LFN is a very convenient tool used as reliability and quality indicators for technologies.

LFN plays a major role in the deterioration of the spectral purity in frequency sources and mixer circuits (i.e. up-conversion phenomenon). The noise investigation presents a major drawback of a good quality telecommunication system. Therefore, major interests were highlighted by circuit designers during the design process of specific circuits (frequency shifters, VCO, mixers, low noise amplifiers …). During the development of a technology, LFN is used by engineers as a tool to locate the sensitive area of the devices. Moreover, researchers developed several physical models for the noise sources in the bipolar transistors to identify and locate their physical origins. By understanding the noise origins, strategies can be developed to decrease their level and reduce their impact on the circuit.

LFN sources were highly investigated by different research groups for several years. This chapter aims to present the basic information of the LFN domain. Therefore, as a start, the noise components found in semi-conductor materials and devices will be generally introduced while focusing on bipolar transistors. The examined noise components are sorted in two categories: white noise and excess noise. These noises will be listed in the first section of this chapter along with their physical origins.

Concerning the excess noises, the biggest part of the LFN literature study is mainly focused on the 1/f noise. Therefore, 1/f noise components in bipolar transistors will present the biggest part of interest that will be examined in this chapter. Unlike the 1/f noise component, the Generation-Recombination (G-R) noise component is not always present in semiconductor materials and devices especially in Si based bipolar transistors. Thus, in the literature, this noise component is not as studied as the 1/f noise. The fact remains that its study constitutes an essential element in a global approach to low frequency noise. In particular, the G-R noise analysis can provide useful information concerning the defects (trap centers) in semiconductors materials and devices.

Next section outlines the physical noise models that were suggested respectively for the examined excess noise sources in bipolar transistors. The 1/f noise and in a lesser extend G-R noise physical models are presented in particular to their current and geometrical dependency.

Last section will initiate the bipolar compact models that are used by circuit designers. Two models will be introduced respectively for the 1/f noise and the G-R components.

Eventually, a summary of several studies will be given to resume some of the previous LFN investigations that were established in the state of art of bipolar transistors. The published conclusions were investigated on both homo junction and poly-emitter bipolar Si transistors (Si BJTs, Si PE-BJTs) and on Si/SiGe heterojunction bipolar transistors (Si/SiGe HBTs).

1.2 Low-Frequency Noise components in the bipolar transistors

Noise in electronic materials and devices result from the random fluctuation of charges induced by several interactions that can disturb the motion of carriers. Since it is an undesirable phenomenon, we are interested in reducing its influence. The attributed noise response sets a lower limit to the sensitivity and accuracy of the circuit.

The low-frequency noise in electronic devices, especially in bipolar transistors, occurs from several noise sources [1][2][3][4]. The examined noise sources are divided into two categories: white noise and excess noise. Contrarily to the excess noise, the white noise is a non-dependent frequency noise which set the lowest level that can be measured by the system.

1.2.1 White noise

The white noise is given by fundamental physical laws without any possible way to extinct completely. The two noise sources that consist the white noise are the thermal noise and the shot noise.

1.2.1.1 Thermal noise

Thermal noise is also known as Nyquist noise or Johnson noise. It was initially explored by J.B. Johnson published in 1927 [5] then was theoretically expressed by H. Nyquist in 1928 [6]. This effect is due to a random carrier's motion resulting from the thermal agitation in the conductor's material. The engendered current presents a negligible mean value contrarily to its fluctuation current value. The voltage and current noise sources are presented by Nyquist in eq. 1.1 and 1.2respectively as:

$$\overline{v_{th}^2} = 4kTR\Delta f \qquad 1.1$$

$$\overline{i_{th}^2} = \frac{4kT\Delta f}{R} \qquad 1.2$$

where k is the Boltzmann constant equals to 1.38 10^{-23} J/K, R is the resistance access, T is the temperature of the conductor and Δf is the band frequency.

The power spectral density of voltage and current fluctuation are respectively expressed as followed [7]:

$$S_v = 4kTR \qquad 1.3$$

$$S_I = \frac{4kT}{R} \qquad 1.4$$

In bipolar transistors, thermal noise is usually associated to access resistances of the emitter, base and collector, S_{vRE}, S_{vRB}, S_{vRC} respectively.

1.2.1.2 Shot noise

Shot noise known as Schottky noise was discovered by Schottky in 1918 [8]. This noise component is generated by the charge carriers overcoming the potential barrier and flowing in an uncorrelated manner. The current spectral density is presented as:

$$S_I = 2qI \quad 1.5$$

More specifically, in bipolar transistors, it is caused by two mechanisms : the fluctuation of majority carriers diffusing through the transistor junctions and their recombination with the minority carriers [9][10]. The base current shot noise outcomes from the flow of holes (majority carriers in p doped area) across the E-B junction and the recombination of electrons (minority carriers) in E-B space charge region. While the collector current shot noise results from the diffusion of electrons (majority carriers in n doped area) and the recombination of holes in C-B space charge region. Base and collector current shot noise are presented in equation 1.6 and 1.7 respectively:

$$S_{IB} = 2qI_B \quad 1.6$$

$$S_{IC} = 2qI_C \quad 1.7$$

1.2.2 Excess noise

The excess noise is associated to the fluctuation of the conductivity. Noise sources can originate from structural or induced defaults, such as crystalline deformations, impurities located in the semiconductor structure, at the interface of semiconductor layers or semiconductor-oxide layers. Since the origins of these noise sources are mainly induced by defaults, they are more likely to be reduced by improving, for instance, the materials quality and the fabrication process.

The examined noise sources are related to Generation-Recombination components (G-R), Random Telegraph Signal noise (RTS) and flicker noise (1/f noise). These noises are related either to the fluctuation of the charge carriers' number (Δn, Δp) or to the fluctuation of carrier's mobility (Δμ).

1.2.2.1 Generation-Recombination noise

G-R noise results from the fluctuation in the number of free carriers (electrons and holes) associated with erratic charge carriers transition between the conduction band and an energy level localized in the energy gap [11]. This noise is due to a trapping/de-trapping behavior of the carriers. The interpretation of G-R noise in semiconductors started from 1951. Since then, many experiments and theories were developed. The spectral density of G-R noise was modeled as given in [12] by the following equation:

$$\frac{S_N(w)}{N_0^2} = \frac{\overline{\delta N^2}}{N_0^2}\frac{4\tau_N}{1+(\omega\tau_N)^2} \quad 1.8$$

where $\overline{\delta N^2}$ is the variance of carrier number fluctuation, N_0 the average number of free carriers and τ_N the carrier life-time.

The spectroscopy of the G-R noise is described by a Lorentzian shape with a maintained noise level (plateau) until a cut-off frequency, $f_{ci} = \frac{1}{2\Pi\tau_N}$, where the noise level decreases respecting a slope value of 2.

Carriers lifetime are composed of both generation and recombination time. The generation time provides information concerning the characteristic of the traps while the recombination time

provides some information on the scattering cross section. By analyzing the G-R components, several trap centers can occur presenting distinct trap signatures each defined by an unique magnitude and cut-off frequency.

1.2.2.2 RTS noise

Random telegraph signal (RTS) noise presented a part of study in the LFN domain since early seventies [13] and eighties [14]. Several physical origins were suggested to investigate this noise sources by Strasilla, Strutt and others. Nevertheless, the presented physical origins in this part was proposed by Kleinpenning in [15]. This noise is due to the fluctuation of carrier's number that depicts the capture and the emission of an electron by an active trap level [16]. Trap levels located to far from the Fermi level present are either full or empty trap centers and are inactive traps. Hence, RTS noise is described as a function of bias conditions and temperature illustrated as a Lorentzian spectral given as:

$$\frac{S_N}{N_0^2} = \frac{S_I}{I^2} = \frac{S_v}{V^2} = K\frac{4\tau_N}{1+(2\Pi f\tau_N)^2} \qquad 1.9$$

where τ_N is the relaxation time in the correlation function that depends on the average of time capture τ_c and time emission τ_e with $\frac{1}{\tau_N} = \frac{1}{\tau_c} + \frac{1}{\tau_e}$ and K equals to $K = \frac{1}{N_0^2}\frac{\tau_N}{\tau_e+\tau_c}$.

In the time domain, RTS noise is presented as a square signal defined by time capture, time emission and the amplitude of current fluctuation ΔI_B. Figure 1.1 illustrates the RTS signal depicting multiple trap levels found during this work in a Si/SiGe HBT.

In Si bipolar transistors, RTS noise was observed and reported by several authors [17][18] mainly on Si PE-BJTs and Si/SiGe HBTs with the down scaling of the dimensions.

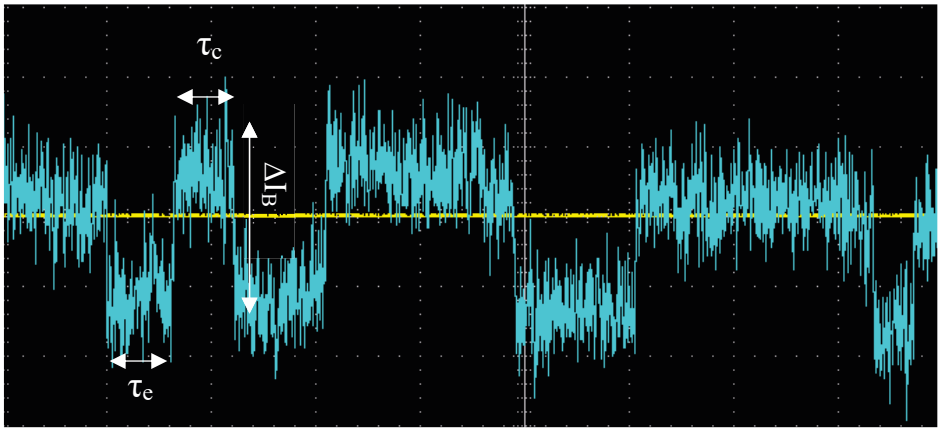

Figure 1.1. RTS noise signals specification in time domain.

1.2.2.3 Flicker noise (1/f noise)

The 1/f noise, described by its own name, derives from the inversely proportionality of the spectral density as a function of the frequency. This proportionality is observed at low frequencies mainly below 1 kHz. Previous studies recorded an extraction of the 1/f noise for extremely low

frequency values in the order of some μHz [19][20]. It is generated by the fluctuation of the material's conductivity given by relation 1.10:

$$\sigma = q\mu n \qquad 1.10$$

Hence, its physical origin can occur from the fluctuation of the carriers' mobility μ and/or carriers' number n. The most common theory commenting the 1/f noise was established by MC Whorter in 1959 [21] which predicts that the 1/f noise is based on a carriers recombination phenomenon depicted by the superposition of several G-R components (surface state theory). The Mc Whorter theory is illustrated in Figure 1. 2.

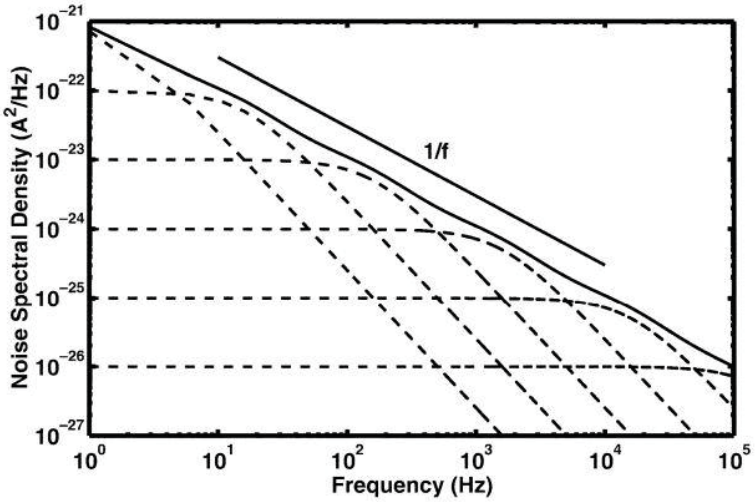

Figure 1.2. Superposition of Lorentzian presenting an 1/f noise [10]

Twenty years after, based on experimental investigations, Hooge proposed an empirical relation with a theoretical approach based on the fluctuation of the mobility and not the number of charge carriers [22]. The mobility was investigated as a function of two scattering mechanisms, impurity and lattice scattering, expressed in 1.11 which concluded that only the lattice scattering is responsible of the 1/f noise in the conductivity [23].

$$\frac{1}{\mu} = \frac{1}{\mu_{imp}} + \frac{1}{\mu_{lattice}} \qquad 1.11$$

1/f noise spectrum is only found if the carrier's diffusion through the traps respects specific conditions. For electrons, the transitions between the conduction band and the different trap levels should be directly established without any transition between the different trap levels neither directly nor through the conduction band [24]. Figure 1.3 presents the different carrier's transitions that result the difference between the 1/f and the Lorentzian spectrum.

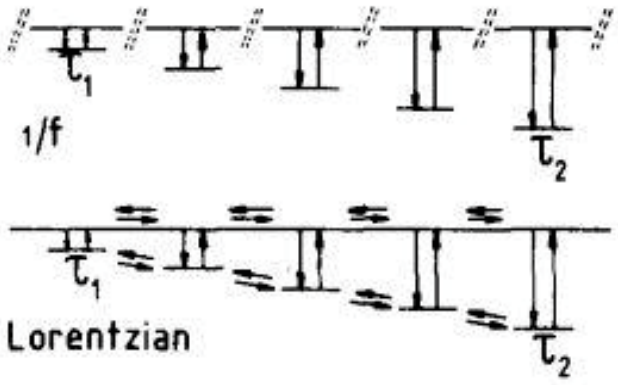

Figure 1.3. Carrier's transition difference between the 1/f noise level and the G-R component [24].

In the literature, the physical origin of the 1/f noise remains the main investigated topic in the LFN domain. Several physical models were published to extract the physical origin of this noise sources that will be listed in section 1.3.

1.3 Physical models of the excess noise sources in bipolar transistors

1.3.1 1/f noise physical models

The physical origin and location of the 1/f noise sources was an active research subject for a long period. Several models were proposed for Si materials to measure the low-frequency noise spectral density in bipolar components. These models are sorted into two parts based on the 1/f noise level dependency on the base current I_B. These models are also described by other parameters such as the emitter surface A_E and the temperature T.

The first section presents models based on a quadratic evolution with I_B (I_B^2) of the S_{IB}. This behavior was mainly detected in the advanced Si/SiGe transistors. On the contrary, the second category is based on an I_B evolution of the S_{IB} level. These models are based on former models known as McWhorter model in terms of carriers number fluctuations [25] and Hooge model in terms of mobility fluctuation [26].

However, the second category of these models were found to be negligible in the advanced Si/SiGe technologies. Therefore, the main interest will be given for the first section for the models describing an I_B^2 and $1/A_E$ dependency.

1.3.1.1 I_B^2 models

1.3.1.1.1 Superposition of Generation-Recombination

In accordance with the experimental results published in [27][28], a model based on the superposition of the G-R components was suggested [29]. This model is considered as the recent model proposed for Poly-emitter bipolar transistors in 2001. The input current spectral density is given by the following model:

$$\frac{S_{IB}}{I_B^2} = \frac{K_F N_{T,dec}^*}{A_E f} \qquad 1.12$$

where $N^*_{T,dec}$ is the number of traps per unit area per frequency decade, A_E is the emitter area, f is the frequency and K_F presents the extracted noise level.

K_F is an empirical parameter, it depends on the operating and physical details of the transistor. A dependency to the I_B^2 and a $1/A_E$ dependency can be concluded from this model.

1.3.1.1.2 Two-step tunneling model

The interpretation of the two-step tunneling modeling has allowed the explanation of the tunnel diode phenomenon in low-frequency noise domain [30]. The first step is a recombination behavior of carriers from the semiconductor bands to states at the interface SiO_2 layer near the mono-crystalline silicon. This behavior describes the Shockley-Read-Hall process. As for the second step, it's described by an elastic tunneling behavior of the carriers from the interface states into the states located in the oxide. Carriers' lifetime in the SiO_2 are quite important comparing to the carrier's lifetime at the interface Mono-Si/SiO_2. These mechanisms are illustrated in Figure 1.4.

The current spectral density was modelled as:

$$\frac{S_{IB}}{I_B^2} \approx \frac{q^4}{ln[\frac{\tau(x_0)}{\tau(0)}]2k\varepsilon_{ox}^2} \frac{N_T t_{ox}^2}{TA_E^* f} \qquad 1.13$$

where t_{ox} is the oxide thickness, T is the absolute temperature and N_T corresponds to the trap's density per unit area and energy interval ($cm^{-2}eV^{-1}$). A_E^* presents a fraction of the emitter area since the tunneling behavior occurs through the thinnest part of the oxide. This parameter takes place for PE-BJT devices with a nonuniform grown oxide thickness that was experimented in [31]. A recent study established in [32] has depicted the Si/SiGe HBTs using the given model in eq. 1.13. I_B^2, $1/A_E$, 1/T, t_{ox}^2 and N_T dependencies were highly respected.

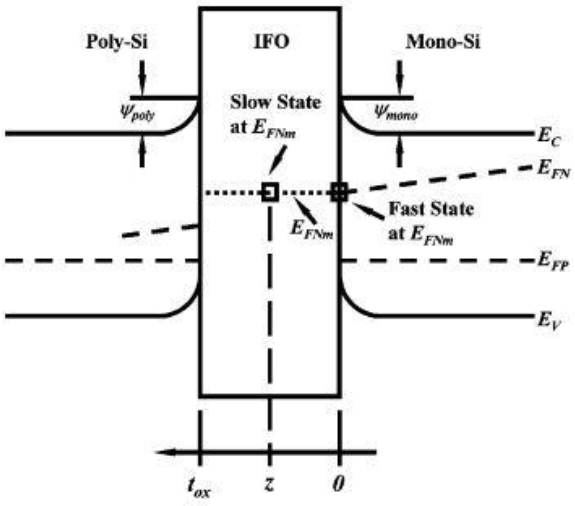

Figure 1.4. Two-step tunneling model at the Interface oxide (IFO) of a p-n-p component [32].

1.3.1.1.3 Tunneling fluctuation model

The tunneling fluctuation model was developed by Markus and Kleinpenning earlier in 1995 [33]. The thermal noise was found to be responsible of the potential barrier height and thus controlling the tunneling probability of the carriers [34]. The model is given by:

$$\frac{S_{IB}}{I_B^2} = \frac{1}{[1+\sqrt{\frac{kT}{2\Pi m_p}}T_{P,ox}(\frac{1}{s_m}+\frac{W_m}{D_m}+\frac{W_p}{D_p})]^2}\frac{4\Pi q k m_p \tan\delta}{3h^2}\frac{t_{ox}^3 T}{f\varepsilon_{ox}V_0 A_E} \quad 1.14$$

where m_p is the effective mass of holes, $T_{P,ox}$ the tunneling probability of holes through the oxide layer, s_m presents the recombination velocity of holes in the metal, $W_{m,p}$ and $D_{m,p}$ are the width and the diffusivity of holes in the monosilicon and polysilicon layer, V_0 is the barrier height, $\tan\delta$ is the loss tangent of the oxide and ε_{ox} the dielectric constant of the oxide layer.

1.3.1.1.4 Tunneling assisted trapping model

The base current consists of a surface and a volume recombination components [35] that is expressed as followed;

$$I_B = I_{v0}[exp(\frac{qV_{BE}}{kT})-1] + I_{s0}[exp(\frac{qV_{BE}}{nkT})-1] \quad 1.15$$

where kT/q is the thermal voltage, n is the ideality factor (n≈2), I_{v0} and I_{s0} are the volume and surface saturation currents.

The tunneling assisted trapping model was developed in 1996 by Mounib [36]. The 1/f noise is based on a surface recombination base current component. A trapping/de-trapping mechanism located in the spacer oxide at the periphery of the emitter-base junction relates to the noise model. Hence, the spectral density of the base current noise is expressed by:

$$\frac{S_{IB}}{I_S^2} = \frac{q^4\lambda}{kC_{SC}}\frac{N_T^*}{T(PW_{SC})f} \quad 1.16$$

where I_s is the surface recombination current, W_{SC} is the width of the E-B space charge region, C_{SC} is the semiconductor surface capacitance per unit area, λ is the attenuation tunneling distance and N_T^* is the oxide slow state volume density.

The surface recombination current (I_S) examined is not equal to the recombination current component (I_B). Experimental results have presented complexities while extracting the I_S values [37]. Meanwhile, other studies have suggested that $I_S = 0.5\, I_B$ and the other half of the I_B can be related to recombination components in the mono silicon emitter [31].

1.3.1.1.5 Surface noise due to carrier density fluctuations

This model developed in [38] presents the 1/f noise as a carriers density fluctuation near the interface Si-SiO_2 through fast surface states. The capture of free carriers by the oxide traps through tunneling allows to present the capture cross section of the traps as $\sigma = \sigma_0 exp(\theta x)$ where θ is a

tunneling parameter and x the tunneling distance. The spectral density of the input current is expressed as followed:

$$\frac{S_{IB}}{I_B^2} = \frac{kTN_T}{\theta A_S f} \qquad 1.17$$

where N_T presents the number of traps per unit area and energy interval ($cm^{-2}eV^{-1}$) and A_S is the emitter area.

1.3.1.1.6 Random walk model

In this model, 1/f noise is generated by a random displacement of carriers at the interface levels through interface states [37]. Experimental results in [31][37][39] were based on the random walk model which predicts that the slow states at the Si-SiO_2 interface are responsible for the 1/f noise. The 4 possible transitions of carriers via the interface states are presented in Figure 1.5. The transition a and b represent the trapping/de-trapping behavior of carriers via an interface trap located at Si/SiO_2 interface. Meanwhile, some carriers might be either captured by a nearby interface trap (transition c) or originated with nearby interface traps (transition d).

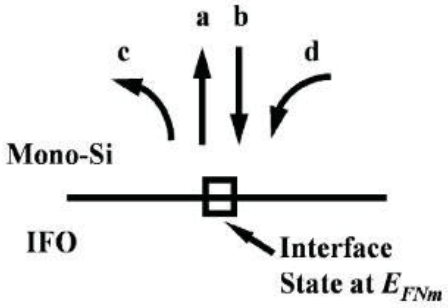

Figure 1.5. Schematic of the possible carriers transitions for IFO interface states [32].

The spectral density of the input current is given as:

$$S_{IB} = 0.1\frac{I_S^2}{fA_E N_{IT}} \qquad 1.18$$

where N_{IT} represents the interface state density and I_S is the surface current. Hence, the 1/f spectral density can be presented as:

$$\frac{S_{IB}}{(I_{S0}\frac{I_B^{2m/n}}{I_{B0}^{2m/n}})^2} = \frac{0.1}{fA_E N_{IT}} \qquad 1.19$$

1.3.1.2 I_B models

The second category of the physical models that were introduced are based on Hooge model earlier in [40][41][42][43]. These models respect an I_B dependency where the 1/f noise is related on the fluctuation of carrier's mobility. The spectral density of the 1/f noise examined in 1.20 was presented in 1988 by Van Der Ziel [44].

$$S_{IB} = K_{diff}\frac{I_B}{f} \quad 1.20$$

K_{diff} parameter corresponds to the various diffusion mechanisms that can occur in the bipolar transistors.

A more recent physical model was proposed by Valdaperez in 2002 for the poly-emitter bipolar transistors [45]. According to Valdaperez, the 1/f noise sources are related to the diffusion of the carriers in the base and the emitter area.

The concept presented by Hooge was not the only respected concept corresponding to an I_B dependency. Several analyses were held to highlight a geometrical dependency of the component contrarily to the Hooge model. An interpretation was maintained by Simoen in [46] and has related the 1/f noise to a perimetrical effect independently to the carrier's diffusion behavior. A similar dependency was examined by Pawlikiewicz in [47] and Kleinpenning in [48].

1.3.2 G-R physical models

In the LFN domain, based on the literature study, G-R components represent the noise sources the less investigated comparing to the 1/f noise sources. A G-R physical model was presented in [49] depicted as:

$$S_I = \frac{I^2}{n^2 V} 4n_t f_t (1 - f_t)\frac{\tau}{1 + \omega^2\tau^2} \quad 1.21$$

where V is the volume of the semiconductor, I is the mean value of the current bias, n is the density of charge carriers, f_t corresponds to the occupation probability of a trap level by the Boltzmann statistics and τ the time constant related to the trapping/de-trapping process. The time constant, τ, representing the capture and the emission of carriers in the trapping/de-trapping process is expressed by:

$$\tau = \frac{T_a^2}{\sigma_n \upsilon_{th}(T_a) N_c(T_a) T^2} exp(\frac{E_c - E_t}{kT}) \quad 1.22$$

where E_c-E_t corresponds to the activation level of the traps, σ_n is the effective section of electron capture at room temperature T_a and υ_{th} is the electron thermal speed.

Based on the physical model presented in 1.20, the noise properties of the G-R component can be summarized as followed:

- The noise spectral density S_I is proportional to the quadratic evolution of the current bias I^2.
- For constant current bias, the G-R amplitude is inversely proportional to the device's volume V.
- Its frequency response corresponds to a Lorentzian spectrum characterized by a stable plateau magnitude up to a certain frequency value, f_{ci}, where the spectral density becomes inversely proportional to f^2, a slope value of -2 is depicted. The cut-off-frequency, f_{ci}, corresponds to the frequency at which the amplitude of the plateau is divided by two.

- The cut-off frequency is related to the time constant τ by the relation:

$$f_{ci} = \frac{1}{2\pi\tau} \quad 1.23$$

1.4 Compact model of the excess noise sources

The noise SPICE model is a compact model used to evaluate the noise levels in circuit simulators. This model allows to investigate the excess noise effects that are highly needed by circuit designers to validate the component and/or the circuit performance. Moreover, the compact modeling of the excess noise components is used as an indicator to compare the variations of a technology during its development, and to compare one technology with another. In this thesis, both 1/f noise and G-R components were examined. Thus, the compact model of each excess noise component will be depicted and the extraction of their parameters will be described. Associated to physical models, the evolutions of these parameters versus bias and geometrical dimensions lead to some assumptions concerning the localization of the excess noise sources.

To investigate the excess noise for both input and output of the device, similar compact models can be applied. Circuit designers have recently presented an interest to the fluctuation of the output current. Nonetheless, the fluctuations of the input current presented the main studied topic in the literature. Hence, the SPICE models will be delivered based on the spectral density of the input current of the device.

1.4.1 1/f SPICE model

The main discussed noise in the literature is the 1/f noise. Therefore, the 1/f SPICE model was mostly introduced in the LFN analysis. In this work, the 1/f SPICE model was investigated at the input of the bipolar transistor through the base current spectral density S_{IB}. The 1/f model depicts the evolution of S_{IB} as a function of I_B and is presented as:

$$S_{IB} = K_F \frac{I_B^{A_F}}{f^{\gamma}} \quad 1.24$$

where K_F represents the 1/f noise level of S_{IB}, A_F its evolution as a function of the input current and γ represents the evolution of S_{IB} as a function of the frequency. These three parameters are known as the 1/f SPICE parameters.

The 1/f SPICE model of bipolar transistors in the LF domain presented in 1.24 is considered as a simplified model due to the complex structure of these devices comparing the MOS components [50][51]. The complexity of the bipolar devices is related to the two carriers' type diffusion of the two-junction associated to the multiple vertical and horizontal interfaces that can occur. Additional parameters can include the interpretation of geometrical effects of the device (perimeter and surface effects).

The extraction of the three SPICE parameters is done by the following steps.

- The γ parameter is extracted directly from the measured current spectral density S_I as a function of the frequency. This parameter corresponds to the slope value of the S_{IB}. An example of S_{IB} is given in Figure 1.6. The S_{IB} is measured in a frequency range of 10

Hz to 100 kHz. In this example, the 1/f noise is depicted in the frequency range of 10 to 100 Hz and a slope value of -1 is deduced. Thereby, the γ value is equal to 1. Spectra presenting a 1/f noise are characterized by a γ value that can vary in the range of 0.9 to 1.1 [24].

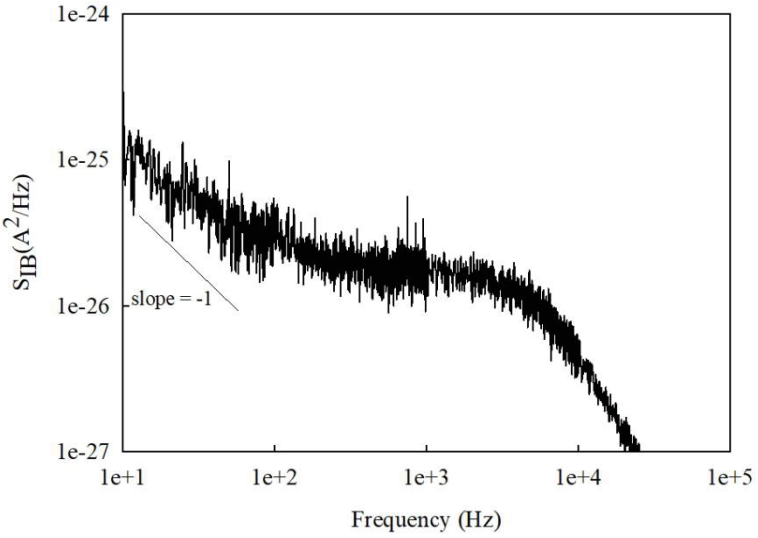

Figure 1.6. The extraction method of the γ parameter.

- A_F parameter is extracted by plotting the S_{IB} at 1 Hz as a function of the input current. To extract a precise A_F value, a minimum of three current biases should be considered that allows to extract a clear dependency. The A_F extraction will be presented in chapter 2 with the experimental results established in this thesis.
- Once the two 1/f SPICE parameters (γ, A_F) are well defined, K_F value can be deduced from the model presented in 1.21. The extraction of K_F is established for S_{IB} at 1 Hz and is given by:

$$K_F = \frac{S_{IB\ at\ 1Hz}}{I_B^{A_F}} \qquad 1.25$$

Based on earlier experimental results presented by several authors [52][53] the 1/f noise base current spectral density for Si bipolar transistors is found to be dependent on the I_B^2 and inversely proportional to A_E. These dependencies depict the main physical models that were examined in section 1.3.

1.4.2 G-R SPICE model

The spectrum analysis of a bipolar transistor presenting a Lorentzian shape can be related to a unique or to several trap centers. Therefore, the general representation of the G-R SPICE model is depicted as the sum of several Lorentzian components. The G-R SPICE model is given by:

$$S_{IB} = \sum_{i=1}^{N} \frac{A_i}{(1 + \frac{f_{ci}}{f})^2} \qquad 1.26$$

where A_i is the Lorentzian plateau magnitude of each detected G-R component and f_{ci} is its associated cut-off frequency.

The extraction method of the model parameters will be given in the next chapter. Each G-R component presents a unique signature: A_i, f_{ci}.

1.5 State of art of LFN for Si-Bipolar transistors

Since 1980, there has been a growing interest in the study of the LFN noise in bipolar transistors (theory, source origin, physical localization, modeling …). In the literature, studies were held on different Si based bipolar transistors: homo junction bipolar transistors, Poly-emitter homojunction bipolar transistors and heterojunction bipolar transistors. In this section, some of the published LFN analyses will be listed for each type of bipolar transistors.

1.5.1 Si BJTs

The LFN studies in Si homojunction bipolar transistor were mainly performed till the start of '90s. These studies were initiate by Van der Ziel group in 1984 in [54] for LFN measurements on bipolar NPN transistors. These studies have resulted by locating the 1/f and the G-R noise sources at the periphery of the emitter area. The 1/f noise sources were related to the fluctuation of the carrier's mobility [44][47]. Based on mobility fluctuation noise, T.G.M Kleinpenning [55] proposed, for the 1/f noise in bipolar transistors, expressions for current and experimental results were explained in terms of fluctuations in the mobility of free charge carriers.

In 1989 and 2001, LFN studies established the origin of the G-R components [56][57]. The detection and the modeling of the G-R components at room temperature have estimated 5 different G-R components. Each component has presented a distinct amplitude level and cut-off frequency that have varied in a frequency range of 0.5 Hz – 100 kHz. The detected traps were related to 5 distinct deep-level impurities in the p-n junction randomly distributed across the device area.

1.5.2 Si PE-BJTs

At the beginning of '90s, a new type of Si bipolar transistor was developed: the poly-emitter bipolar transistors (PE-BJT). These devices have presented higher frequency performances and improved noise properties. The poly-emitter transistor is a Si homojunction transistor that presents an interfacial oxide layer deposit at the interface of the emitter-base layer. This deposit layer is considered as a barrier to block the diffusion of holes from the base to the emitter region. During its development period (mid-90's mid-2000), intensive LFN studies were undertaken by several groups, mainly associated in the investigation of the 1/f noise, for instance in [46][18][58][59], a review can be found in [17]. These studies cover theoretical, experimental and compact modeling of the 1/f noise as well as the impact of different stresses (hot electron, irradiation, etc). When G-R components are present (mainly in small area devices) there were associated to RTS noise.

The 1/f noise was studied in 4 NPN poly-emitter transistors in 1994 in [60]. The 4 transistors have presented different oxide layer structures related to multiple fabrication processes. The input current dependency was examined for each structure. A quadratic evolution of the spectral density as a function of the base current I_B was the predominant behavior extracted in this study. The I_B^2 dependency corresponds to the diffusion of holes at the oxide interface layer by a tunneling effect.

A study of several chemical treatments (HF, RCA) was established on the mono-crystalline layer before the deposition of the poly-emitter layer. This study was held in 1995 by Mounib et al [61] by Simoen et al[17] and by Siabi-Shahrivar et al [62]. The HF treatment led to a non-uniform oxide thickness in the range of 0.4 nm, while the RCA treatment led a relatively uniform oxide thickness in the range of 1 to 1.14 nm. The evolution of the S_{IB} in response to I_B was found to be similar for both type, HF and RCA treatments. However, the 1/f noise level was greater by half of decade for devices with RCA treatments.

In 1996, a study was accomplished on the impact of the reduction of the emitter area on the low-frequency noise for a self-aligned poly-emitter bipolar transistor [63]. This study focused on the RTS noise in the tested bipolar transistors, especially on the evolution of the characteristic times of capture and emission of the RTS noise as a function of the emitter-base voltage V_{BE} and temperature T. It was established that RTS noise was due to tunnel transitions between low interface states located at Si/SiO_2 interface and silicon conduction band. During this period several paper related to the RTS study were published [64].

Several investigations were held by Jamal Deen et al. in the LFN domain on NPN and PNP poly-emitter bipolar transistors in [52][65][66][67]. According to their results, the spectral density S_{IB} of the NPN transistors was mainly described by the 1/f noise followed by the shot noise $2qI_B$. Contrarily to the PNP devices that mainly presented no less than one G-R components. The evolution of the 1/f spectral density is found to be dependent on the quadratic evolution of I_B and inversely proportional to A_E. The 1/f noise sources in both devices type are located in the oxide layer at the interface of the poly/mono-silicon interface. The negligible impact of the temperature on the 1/f noise was found for the NPN transistors. While an inverse dependency on the Temperature was examined by analyzing the G-R components in the PNP transistors.

1.5.3 Si/SiGe HBTs

As for Si/SiGe based heterojunction bipolar transistor, the first development of these components started earlier of the s'90. However, this technological evolution really taken off in the middle of the '90s due to the increase in the high-speed integrated circuit demands, particularly for telecommunications.

Due to its compatibility with the CMOS technology, Si/SiGe HBTs developed in BiCMOS technologies appeared as serious competitors of the III-V HBTs in term of pure frequency performances at first then in terms of fabrication cost, performance and compatibility with CMOS. LFN analysis started at the same time with approximately the same LFN groups listed in the previous paragraph concerning PE-Si BJTs. The main studied subject has involved the localization and identification of the physical origins of the 1/f noise sources. In 1994 and 1995, an analysis of the components was maintained of HBTs presenting an ideal spectral response (1/f noise followed by the shot noise) [68][69]. The analysis resulted in a linear evolution of the 1/f noise level as a function of I_B. The 1/f noise was related to the fluctuation of the carrier's number at the hetero-interface of the emitter-base area.

Si/SiGe HBTs based on a UHV/CVD deposition of the polysilicon emitter area were studied in 1996 by J.D. Cressler and others in [59][70], and till now the same group continued with

intensive studies on the impact of different type of irradiations [71][72]. The spectral density of the input current S_{IB} has resulted in a $1/A_E$ and an $I_B^{1.9}$ dependencies for the selected devices. The 1/f noise sources were estimated to be homogenously distributed at the interface of the emitter area. The impact of the Ge atoms incorporation in these devices were examined in 1997 by other research groups [73] to highlight their negligible impact which was concluded by Cressler's group. The influence of the incorporation of carbon atoms in the SiGe layer was also studied in [53] highlighting induced G-R components at high carbon level.

Further investigation was established in 1999 and 2000 by analyzing the current spectral density for both the input and the output of the transistors [74][75]. The analysis of the Si/SiGe HBTs at several bias conditions allows to highlight the suspected area where the dominant noise sources are located. As a result, a quadratic evolution of the S_{IB} as a function of I_B was extracted and the dominating noise sources were supposed to be distributed at the emitter-base region.

Other researcher groups examined the geometrical parameters impact on the LFN measurements. A distinct behavior was found depending on the emitter surface in [76][77][78]. Transistors presenting a large emitter surface presented the overcome of the 1/f noise. The 1/f noise respected an I_B^2 and a $1/A_E$ dependencies. The 1/f noise sources were related to the superposition of several recombination centers distributed at the emitter surface. Contrarily to this conclusion, another study resulted in a none-dependency to the emitter geometry in [79]. While G-R components were mainly recorded for smaller emitter geometries. As for PE-BJT, these G-R components were generally associated to RTS noise [80][81][82].

From the beginning of 2010, a decrease of publications concerning Si/SiGe HBTs occurred. This was due to the gradual disappearance of some component manufacturers. As a consequence, only a few research groups are still working in the field of LFN on Si/SiGe HBTs [83][84][85][86][87].

1.6 Conclusion

In this chapter, the basic information in the Low-frequency noise domain needed to accomplish this thesis was given. The different noise components that can be found in semiconductor devices were listed in the first section. These noise components were classified as either white noise or excess noise.

The excess noises, 1/f noise and G-R components, will be the two investigated noises in this work mainly the 1/f noise. Based on the literature, some of the physical models were presented, mainly the 1/f physical models based on the I_B^2 evolution. These physical models are consistent with the main extracted behaviors of the heterojunction bipolar transistors which will be studied in the work.

The LFN domain presented a high interest for circuit designers. Thereby, simplified compact models were developed to examine both 1/f noise and G-R components. The extraction techniques of the SPICE parameters from the experimental results were presented.

The last section of this chapter covered the state of art of several types of bipolar transistors. The concluded results concerning low frequency noise were examined for homo junction mono-

emitter and poly-emitter bipolar transistor and the heterojunction bipolar transistors. The examined investigation for the newest bipolar components resulted in a $1/A_E$ and an I_B^2 dependencies of the 1/f noise. Even though the low-frequency domain presents several years of research and establishments, the localization of the noise sources and their origins remain a complex field of study.

Chapter 2 Test bench and Low-Frequency Noise measurements of Si/SiGe:C HBTs

2.1 Introduction

Low-Frequency Noise (LFN) measurements are highly recommended by circuit designers during the design of particular integrated circuits (due to the up-conversion phenomenon) and by engineers while developing the technological process of a device (quality and reliability indicators for instance). To accomplish these measurements, a high-quality test bench is required with an adapted well-defined environment that allows retrieving reliable data.

The first section of this chapter is devoted to the description of the test bench used to measure the input current fluctuations of the transistor, base current spectral density S_{IB}. The equivalent circuit of the modulated noise by the device and the measurement chain will be respectively presented. Based on theoretical expressions, the current fluctuation of the transistor will be expressed. The studied devices are Si/SiGe:C HBTs developed by STMicroelectronics issued from BiCMOS technology. In this thesis, two BiCMOS technologies will be investigated with a distinct CMOS node of 130 nm and 55 nm, BiCMOS9MW and B55 respectively. As already exposed, the main objective of this thesis is the characterization of the B55 technology while the mature BiCMOS9MW is mainly studied for comparison. The manufacturing process and the key parameters that led to a distinct behavior will be presented. Moreover, the geometrical configuration of the selected devices in this study will be listed for each technology.

Before establishing the LFN measurements, DC characterization is elementary to initiate the study. They are necessary to evaluate the device's performance and to define the bias range responsible for the ideal performance of the transistor. Therefore, DC analysis will be established in section 2.5. Several current components can occur from these devices depending on the bias range which will be presented in detail. To conclude this section, a comparison of the distinct DC performances will be given for HBTs of each technology.

The LFN spectroscopy of a tested devices figures in two types of spectra that can be affected by the presence of Generation-Recombination noise component. This subject will be described in section 2.6. LFN measurement is considered as a highly sensitive characterization technique. Thereby, several phenomena can impact the obtained results. Section 2.7 will introduce the dispersion effect that may lead to non-reproducible results, from a die to another, for identical devices.

In section 2.8, after a global spectral analysis, experimental measurements and analysis of 1/f noise and G-R components will be presented in paragraph 2.8.2 and 2.8.3 respectively. As for the DC study, this study will be divided into two parts: analysis as a function of several collector structures from the same B55 technology and analysis as a function of two variations of the B55 technology. The noise components will be interpreted by compact models whose parameters will be extracted. Associated to the geometrical parameters study, it will be used to highlight the defected area in which the noise sources occur. For the 1/f noise, two Figures-Of-Merit, K_B and f_c/f_t, will be used to interpret the evolution of the fabrication process of the HBTs between the technologies.

2.2 Low-Frequency Noise bench test

LFN measurement is a highly sensitive characterization method that requires high-quality bench test instrumentations. The measured noise must correspond to the noise produced by the tested component without the interference of any external perturbation. Therefore, LFN spectroscopy needs low noise instrumentations as well as some grounding and shielding techniques skills. The measurement system is placed in a Faraday cage to reduce any mechanical and electromagnetic perturbations. Batteries are used as a power supply to minimize the electrical perturbations that can be induced by the electric power supplies. Some additional perturbations can be generated from the instruments and the cables affecting the proper noise of the device that needs to be considered.

Two LFN configuration setups exist known as: high impedance and low impedance configuration. This work will mainly present an interest in the fluctuation of the base current. Therefore, only the high impedance configuration will be discussed. Equivalent noise circuit and theoretical expressions will also be presented.

The high impedance test bench aims to directly measure the input current fluctuations of the device. The measurement chain, presented in Figure 2.1, constitutes a low noise current amplifier (EG&G 5182), a bias circuit, a low-noise current preamplifier to bias the collector (SR 570) and a signal analyzer (HP 84410A). The analyzer assesses the spectral density of the base current S_{IB} by a Fourier transform. Data are registered through an IEEE bus on the computer. The DUT contacts of this configuration are established on wafer through the HF configuration of the devices by using coplanar probes. Measurements are usually established in a frequency range of 1 Hz to 100 kHz. However, most of the examined measurements in this thesis are established in the range of 10 Hz to 100 kHz.

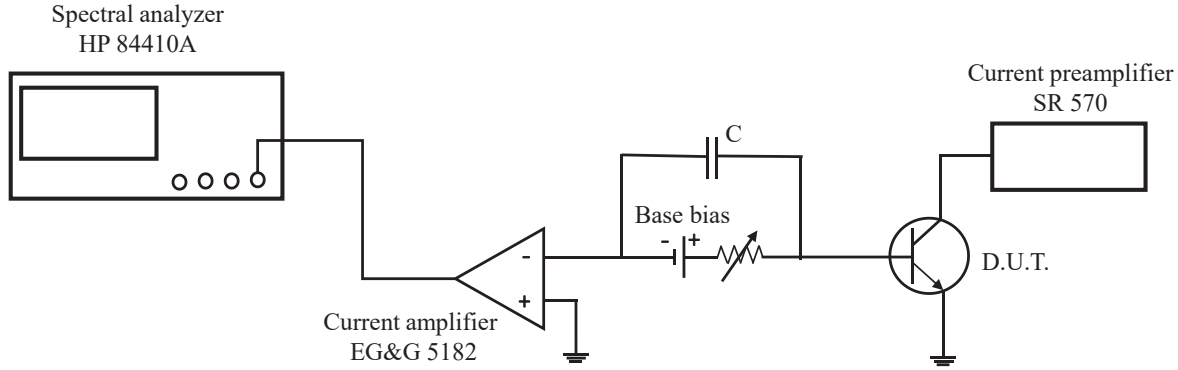

Figure 2.1. High Impedance configuration bench test for S_{IB} measurement.

The equivalent small signal circuit of the measurement chain noise associated to the intrinsic transistor noise sources is presented in Figure 2.2.

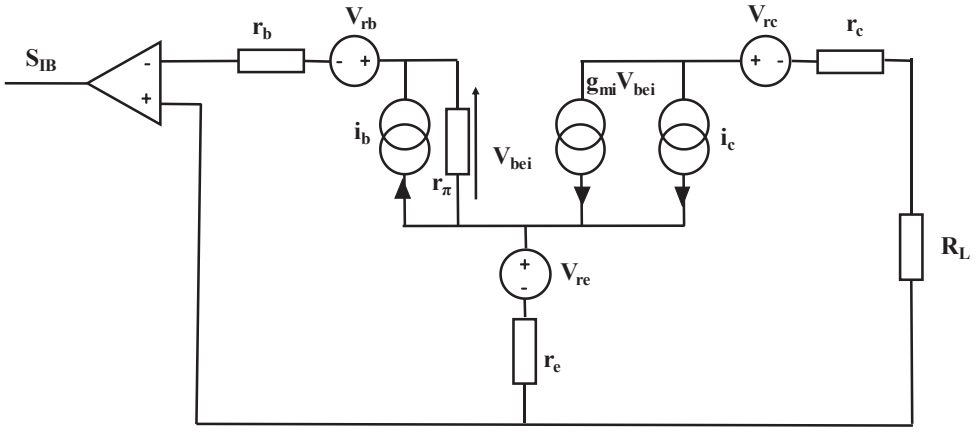

Figure 2.2. LFN equivalent circuit of the I_B fluctuations generated by the measurement bench and DUT.

- r_b, r_e, r_c represent the access resistance of the transistor which depends on the doping level of each area. These resistances are associated to a noise source illustrated as V_{rb}, V_{re}, V_{rc}.
- g_{mi} is the transconductance of the intrinsic transistor defined as $g_{mi} = \frac{h_{fe}}{r_{\Pi}}$; h_{fe} represents the dynamic current gain and r_π represents the dynamic resistance for the intrinsic input of the transistor.
- i_b, i_c are the equivalent noise sources associated with the base and the collector currents.

The theoretical expression of the input current spectral density, S_{IB}, proposed by Kleinpenning in [88] provoked a fully correlated behavior between the input and the output noise sources of the intrinsic transistor ($\Gamma_{ibic} = 1$). In addition to the negligible influence of r_c, S_{IB} Kleinpenning's model is presented in eq. 2.1.

$$S_{IB} = \frac{(r_{\Pi} + g_{mi} r_e)^2}{Z_0^2} S_{ib} + \frac{r_e^2}{Z_0^2} S_{ic} + \frac{1}{Z_0^2} S_{Vr} \qquad 2.1$$

where

$$Z_0 = r_{\Pi} + r_b + (g_{mi} + 1)\, r_e \qquad 2.2$$

$$S_{Vr} = S_{Vrb} + S_{Vre} \qquad 2.3$$

r_π presents a high value that dominates the Z_0 expression. Thereby, the impacts of the second and third terms of the model depending on S_{ic} and S_{Vr} respectively are negligible. Hence, the measured fluctuations of the base current correspond to the intrinsic base current fluctuations of the transistor presented as followed:

$$S_{IB} \approx S_{ib} \qquad 2.4$$

This approach was verified by previous studies in the group [89][90] where only S_{ib} has dominated S_{IB} for poly-Si and Si/SiGe transistors.

2.3 Studied technologies

The studied devices are Si/SiGe:C HBTs integrated in a BiCMOS technology. These components are developed by STMicroelectronics for RF, MMW and THz applications in the frame of the European TARANTO project. STMicroelectronics aims to satisfy the demand for new applications by providing higher performances for the integrated circuits (IC). In this thesis, two BiCMOS technologies were studied that correspond to a mature BiCMOS9MW technology (wafer titled J109FRM-19F5) presenting a 130 nm CMOS node and a technology under development presenting a 55 nm CMOS node known as the B55 technology (wafers titled Q737119 w-24, PORBORNOO-C5B and Q630012Q13). The BiCMOS9MW technology was detailed during the thesis of Marcelino Seif [84]. It is considered as a mature technology and will be used as a reference in this work. Both BiCMOS generations are based on a Double-Polysilicon Fully-Self-Aligned architecture associated with a selective epitaxy growth for the SiGe:C base. A Scanning Electron Microscopy (SEM) cross-section of the HBTs is illustrated in Figure 2.3.

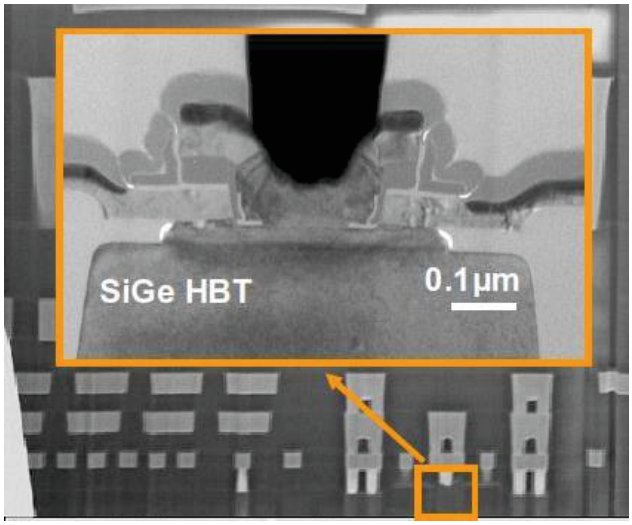

Figure 2.3. SEM cross-section of the HBT technologies [91].

The general process of HBTs fabrication initiates with the construction of the collector area with a buried layer implementation, the collector epitaxy then the conception of the isolation trench (STI, DTI) followed by the implementation of the Selective Implanted Collector. Once the conception of the collector area is done, the fabrication process of the Emitter-Base area begins. The conception of the Si/SiGe E-B heterojunction is accomplished by the deposition of listed layers respectively: pedestal oxide, extrinsic poly-base, nitride oxide, intrinsic base SiGe:C, spacer oxide, Si poly-emitter. The fabrication module ends with the activation of the dopant, the silicidation layer deposition and the contact formation. The fabrication processes of the HBTs issued from the B55 technology can be found in detail in [92] where some of the technological modifications were listed like: shrinking the geometrical parameters and tilt the substrate of 45° for instance. One important consequence, for the analysis and the interpretation of some results found during this work, is the shrinking of the new BiCMOS technology, leading to a decrease in the E-B oxide layer thicknesses of 40 %, especially the spacer one.

Moving towards the recent technology, an increase in the frequency performances of the transistors was highlighted that conditions the performances of the associated circuits. The device's behavior at high frequency is characterized by the transition frequency f_t and the maximum oscillation frequency f_{max}:

- Transition frequency, f_t, is the frequency at which the current gain is equal to 1. It is inversely proportional to the carrier's transition time from the emitter to the collector contact, τ_{EC}. f_t is expressed by the following equation:

$$f_t = \frac{1}{2\Pi\tau_{EC}} \qquad 2.5$$

  Associated ICs usually operate at a fraction of its real value limited by parasitic parameters. Therefore, f_t values can only be extracted through an interpolation. This parameter is considered as a figure of merit to compare different generations of similar technology. f_t values witnessed an increase in the B55 technologies comparing to the BiCMOS9MW, 320 GHz and 230 GHz respectively.
- Maximum oscillation frequency, f_{max}, corresponds to the frequency when unilateral power gain (Mason's gain) becomes unity which defines the boundary between active and passive networks. The extraction of f_{max} values is a critical process comparing to the f_t, since its values depends only on the intrinsic parameters of the device. f_{max} is expressed as;

$$f_{max} = \sqrt{\frac{f_t}{8\Pi r_b C_{bc}}} \qquad 2.6$$

  f_{max} is found to be inversely proportional to square root of the intrinsic base resistance r_b and the transition capacitance of the BC junction C_{bc}.

In addition to the modification introduced in the B55 technology, several technological architectures or process steps were examined to improve or modulate the HBTs performance. These modifications occurred on both the collector area and the E-B junction of the components. In this thesis, three collector structures (i.e. three collectors doping levels) and E-B carrier's activation methods applied to the B55 technology will be studied.

2.3.1 Collector structures: HS, MV, HV

Several collector doping levels of HBTs were designed while developing the B55 technology. The High Speed (HS) HBTs present the highest collector doping level localized in the Selective Implanted Collector (SIC), presented in Figure 2.4, which is absent from the Medium Voltage (MV) HBTs. HS transistors are designed with an important doping level to reduce the base-collector capacitance, hence, to increase the frequency performances f_t and f_{max}. However, the reduction of the collector doping level in MV and HV transistors led to increase the collector-emitter breakdown voltage in the common emitter mode, BV_{CE0} by 27 % and 113% respectively comparing to HS.

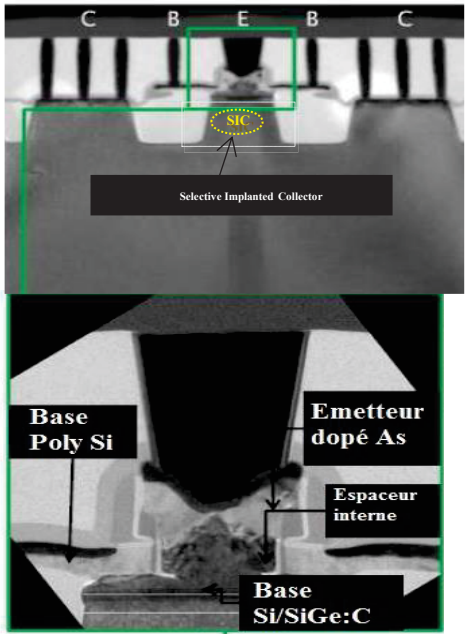

Figure 2.4. TEM cross-section of HBT of the BiCMOS technology

Transition frequency (f_t), maximum oscillation frequency (f_{max}) and collector performances presented a direct dependency on the collector doping concentration [93]. The properties of each structure are listed in Table 2.1.

	HS	**MV**	**HV**
f_t (GHz)	326	178	64
f_{max} (GHz)	376	384	269
J_C (mA/µm2)	19	6.1	1.9
BV_{ce0}	1.5	1.9	3.2

Table 2.1. HBTs properties depending on the collector structure

The high doping level of the collector structure reduces the base-collector capacitance C_{bc} which presents a direct impact on f_t and f_{max}. Hence, HS devices highlighted an important frequency performance of 325 GHz comparing to the MV and HV devices with 180 GHz and 65 GHz respectively. Nevertheless, as expected, the decrease of the collector doping level has resulted in an increase of the breakdown voltage in the common-emitter mode BV_{ce0} from 1.5 V for HS devices to 3.2 V for HV devices.

2.3.2 Dopant activation methods

A modification of the Spike Annealing (SA) properties was carried out by STMicroelectronics as a possible optimizing step of the B55 process [9]. A decrease in the dopant activation temperature of the SA was established by a total of 63 °C, from 1113 °C for BiCMOS9MW to 1050 °C for B55.

Nonetheless, while developing the B55 several activation techniques were investigated. Two generations of this technology occurred with a distinct activation method. The first one is the SA which represents a classical thermal activation technic and will be referred to B55 TH. While the second one, it contributes to a Dynamic Spike Annealing that will be referred to B55 DSA.

A detailed study was previously examined in [9] to present a better control of dopant diffusion and activation methods. Nevertheless, only one DSA procedure will be presented in this part which corresponds to the provided wafer by the industrial partner. The new activation technique presents a decrease in the spike annealing process of 30 °C, the SA is established at 1020 °C followed by a dynamic spike annealing process. The reduction of the thermal budget decreases the MOSFET performance, therefore, its combination with the DSA process allows to partly recover the MOSFET characteristics.

Secondary Ion Mass Spectroscopy was accomplished for each activation method to study the diffusion coefficient of both Boron and Arsenic [94]. A negligible impact was found on the Boron atoms while a reduction of Arsenic atom's diffusion from the emitter to the base was detected for lower activation temperature. This effect impacts both C_{be} and r_e values. Thus, an increase in the frequency response (f_t, f_{max}) of the transistors was examined. A comparison of f_t performance for both B55 generations was provided by STMicroelectronics in Figure 2.5.

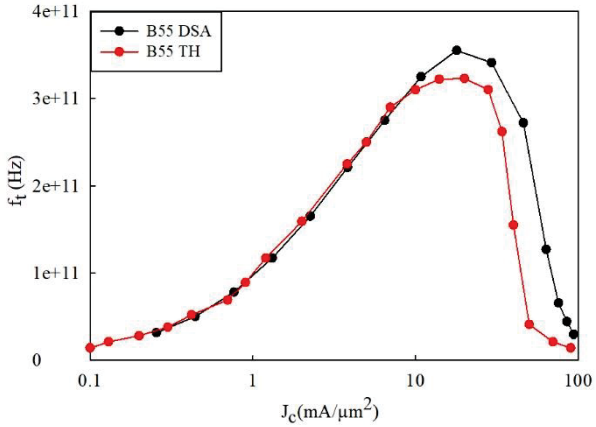

Figure 2.5. f_t comparison of both activation methods for the B55 technology.

2.4 HBTs configuration

Several configurations and emitter architectures were designed during the conception of the HBTs. A detailed study of the designed configurations and architectures that occur in these devices can be found in [92]. Only the characterized configurations will be presented in this section.

Figure 2.6 represents an example of two configurations that can be found in the selected devices. A single finger configuration HBT, illustrated in Figure 2.6.a, is expressed by the CBEBC sequence. A multi-finger configuration can also occurs depending on the number of Emitters contacts. The selected configuration in Figure 2.6.b presents a double finger configuration expressed by the CBEBCBEBC sequence.

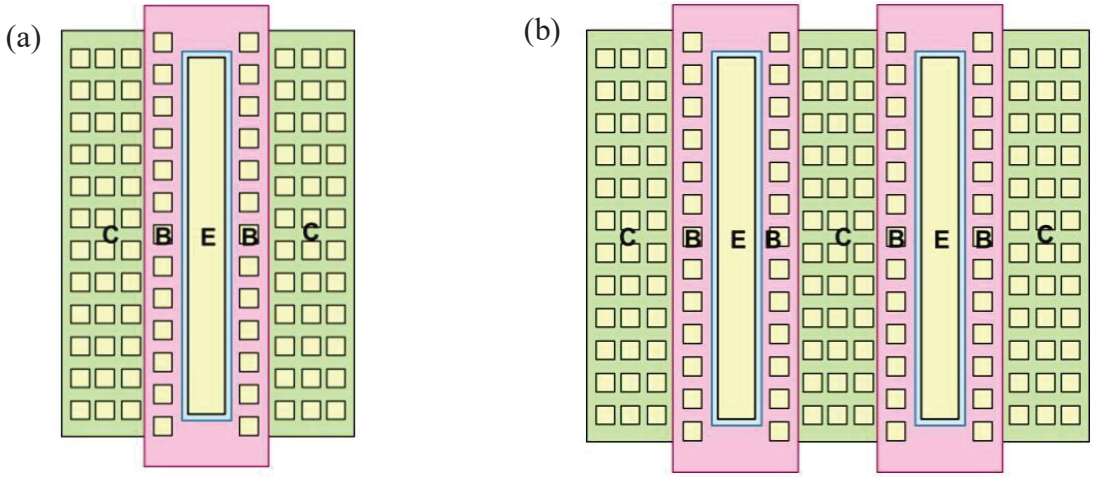

Figure 2.6.HBTs presenting a) a single finger and b) a multi-finger configuration [92].

In this chapter, two main studies were undertaken with a distinct pack of selected devices architecture. The first study that was held examine the three collector structures from the B55 TH technology: HS, HV and MV devices. The selected emitter geometries of HBTs are listed in Table 2.2.

Technology	HBT's name	Configuration	W_E (µm)	L_E (µm)	A_E (µm^2)
B55 (HS, HV, MV)	QHFB501	1 finger	0.2	0.45	0.09
	QHFB505	1 finger	0.2	5	1
	QHFB506	1 finger	0.2	10	2
	QHFB514	1 finger	0.42	10	4.2

Table 2.2. Geometrical characteristics of the HS, HV and MV studied HBTs from the B55 technology.

As for the second study, two dopant activation techniques of the B55 technology were investigated and will be presented as: TH and DSA. These results will be compared to the mature BiCMOS9MW technology. To compare both B55 and BiCMOS9MW HBTs, the devices were selected with similar emitter geometries, W_E, L_E and A_E. The considered devices of both technologies in this study are the High Speed (HS) structure. A detailed presentation of the investigated components is presented in Table 2.3.

Technology	HBT's name	Sample ID	Configuration	W_E (µm)	L_E (µm)	A_E (µm^2)
BiCMOS9MW	NBHSAH	1	1 finger	0.27	3	0.81
	NBHSAI	1	1 finger	0.27	10	2.7
		3	1 finger	0.27	15	4.05
	NBHSAO	1	1 finger	1.08	10	10.8
	NBHSAU	1	4 fingers	0.27	10	10.8

B55 (TH, DSA)	QHFB503	HS	1 finger	0.2	1	0.2
	QHFB504	HS	1 finger	0.2	3	0.6
	QHFB505	HS	1 finger	0.2	5	1
	QHFB506	HS	1 finger	0.2	10	2
	QHFB511	HS	1 finger	0.25	10	2.5
	QHFB512	HS	1 finger	0.3	10	3
	QHFB514	HS	1 finger	0.42	10	4.2
	QHFB521	HS	5 fingers	0.2	10	10

Table 2.3. Geometrical characteristics of the studied HBTs from the BiCMOS9MW and the B55 technologies.

2.5 DC characterization

DC characterizations are fundamental measurements that need to be done at first to depict the performance of the device. Once the HBT presented a normal behavior, current biases are chosen to perform the LFN measurements.

The selected DC characterization within this study is the Forward Gummel plot characterization illustrated in Figure 2.7. Gummel plot represents the evolution of the base and collector currents, I_B and I_C, in response to the emitter-base voltage bias V_{BE} while V_{BC} is maintained to zero. DC measurements are established on wafer by using the same coplanar probes needed for the LFN measurement. The measurement setup constitutes a Keithley 4200 semiconductor characterization.

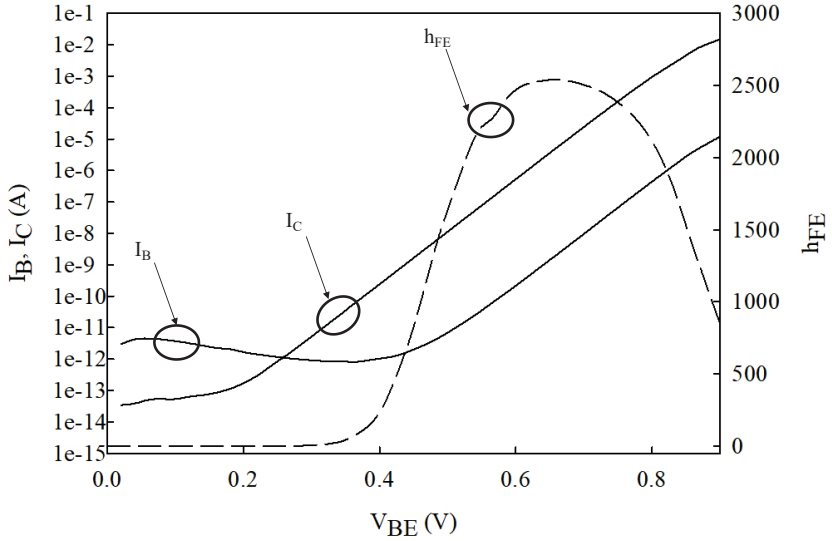

Figure 2.7. Forward Gummel mode of an HBT device. Solid lines: I_B and I_C, Dash lines: h_{FE}.

I_B and I_C of a transistor biased in a common-emitter configuration are expressed respectively in eq. 2.7 and 2.8. The static current gain h_{FE} is then obtained by eq. 2.9.

$$I_B = I_{SB}\, exp(\frac{qV_{BE}}{\eta_B kT}) \qquad 2.7$$

$$I_B = I_{SC}\, exp(\frac{qV_{BE}}{\eta_C kT}) \quad 2.8$$

$$h_{FE} = \frac{I_C}{I_B} \quad 2.9$$

where η_B and η_C represent the ideality factor of the base and the collector respectively and I_{SB} and I_{SC} represent their saturation current.

2.5.1. Base current components

As can be seen in Figure 2.7, several current components can dominate the base current that corresponds to a certain ideality factor. Four current components can be identified in three distinct V_{BE} range values. In the first V_{BE} bias range, $V_{BE} < 0.45$ V, generation-recombination current or tunnel current predominates the base current presenting an ideality factor that varies between a value of 1 to 2 or higher than 2 respectively. Then, a diffusion current component predominates the base current for voltage bias in the value range of 0.45 V and 0.8 V. In this bias range, HBTs present an ideal behavior operating with a current gain amplification, the ideality factor is equal to 1. Finally, in a V_{BE} range higher than 0.8 V, the high injection effects dominate the base current presenting an ideality factor in the range of 1-2.

2.5.1.1 Generation-recombination current

This current component occurs from generation-recombination traps or centers induced from crystal lattice dislocations, impurity atoms located in the crystal lattice, or at the surface defects. The energy of a recombination center is characterized by its capture cross-section inversely proportional to the carrier's lifetime and its activation energy.

Once the thermal-equilibrium condition of a semi-conductor is disturbed, $pn \neq n_i^2$, processes exist that allow to recover its equilibrium. Two types of processes can occur for the SiGe semi-conductors, a band-to-band transition or a band-to-trap transition [95]. Band-to-band transitions are more likely for direct-bandgap semiconductors (III-V materials). When $pn > n_i^2$ the recombination process takes place while the generation process reveals when $pn < n_i^2$.

Figure 2.8 illustrates the band-to-band recombination process.

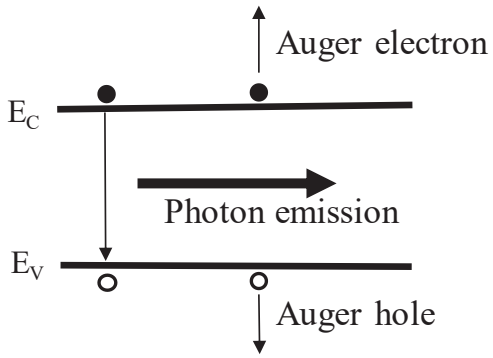

Figure 2.8. Band-to-Band recombination process

The transition of an electron from the conduction band to the valence band is conserved either by the emission of a photon (radiative process) or by the transfer of its energy to another carrier which will be ejected from the atom (Auger process).

Four basic processes are engaged in the generation-recombination carrier through trap levels that describe the band-to-trap transition. An occupied trap by a hole can cause its emission to the valence band or its recombination with an electron from the conduction band. When the trap is initially occupied by an electron, this electron can be emitted to the conduction band or a hole emission can occur from the valence band to recombine with the trapped electron [96]. These processes are illustrated in Figure 2.9.

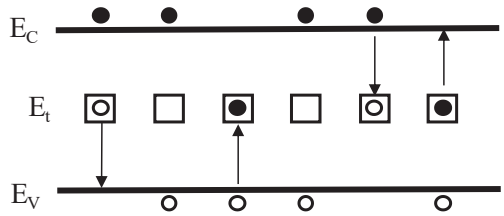

Figure 2.9. Generation- recombination processes through a single trap level

2.5.1.2 Tunnel current

In the classical mechanic behavior, only carriers with excess energy higher than the potential barrier can cross the potential walls. However, the tunneling effect is a quantum-mechanical phenomenon which allows representing the electron by its wave function. Therefore, electron tunneling probability through the barrier is not negligible [95]. Figure 2.10 illustrates the response of the wave function across the barrier, a significant decrease in the electron energy is marked by crossing from region A to region B without being completely restrained by the barrier's height.

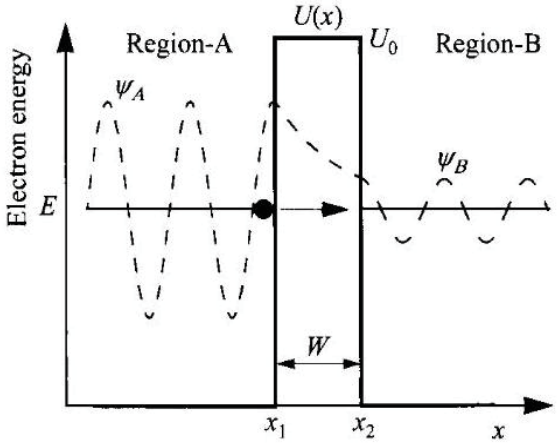

Figure 2.10.Electron energy tunneling through a potential barrier [95].

2.5.1.3 Diffusion current

When the excess carriers are not uniformly distributed in the crystal, the diffusion process occurs. The gradient of the carrier's concentration provokes their migration from the high

concentration region towards the lower concentration one. This phenomenon tends to lead the system into a uniformity state.

The carriers flow conforms with the Fick's law that is proportional to their respective concentration gradient. The diffusion current density of electrons and holes are respectively presented in eq. 2.10 and 2.11.

$$J_n = qD_n \frac{d\Delta n}{dx} \qquad 2.10$$

$$J_p = -qD_p \frac{d\Delta n}{dx} \qquad 2.11$$

The diffusion current component constitutes the ideal current behavior for the bipolar transistors.

2.5.1.4 High injection effects

The high injection effects result in a deviation from the Shockley's Law. The most common effect provoking this phenomenon is the impact of access resistors r_b and r_e at high current resulting in a decrease of the applied voltage [88]. Thereby, the voltage bias found at the extrinsic Emitter-Base junction can be presented as followed:

$$V_{BE'} = V_{BE} - r_b I_b - r_e I_e \qquad 2.12$$

Nevertheless, the deviation from Shockley's Law can be caused by other effects as the Webster effect, the Kirk effect and the current crowding effect.

The Webster effect is defined by the increase of holes in the base region due to the immigration of electrons from the Emitter to preserve the neutrality. The Kirk effect takes place once the charge density associated with the current through the Base-Collector junction is larger than the ionized impurity density in the Collector region. Increasing the Collector doping might seem like a solution for the Kirk effect. Nonetheless, it increases the Collector-Base capacitance C_{bc} and decreases the Collector-Base breakdown voltage BV_{cb}. Hence, the Kirk effect limits both RF and power applications. As for the third effect that can occur, the current crowding effect is induced by the restrained flow of the current lines near the Emitter window and limit the effective E-B width W_{Eeff} comparing to the real W_E. The intrinsic Base resistance is highly affected by the distribution of the current density through the Base region which causes a decrease in the current gain.

2.5.2 DC results and analysis of the B55 comparing to the BiCMOS9MW

In this section, DC analysis will be initiated by comparing the three collector structures of the B55 TH: HS, MV and HV. Later on, DC performances of the two B55 flavors, TH and DSA, will be examined. The B55 characteristics will be compared to the BiCMOS9MW ones.

2.5.2.1 Comparison of the three collector structures

As previously presented, the B55 technology is designed with three distinct collector structures. Each structure elaborates a specific collector dopant level in the SIC area.

Figure 2.11 illustrates the performance of selected HS, HV and MV devices presenting an identical emitter geometry from the B55 TH. The selected devices correspond to QHFB514 presenting an Emitter area of 4.2 µm^2.

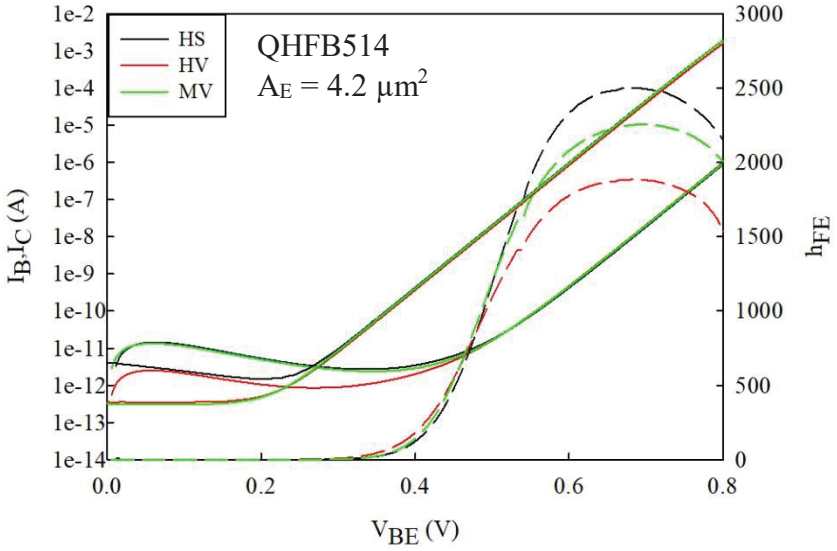

Figure 2.11. Gummel characteristics for HS, HV, MV HBTs of the B55 TH. Solid lines: I_B and I_C currents – Dash lines: DC current gain h_{FE}.

The impact of the collector doping level is highlighted in the low injection regime by the I_B level, for $V_{BE} < 0.5$ V. Independently to the collector structure, a tunneling current component occurred the Base current in the low bias area. This current component was repeatedly observed for the studied B55 HBTs independently from their geometrical parameters. High and medium collector doping level HBTs, respectively HS and MV, presented a higher level of tunneling base component compared to the lower collector doping one (HV device). This behavior is justified by the increase of the tunneling effect where a higher carrier number cross through the barrier's wall in high doped area as it is in HS and MV HBTs.

While in the diffusion area, 0.5 V < V_{BE} < 0.8 V, a negligible impact occurred on the I_B contrarily to the h_{FE}. A direct impact of the collector doping level was found on the maximum h_{FE} of each device. A decrease of the maximum h_{FE} was identified from a value of 2500 to 1870 for the high collector doping devices (HS) and the low collector doping ones (HV) respectively. While MV devices presented an intermediate behavior with a maximum h_{FE} of 2200. The decrease of the maximum current gain can be associated to the well-known Kirk effect [97].

A similar behavior was found independently from the emitter geometries of the tested B55 TH technologies.

2.5.2.2 Performances of the B55 TH and DSA, comparison with BiCMOS9MW

Since HBTs are needed for RF and THz application, HS HBTs present the best candidates for these industrial needs comparing to HV and MV devices. Therefore, HS transistors will be mainly referred to while comparing the performances of the different developed BiCMOS technologies.

Figure 2.12 represents the DC comparison of the two variations of the B55 E-B dopant activation techniques (TH and DSA) and the BiCMOS9MW technologies. A similar A_E of 4.05 μm^2 and 4.2 μm^2 was chosen for the BiCMOS9MW and the two B55 respectively.

Figure 2.12.a illustrates the distinct behavior of each technology in the low injection regime where I_B will be mainly discussed. The dominating current component in this regime is the generation-recombination current component for the BiCMOS9MW contrarily to both B55 where the tunneling current component dominates. A shift in the diffusion area by nearly one order of magnitude was witnessed moving from the BiCMOS9MW towards to the B55 technologies. For the selected HBTs, the diffusion area was initiated at a V_{BE} value of 0.42 V and 0.5 V for BiCMOS9MW and both B55 respectively.

The distinct performance of each technology in the diffusion area is mostly visible on the I_C level of the three types of transistors in Figure 2.12.a and by the maximum h_{FE} in Figure 2.12.b. A maximum h_{FE} of 1240, 2100 and 2560 was extracted for BiCMOS9MW, B55 TH and B55 DSA respectively. By controlling the dopant activation technic, an increase of the maximum current gain was systematically marked with a value of 460 for the selected B55 components. The described behavior was repeatedly observed independently to the emitter geometries with a minimum increase of 300.

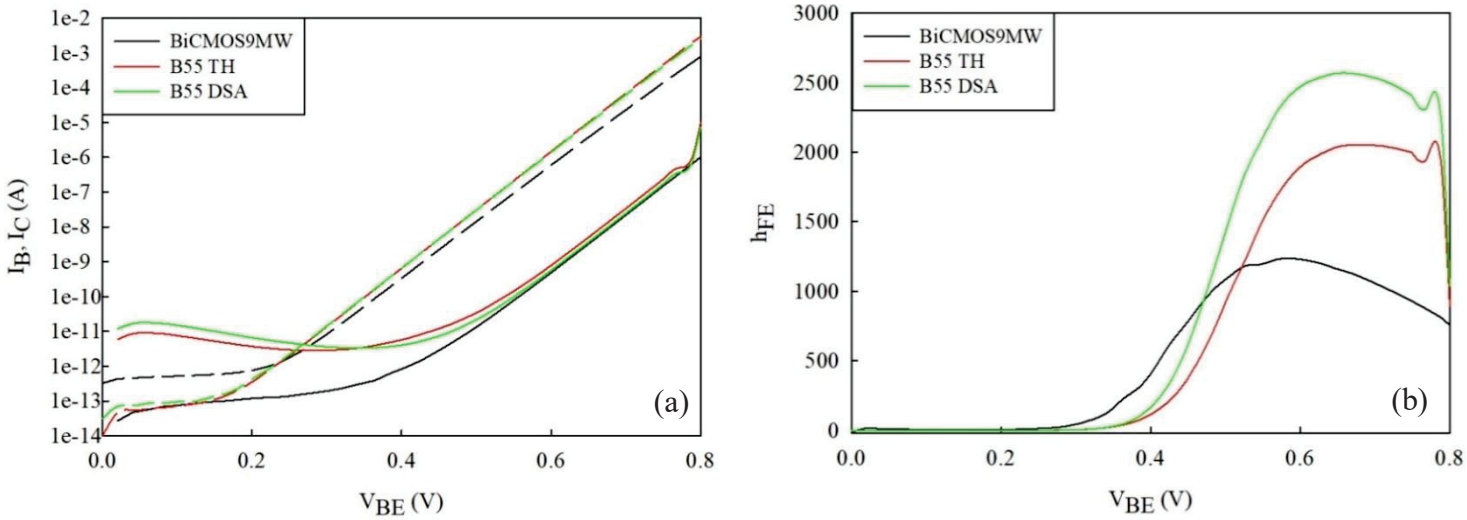

Figure 2.12. Gummel characteristics for a BiCMOS9MW HBT (A_E = 4.05 µm²) and the two B55 HBTs (A_E = 4.2 µm²). a) Solid lines: I_B current – Dash lines: I_C current b) current gain h_{FE}.

2.6 Low-Frequency Noise: Spectral analysis

Even though LFN measurement is time-consuming to perform, it's a highly effective method to detect defects in the materials. For instance, a distinct LFN behavior can be found for devices presenting identical I-V characteristics [89]. In this section, the decomposition of the current spectral density will be presented to identify the different LFN components. In the next sections, the aim will be to analyze and model the excess noise components as well as to locate the dominant noise sources in the selected devices representing the different flavors of BiCMOS technologies given in Table 2.2 and Table 2.3.

Spectral analysis established in the frequency range of 10 Hz to 100 kHz presents three possible noise components. An example is given in Figure 2.13 which represents the spectral density of the input current S_{IB}. The shot noise (red dash lines) is found to be dominated by either flicker noise (green dash lines) or G-R components (black dash lines) until a frequency greater than 1 kHz. The flicker noise, known as the 1/f noise, is illustrated as a linear decrease of the current spectral density inversely proportional to the frequency (a slope equals to -1). The 1/f noise level at 10 Hz is equal to 1.8 10^{-23} A^2/Hz for the selected HBT. Thereby, the 1/f noise level at 1 Hz is deduced simply by increasing the extracted value at 10 Hz by one decade, leading to a value of 1.8 10^{-22} A^2/Hz. As for the G-R component illustrated by a Lorentzian shape, it is identified by a proper cut-off frequency and plateau magnitude (presented in chapter 1 section 1.3.2). A transistor affected by the G-R noise presents no less than one Lorentzian component. Each component is characterized by distinct f_{ci} and A_i. The extraction of these parameters can be intricate in some cases. Therefore, a software is used to perform a more precise parameter extraction that will be detailed in section 2.8.3.1**Erreur ! Source du renvoi introuvable.**.

G-R components are mainly related to RTS noise that is observed as a square signal in the time domain analysis. RTS noise signal is presented in the inset of Figure 2.13.

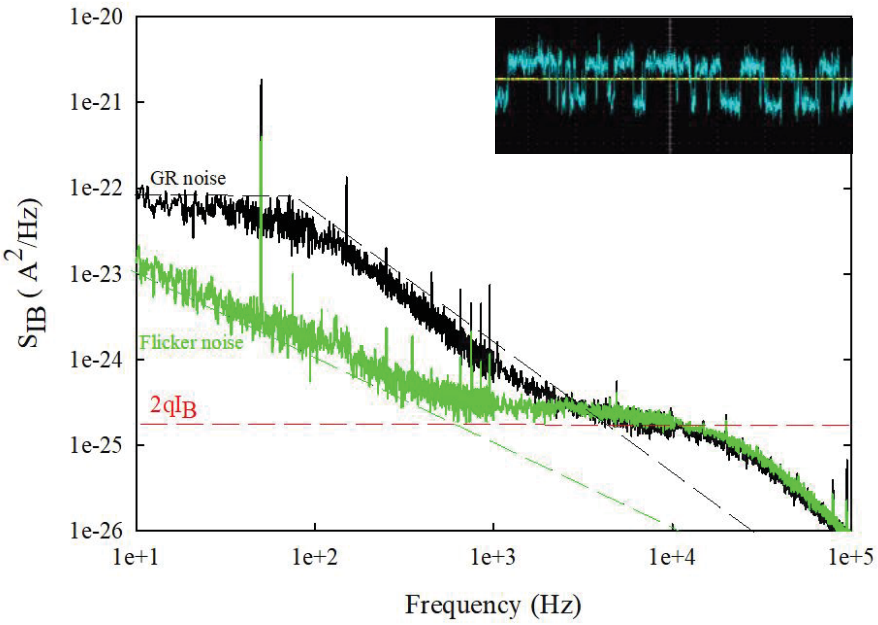

Figure 2.13. Current spectral density S_{IB} as a function of the frequency. Inset: RTS noise in time domain

Each current spectrum can be analytically encrypted by the following equation in eq. 2.13. The first and second terms represent the 1/f noise and the G-R noise components respectively, while the third one represents the shot noise.

$$S_{IB} = \frac{B}{f} + \sum_i \frac{A_i}{1 + (\frac{f}{f_{ci}})^2} + 2qI_B \qquad 2.13$$

Later on, two types of spectra will be identified during the LFN analysis. An ideal spectrum composed of the flicker noise followed by the shot noise (green spectrum in Figure 2.13). The

second one is an affected spectrum by no less than one G-R component (black spectrum in Figure 2.13). Before characterizing and modelling each excess noise component, we will first discuss an important parameter that needs to be considered: the die to die dispersion.

2.7 Dispersion effect on similar HBT geometries

The DC parameters dispersion is one of the major interests for IC manufacturer and was intensively investigated. Die to die DC variation is systematically measured using fully automatic probers and analyzed with statistical data. As for the LFN dispersion, the time needed to obtain sufficient spectra for a statistical approach is problematic. Sanden and al [98] first presented results concerning poly-emitter Si bipolar transistors. Using the same approach, the LFN group in Montpellier obtained results on Si/SiGe HBTs based on 0.25 µm and 0.13 µm BiCMOS technologies [99]. More recently, this effect was investigated on the BiCMOS9MW technology in [84]. Latest results underlining the importance of LFN dispersion study in microelectronic components and systems were presented at the ICNF conference 2019 by Christoforos Theodorou and Gerard Ghibaudo [100] for CMOS transistors.

On BiCMOS9MW, both I-V and LFN analysis presented a certain dispersion effect on similar device geometries from several dice [84]. An identical investigation will be elaborated to testify the dispersion effect on the B55 technology. This study was maintained on six HBTs presenting an identical A_E from 6 dice of the B55 DSA distributed on the wafer.

The evolution of I_B as a function of V_{BE} established on several dice is illustrated in Figure 2.14.a. The dispersion impact on the I-V characteristics was estimated at two bias values, a V_{BE} value around 0.5 V that corresponds to the intersection of both low-injection and diffusion regime and a V_{BE} value of 0.75 V that corresponds to the used bias range during the LFN characterization. A higher dispersion effect was detected for lower V_{BE} values due to the higher impact of G-R and tunnel components on the base current. The dispersion impact decreases from a range value greater than 45 %, at a V_{BE} of 0.5 V, to a dispersion value lower than 20 % for HBTs biased at a V_{BE} of 0.75 V once the diffusion current dominates. Generally, in the rest of the document when analyzing the DC results, the dispersion effect on I-V characteristics will not be considered.

Figure 2.14.b illustrates the dispersion effect on the LFN measurements for identical A_E HBTs. These transistors were characterized in a base current bias range of 50 nA to 500 nA. The presented results in the figure below correspond to an I_B bias of 100 nA. LFN measurements of identical HBTs can either present a dispersed noise level or different noise components. As can be seen in Figure 2.14.b, both 1/f noise and G-R component occurred in the LFN analysis of this representative example. The noise level of the given HBTs varied by less than one decade in the case of ideal behavior (1/f noise followed by shot noise) and by a variation up to 2.5 decades for spectra affected by G-R components. Similar dispersion behavior was observed independently from the I_B values.

Contrary to DC characterization, the dispersion effect will be always considered before LFN analysis. Indeed, measurements were systematically performed on several dice. For the rest of this chapter, as well as in chapter 3, the number of tested dice will be presented for each specific study (as a function of bias current, geometrical parameters, irradiation ...). Hence, as LFN

measurements are time-consuming, the number of tested dice will remain limited. Thus, this will not present a statistical analysis as such, but rather an approach to evaluate the influence of the dispersion. On some figures the obtained results on several dice will be reported. However, for a better visualization on most of the graphs a representative example or, in rare cases, a mean value will be reported.

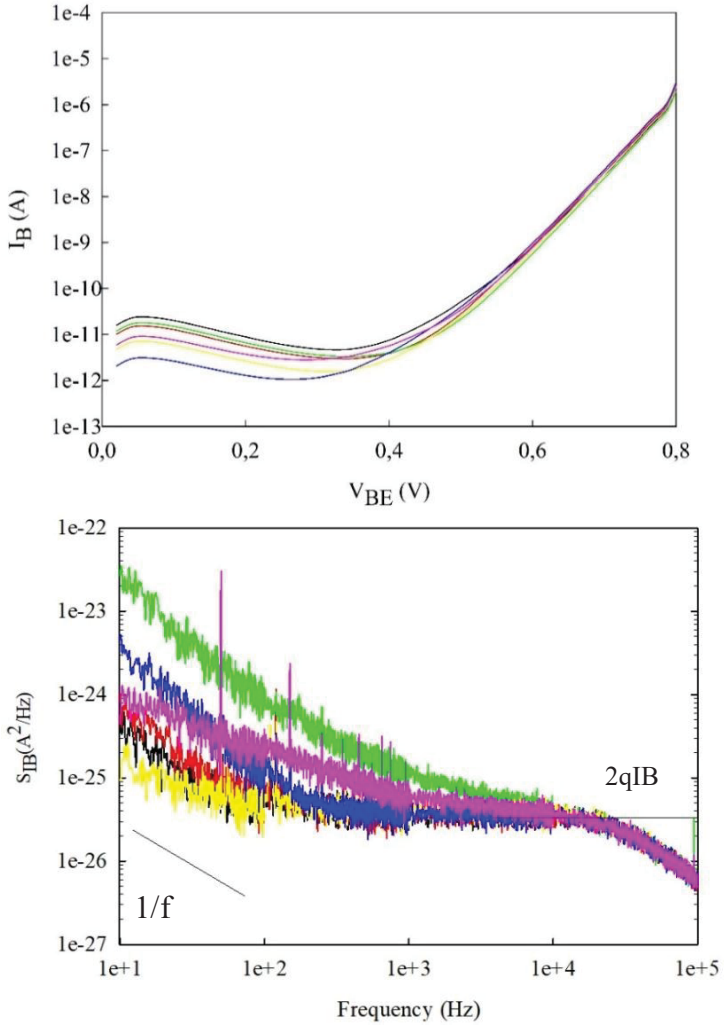

Figure 2.14. Dispersion effect for several HBTs presenting the same emitter geometry on both a) DC and b) LFN measurements.

A statistical study was accomplished as a function of emitter geometries to evaluate a possible dependency of the G-R presence. This study is concluded in Table 2.4 illustrating the percentage of the affected spectra by G-R components for each A_E, a total of 63 HBTs from the B55 DSA are examined. The G-R components presented an independency to the emitter geometries where the 0.6 µm^2 A_E HBTs presented an identical percentage of G-R as the 4.2 µm^2 A_E devices.

A_E (µm^2)	**Spectra affected by G-R components**
0.2	100%

0.6	62%
1	37%
2	25%
3	75%
4.2	62%
10	88%

Table 2.4. Distribution of the G-R components depending on the emitter surface A_E.

Contrarily to the published results in [84] for the BiCMOS9MW technology, a random distribution of the G-R components occurs in the studied HBTs of the B55 DSA. A similar behavior impact was found for the B55 TH. Thereby, the distribution of the G-R components is independent to the A_E parameter, while G-R presence was more pronounced in small area devices for BiCMOS9MW technology.

A study of the dispersion effect was established on the two tested BiCMOS technologies independently to their A_E. The analysis revealed a more conspicuous G-R component presence in the B55 technologies comparing to the BiCMOS9MW one. The distribution of the noise components is presented in Table 2.5 for each technology. 80 % of ideal spectra were found for the BiCMOS9MW HBTs contrarily to the B55 technologies which did not exceed a total of 40%. These percentages can be slightly modified depending on the selected devices and their distribution on the wafer.

A detailed study was accomplished on the three collector structures HS, HV and MV of the B55 TH to investigate a possible impact of the collector structure on the base noise components. A negligible difference was revealed by presenting a similarity in the noise source percentage listed in Table 2.5. Its impact on the input LFN spectral behavior regarding the presence of G-R components is found negligible. Since the only variable parameter between the three structures concerns the collector doping level, its results seem logical.

Since LFN measurements are a time-consuming process, only HS devices were examined in the B55 DSA and as can be seen in Table 2.5 the result is coherent with the B55 TH.

	BiCMOS9MW	**B55 TH**			**B55 DSA HS**
		HS	**MV**	**HV**	
1/f noise	80 %	35 %	30%	25 %	35 %
G-R components	20 %	65 %	70 %	75%	65 %

Table 2.5. Noise components partition for each BiCMOS technology.

2.8 Characterization and modeling of the input excess noise components

As presented in the previous section, a dispersion effect results from the LFN measurements of identical A_E HBTs. To reduce its impact on the LFN analysis, several dice were selected from each technology homogenously distributed on a quarter of the given wafer. Since LFN spectroscopy is time-consuming, a limited number of dice was investigated for each technology. Concerning the study of the three collector structures, an average of 20 devices per structure were undertaken. While for the second study, a total of 63 and 45 transistors were examined for each B55 flavor and BiCMOS9MW respectively.

In the first paragraph, the fluctuation of the input current of the transistor, S_{IB}, will be initiated with a global spectral analysis. Then, the study of the 1/f noise component presenting the main part of this section will be discussed. The 1/f noise will be studied, analyzed and modeled first as a function of the three collector structures and second as a function of the two B55 flavors (TH and DSA) compared to the BiCMOS9MW one. Each study is accomplished in a distinct current bias range of 100 nA - 1 µA and 50 nA - 500 nA for the first and second studies respectively and versus geometrical parameters. The localization of the 1/f noise sources as well as Figure –Of-Merit will be discussed.

In the last part of this section, G-R components of the B55 technology will be studied. This study is established in a current bias range of 50 nA - 500 nA. The plateau magnitudes and the cut-off-frequencies depicting the G-R components will be investigated as a function of current bias and geometrical parameters.

The interpretation of these results will allow the extraction of the compact model parameters for both 1/f noise and G-R components. The extraction of the parameters will be interpreted as a function of the base current bias and the emitter geometries to highlight the localization of the LFN sources of the associated excess noise components.

2.8.1 Spectral behavior

As presented in section 2.6, LFN spectroscopy can present two types of spectra: ideal spectra and spectra affected by G-R components. Figure 2.15 illustrates spectral density of the input current S_{IB} for the three collector structures (HS, HV and MV) of the B55 TH. The presented spectra represent a 1 μm^2 A_E HBT biased by an I_B of 100 nA.

The illustrated HBTs in the Figure 2.15 presented a more or less distinct LF response one from another. The HS device (black curve) respected an ideal behavior while HV device (red curve) has presented a 1/f noise (in the frequency range 10 – 100 Hz) followed a G-R component in the frequency range of 100 – 1000 Hz. As for the MV device (green curve), a G-R component ($G\text{-}R_1$) dominating the 1/f noise is observed in the frequency range 10 – 100 Hz followed by a second G-R component ($G\text{-}R_2$). The shot noise $2qI_B$ was not reached for the MV device.

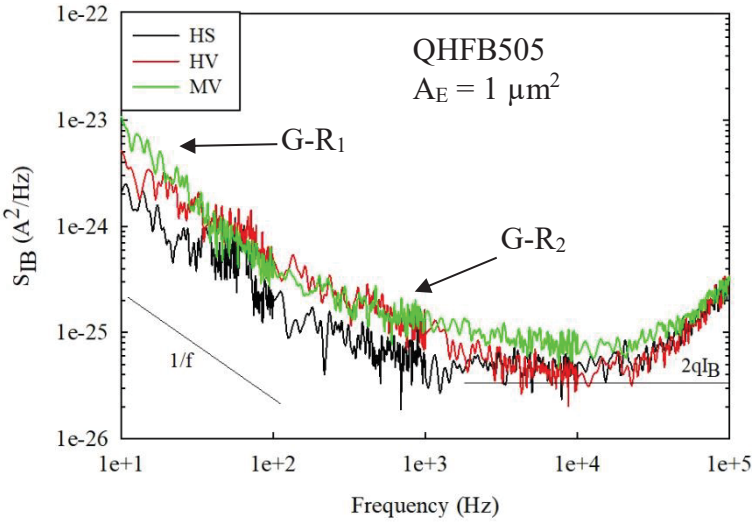

Figure 2.15.Input current spectral density of the collector structure B55 TH for I_B value of 100 nA.

Figure 2.16 illustrates an example of spectra obtained on the two B55, TH and DSA. The illustrated spectra are issued from a 4.2 µm^2 A_E HBT of each flavor in bias range between 50 nA and 500 nA.

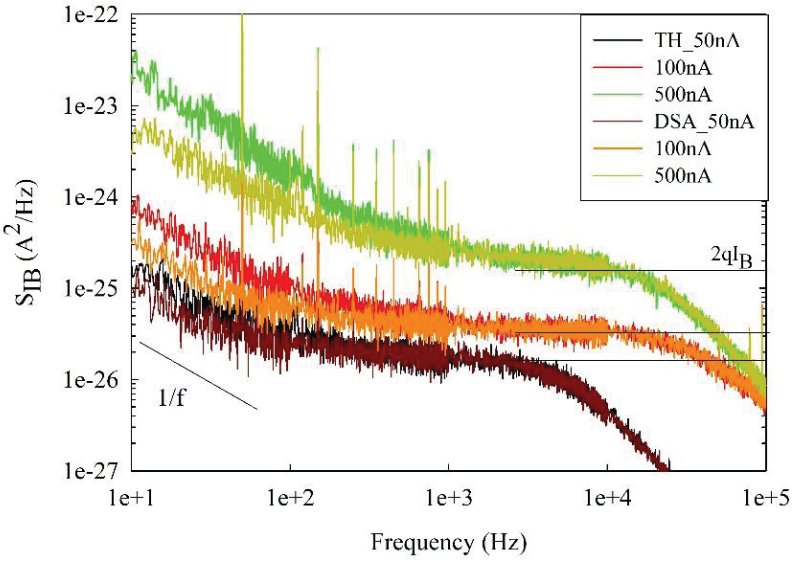

Figure 2.16. LFN measurements of B55 DSA versus TH for the noise level of a 4.2 µm^2 A_E HBT.

A negligible impact of the distinct activation techniques is observed on the 1/f noise level for the 50 nA I_B bias. On the contrary, an improved 1/f noise level is observed for the 100 nA I_B bias with a decrease in the noise level by half of decade for the B55 DSA. As for the 500 nA I_B bias, a modification in the noise component has occurred between the B55 TH and the B55 DSA, with the presence of G-R components disallowing the comparison of the 1/f noise level one with another. The behavior of the 1/f noise component was repeatedly observed during the entire comparison process. Thus, this qualitative trend can be related to the better control of dopant activation techniques of the B55 DSA.

Regarding the different types of transistors or technologies, a quantitative approach of the excess noise components will be given in the next paragraphs.

2.8.2 1/f noise analysis

Once HBTs presented an ideal behavior (flicker noise followed by the shot noise $2qI_B$), the 1/f SPICE compact model, presented in chapter 1 ($S_{IB} = K_F \frac{I_B^{A_F}}{f^{\gamma}}$), can be employed to analyze the unambiguously existing 1/f noise component.

The extraction of the SPICE parameters (γ, A_F, K_F) is provided in detail in the first chapter section 1.4.1. It allows to compare the evolution of the technology and to locate the origin of the noise sources to highlight the defected area of the device.

First, the analysis will occur in response to the three collector structures of the B55 TH presented in Table 2.2. An average of 5 to 7 devices per collector structure were studied. Then, the second analysis will occur in response to the two flavors of the B55 technology listed in Table 2.3 that will be also compared to the mature BiCMOS9MW technology. A total of 22 and 36 HBTs of B55 and BiCMOS9MW, that presented ideal spectra, were examined.

2.8.2.1 Analysis in response to the collector structures

At first, 1/f spectral density S_{IB} at 1 Hz is plotted as a function of the input current I_B. These results, presented in Figure 2.17, enable the extraction of the A_F parameter. The results expressed in Figure 2.17.a, Figure 2.17.b and Figure 2.17.c correspond to three collector structures with distinct A_E each 2 µm2, 1 µm2 and 4.2 µm2 respectively.

The studied HBTs presented a quadratic evolution of the S_{IB} at 1 Hz in response to I_B independently to the collector doping level and the A_E. The extraction of a slope value of 2 (A_F = 2) is considered a typical behavior exploited in the low-frequency community [17] according to the physical models introduced in chapter 1. The 1/f noise levels presented in the figures below describe a dispersed noise behavior comparing the collector structure one with another. In all cases, the 1/f noise level difference between of each structure is in the range of one decade. Therefore, an independency of the collector doping level to the 1/f noise level can be assumed.

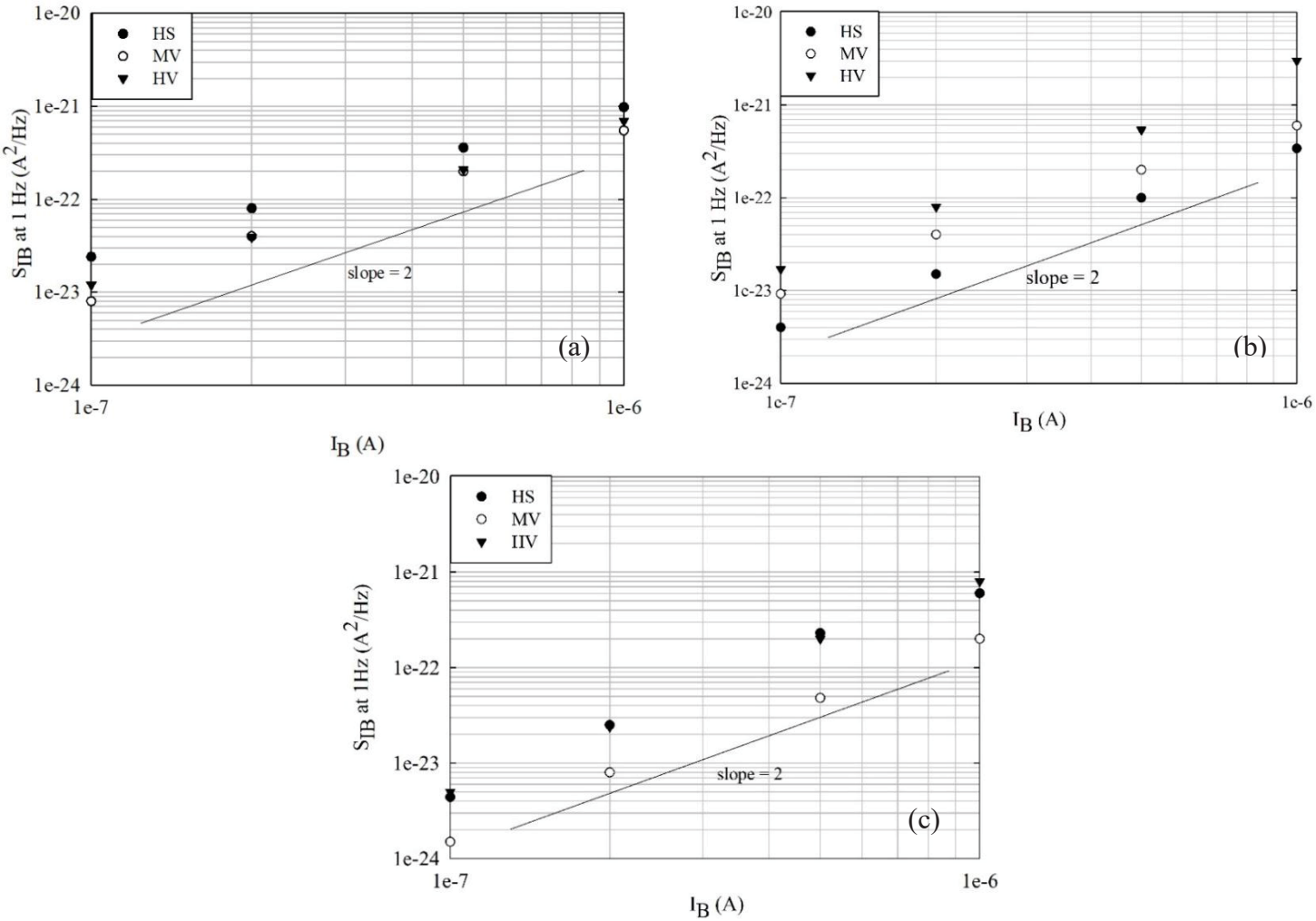

*Figure 2.17. 1/f noise level comparison between HS, HV, MW for of the B55 technology for a)0.2*10 µm², b) 0.2*5 µm² and c) 0.42*10 µm².*

Given that the quadratic evolution of S_{IB} at 1 Hz as a function of the I_B is respected, K_F values can be extracted from the SPICE model. In this case, K_F is a unit less parameter that is expressed as followed:

$$K_F = \frac{S_{IB\ at\ 1Hz}}{I_B^2} \qquad 2.14$$

Once K_F parameters are extracted, the noise level can be plotted as a function of the emitter area A_E. This study is reported in Figure 2.18 for the three collector structures and for several dice, resulting in scattered data. Nevertheless, independently to the collector doping level, a similar tendency is observed by presenting an inverse proportional dependency of the 1/f noise level to A_E. This effect is systematically observed for devices presenting G-R free spectra. The $1/A_E$ dependency is considered as a typical behavior extracted through previous similar studies [17].

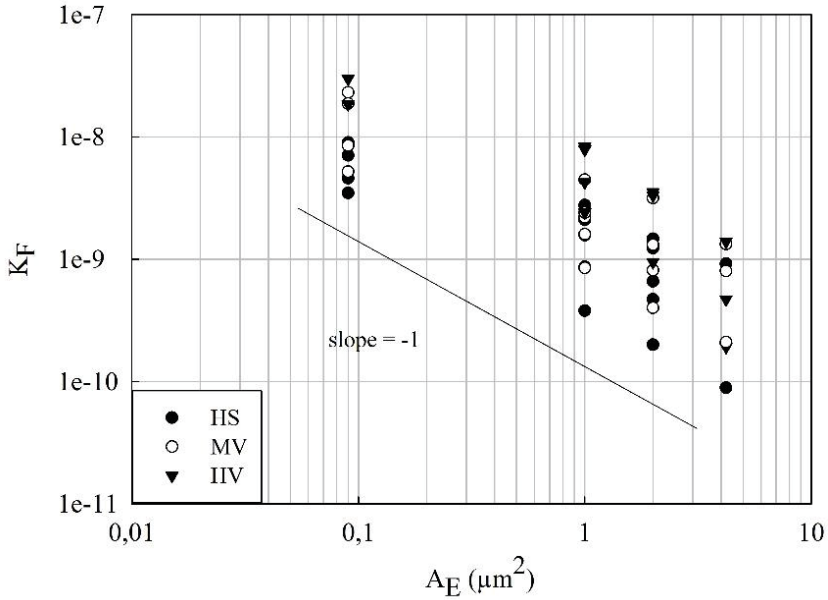

Figure 2.18. Figure-Of-Merit, K_F (A_E), comparison for the three collector structures.

Since K_F is inversely proportional to the A_E, a Figure-Of-Merit K_B can be directly employed from the following expression:

$$K_B = K_F A_E \qquad 2.15$$

The Figure of Merit K_B, is a very convenient FOM often used to compare the 1/f noise level of HBTs produced from different manufacturers.

K_B values can be directly extracted from Figure 2.18 at A_E value of 1 μm^2. An average K_B value is estimated around 10^{-9} μm^2. This average value is slightly higher to the mean value obtained of a full wafer of the BiCMOS9MW ($6\ 10^{-10}$ μm^2) [84]. Hence it is really difficult to find a significant influence of the collector doping level. We can conclude that the 1/f noise level does not depend on the collector doping level, this is coherent with the general hypothesis concerning the localization of the 1/f noise sources in modern bipolar transistors which is to incriminate the intrinsic Emitter-Base junction.

In this section, a comparison for the three collector structures was accomplished. As usually observed in the bipolar transistors, the 1/f noise dependency to I_B^2 and $1/A_E$ was found. However, no clear impact of the collector doping was observed on the 1/f noise level.

2.8.2.2 Analysis of the two flavors of the B55 compared to the BiCMOS9MW

The 1/f noise analysis of the two B55 (DSA and TH) and its comparison with BiCMOS9MW technologies was carried on components presenting an ideal behavior (free G-R spectra) from the HBTs listed in Table 2.3. The analysis will be established as a function of the input current level and the emitter geometries.

2.8.2.2.1 1/f noise study as a function of I_B

The evolution of the S_{IB} at 1 Hz plotted as a function of I_B is depicted in Figure 2.19 for the three types of transistor. The selected HBTs present a 0.81 µm^2 and a 1 µm^2 A_E components for the BiCMOS9MW and the B55 technology respectively. Independently to the BiCMOS technology, a quadratic evolution of the S_{IB} at 1 Hz was found in response to the I_B level. Thereby, a value of 2 can be attributed to the SPICE parameter A_F for the plotted devices. The same I_B dependency (I_B^2) was systematically concluded independently to the A_E for all of the tested HBTs.

The variations of the 1/f noise level, for the presented transistors, are lower than the expected dispersion factor which disallow the extraction of a reliable interpretation. Nonetheless, after the characterization of 8 to 9 dice from each technology, the illustrated results in Figure 2.19 can be considered as a representative behavior for the tested HBTs. The S_{IB} at 1 Hz level of the B55 DSA was found comparable to the lowest one detected for the BiCMOS9MW while a higher noise level was extracted for the B55 TH. The statistical approach for the die to die dispersion will be estimated by the K_B value in next paragraph.

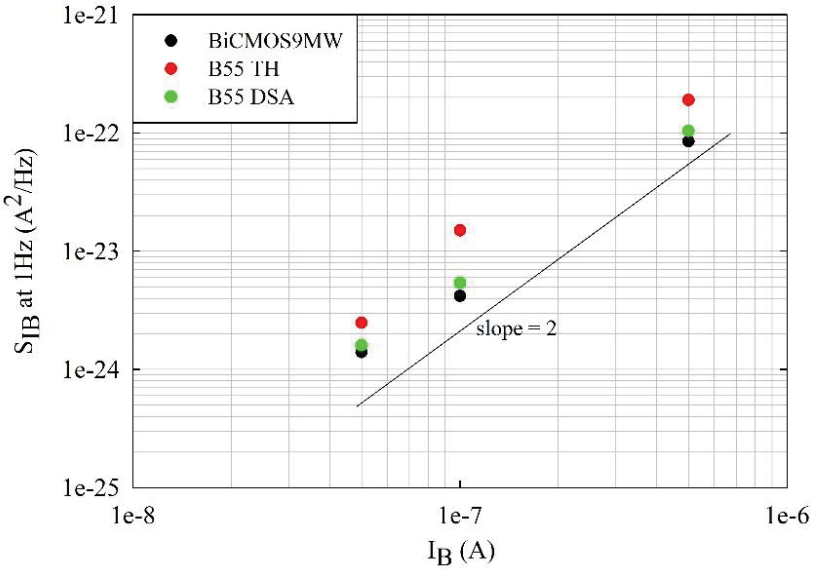

Figure 2.19. 1/f noise level comparison of 0.81 µm2 and 1 µm2 AE HBTs respectively for the BiCMOS9MW and the two B55 technologies.

Thereby it can be initiated that the better control of the dopant activation of B55 DSA improved its performance by reducing its noise level to present a comparable noise response to the mature BiCMOS9MW technology.

2.8.2.2.2 1/f noise study as a function of A_E

Once the quadratic law evolution of the 1/f noise in response to I_B is respected, the unit less K_F parameter can be extracted from the SPICE model presented in 2.14. The further step is by plotting the K_F values as a function of the selected A_E HBTs. This study is illustrated in Figure 2.20 for the three types of HBT which covers an A_E range greater than one decade. By considering the

dispersion effect that was recorded on multiple dice, an inverse dependency to A_E can be extracted. This tendency was respected independently from the BiCMOS technology.

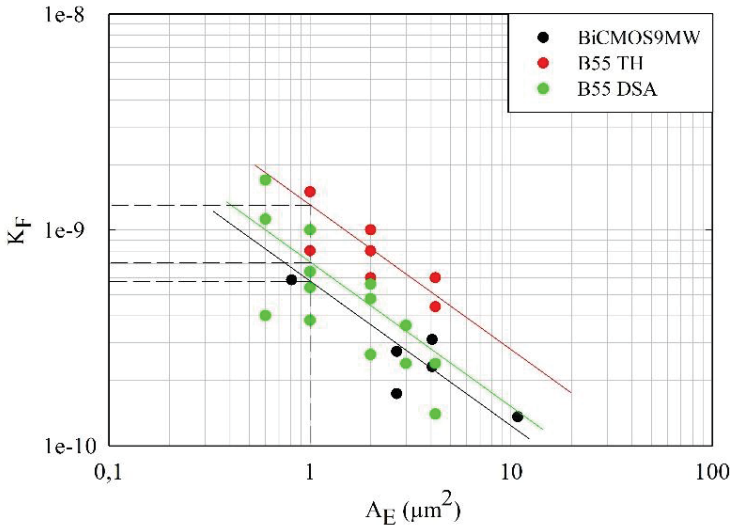

Figure 2.20. The evolution of K_F in response to A_E for three selected BiCMOS technologies.

Given the fact that the $1/A_E$ dependency was respected, the FOM, K_B, can be extracted either by graphical extraction for A_E of 1 µm^2 or by relation 2.15.

The graphical extraction of K_B parameter presented three mean values 6 10^{-10} µm^2, 7 10^{-10} µm^2 and 1.5 10^{-9} µm^2 for the BiCMOS9MW, the B55 DSA and the B55 TH respectively. The K_B values recorded on the selected B55 DSA and BiCMOS9MW components, are found to be nearly a decade higher from the best value of 6.8 10^{-11} µm^2 reported in [101] from earlier studies on BiCMOS9MW technology. This last K_B value resulted from one single die. However, the extracted value (5.8 10^{-10} µm^2) is in the range of the average one obtained during the statistical study of the 1/f dispersion undertaken on a full BiCMOS9MW wafer [98].

The extracted K_B values confirm the better noise performance of the B55 DSA which can be a direct impact of the better control of dopant activation method and thus a better electrical quality of the deposit layer. Nonetheless, it can be an indirect impact to the activation method that results in a better control of the E-B electrical junction depth. The impact of the electrical E-B junction depth was previously investigated and resulted in a decrease of the 1/f noise level along with the increase of its depth [102]. This effect can be related to decreasing the interaction of the minority carriers with the interface states located at the poly/mono-emitter interface.

2.8.2.2.3 1/f study as a function of P_E/A_E ratio

The investigation of the 1/f noise sources as a function of the emitter perimeter P_E is an important study that allows narrowing the suspected E-B area of the noise source location. Figure 2.21 represents the evolution of S_{IB} at 1Hz as a function of P_E/A_E ratio for the three selected I_B currents of each technology. This study can be considered in some cases as a complex study due to the geometrical limitation of the components (i.e. effective dimension, distinct masks and limited data range).

A negligible impact of the emitter perimeter on the S_{IB} is recorded for the three types of transistors by maintaining a stable S_{IB} level independently to the applied current bias. Moreover, as already mentioned, the 1/f noise level of the B55 DSA presented a comparable noise level to the mature BiCMOS9MW technology while a higher level was slightly detected for the B55 TH. This effect is most evident for higher current bias, I_B value of 500 nA.

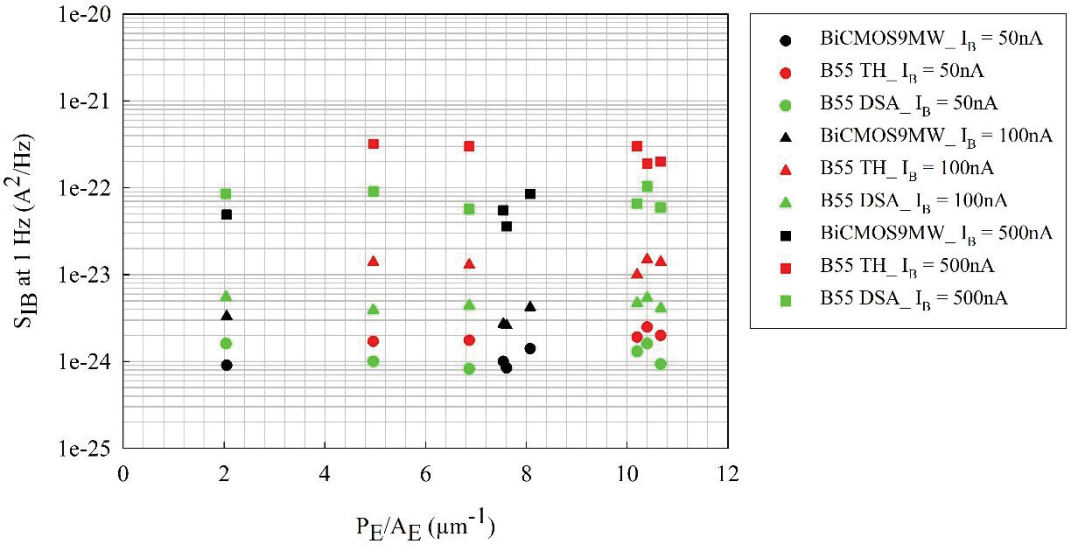

Figure 2.21. 1/f noise level, for the three types of transistor, as a function of the P_E/A_E.

The illustrated behavior in the figure below was systematically observed for the characterized HBTs. The extracted tendency suggests that the 1/f noise components are distributed at the emitter area independently to its periphery.

2.8.2.3 Localization of the 1/f noise source

To highlight the sensitive area of the HBTs related to the existing 1/f noise sources, the presented studies in 2.8.2.2.1 and 2.8.2.2.2 2.8.2.2.2and 2.8.2.2.3 are necessary. The analysis of the three types of transistors (B55 TH, B55 DSA and BiCMOS9MW) presented similar tendencies in response to I_B, A_E and P_E with a distinct noise level. Therefore, the localization of the 1/f noise sources and their physical origin will be introduced without specifying the BiCMOS generation.

Based on the physical models and earlier studies in this field, the quadratic evolution of the 1/f noise level as a response to I_B and its proportionality to $1/A_E$ led to suspect a surface distribution of the 1/f noise sources in the E-B area. This was already deduced by several studies on bipolar transistors [101][52][103][86]. The independencies of 1/f noise level to the collector doping confirms, indirectly, the predominance of the E-B area. The non-dependency to the P_E parameter confirms the suspected surface effect. Some authors proposed as a more precise localization of the 1/f noise sources the intrinsic poly/mono silicon interface [103][46][36] (see Figure 2.22).

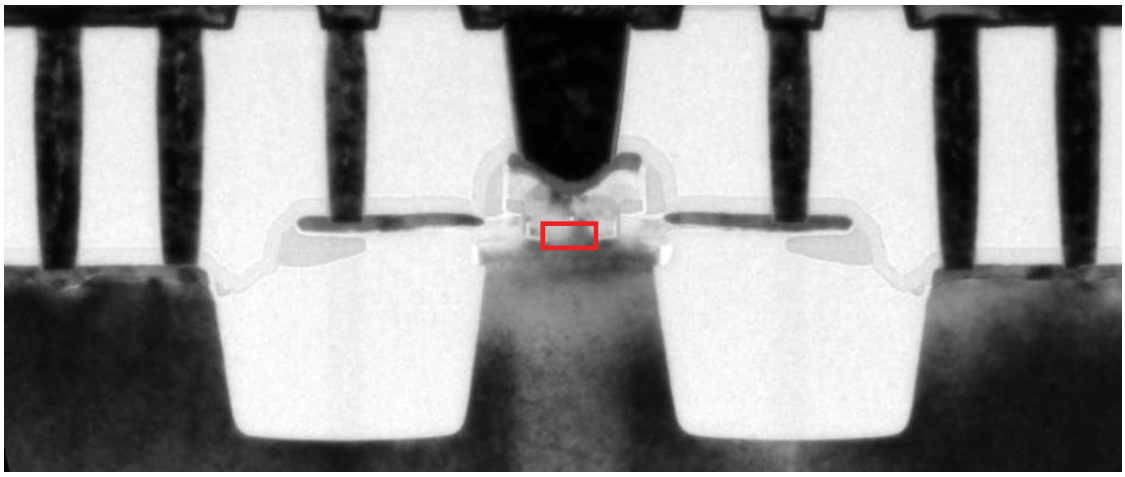

Figure 2.22. Localization of the 1/f noise source from a TEM capture of the HBT device.

2.8.2.4 Figure-Of-Merit fc/ft

The FOM f_c/f_t ratio combines the performance of transistor in both Low-Frequency noise and High-Frequency domain. f_c represents the 1/f noise corner frequency that provides direct information on the device's 1/f noise level while f_t represents the transition frequency that reflects the device's performance in HF.

f_c can be extracted by either the SPICE model when I_B^2 law is respected or by a graphical extraction. The extraction of f_c through the SPICE model is given by expressing $S_{IB}^{1/f} = S_{IB}^{shot\ noise}$. Hence, f_c is presented as followed:

$$f_c = K_F \frac{I_B}{2q} \qquad 2.16$$

As for the second extraction method, Figure 2.23 illustrates the graphical extraction of the fc value. It corresponds to the intersection of the 1/f noise component and the shot noise $2qI_B$. The selected spectrum presents an f_c value of 250 Hz.

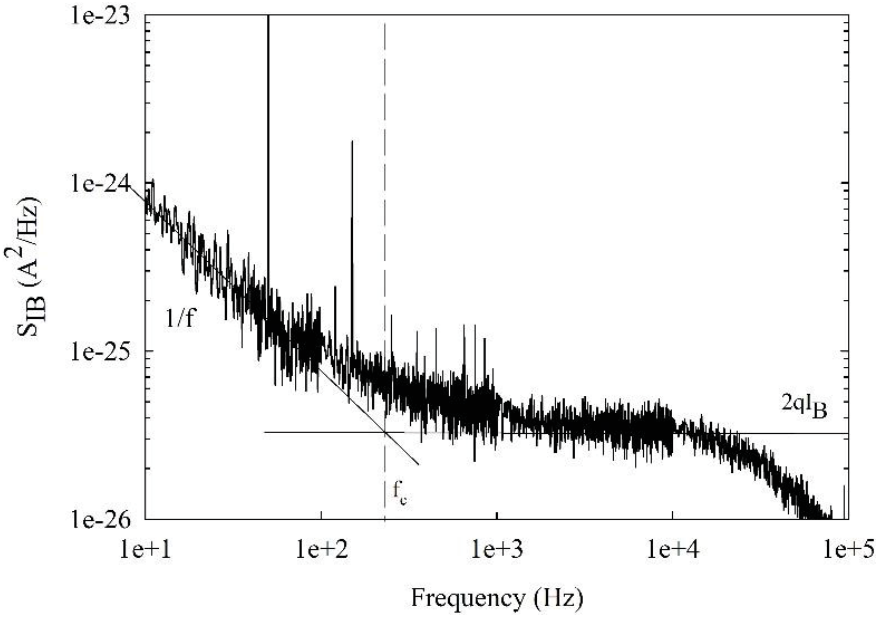

Figure 2.23. Extraction method of the corner frequency f_c value.

f_t values are graphically extracted from a given graph provided by STMicroelectronics. The latter describes the evolution of the f_t level in response to the collector current density J_C. An example was previously provided in Figure 2.5 for B55 TH and B55 DSA.

From relation 2.16, f_c can be expressed as function of J_C:

$$f_C = K_B \frac{J_C}{2q\beta} \qquad 2.17$$

Since both f_t and f_c presented a dependency on the current collector density, f_c/f_t ratio is expressed in response to J_C.

Figure 2.24 represents f_c/f_t ratio of the two BiCMOS technologies as a function of J_C. Similar behavior was observed independently to the BiCMOS technology which describes a stable f_c/f_t level till a J_C value of 1-2 mA/µm^2 followed by a linear increase.

By comparing the two technologies, the lowest ratio is found for the mature BiCMOS9MW technology through its lower K_B values. Nonetheless, the B55 DSA presented a better frequency performance than the B55 TH, closer to the BiCMOS9MW. Despite the better LFN performance of the BiCMOS9MW, B55 f_c/f_t ratio is similar to the BiCMOS9MW one thanks to its improved high frequency performance.

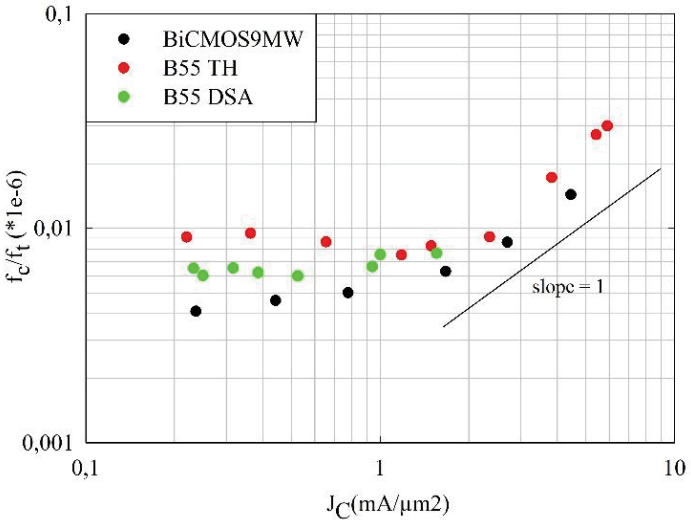

Figure 2.24. FOM, fc/ft ratio, for the three characterized BiCMOS technologies

The evolution of f_c/f_t ratio can be modeled by the following expression [104]:

$$\frac{f_c}{f_t} = K_B \frac{\Pi}{q} \frac{J_C}{\beta} \left(\tau_F + V_t \frac{C_t}{J_C} \right) = \frac{K_B \Pi}{\beta q} \left(\tau_F J_C + V_t C_t \right) \qquad 2.18$$

where τ_F is the forward transit time, V_t is the thermal voltage and C_t is the total junction depletion capacitance per unit area.

For J_C values lower than 2 mA/µm^2, V_tC_t dominates $\tau_F J_C$ presenting a capacitance effect by maintaining a stable level. While at higher J_C values, higher than 2 mA/µm^2, a linear increase of the ratio level occurs in response to J_C. The extraction of C_t values presents a challenging task where the dispersion factor could significantly affect its value. The dispersion factor can influence both the corner frequency f_c extraction and the transition frequency f_t extraction. However, a C_t value was estimated in the range of 20 fF/µm^2 for the three tested transistor types. Even though this method is not accurate, the extracted C_t value from the experimental study is with agreement with STMicroelectronics values.

2.8.3 G-R components analysis

The G-R components, contrarily to the 1/f noise, present a more restrained field of study in the LFN community of Si based bipolar transistors. Their presence became more pronounced in Si/SiGe:C HBTs. These components are not systematically observed on each device as presented in section 2.6, Table 2.5. Therefore, a statistical study is needed at first to detect their presence.

As previously mentioned, 8 to 9 dice were characterized resulting in a total of 41 and 9 HBTs affected by G-R components from B55 and BiCMOS9MW respectively. Therefore, G-R analysis will be mainly established for the B55 technology in this section.

Once HBTs are affected by G-R components, Lorentzian shape can be retrieved from its LFN spectroscopy. Each Lorentzian is defined by a distinct plateau magnitude and a cut-off frequency. In this section, the extraction methods of these parameters will be presented in addition to their

compact modeling. The presented study in this part is given to explore some tendencies that will be needed for the irradiation response investigation in the next chapter.

Most often, G-R components were related to RTS components represented by a square signal in the time domain (see Figure 2.13). To study this component in the time domain, more than 20 records are needed to extract a reliable time constant. First approach and result were presented on BiCMOS9MW in [105]. More recently, B55 devices were studied by the University of Modena and Reggio Emilia in Italy [106], partners in TARANTO project.

2.8.3.1 G-R analysis

Mainly, the non-ideal spectrum related two G-R components which is modeled using the presented G-R compact model (i.e. two Lorentzians) in equation 1.24:

$$S_{IB\ G-R} = \frac{A_1}{1+(\frac{f}{f_{c1}})^2} + \frac{A_2}{1+(\frac{f}{f_{c2}})^2} \qquad 2.19$$

where (A_1, f_{c1}) and (A_2, f_{c2}) represent the first and the second Lorentzian parameters (plateau magnitude, cut-off frequency).

Two methods occur to extract the Lorentzian parameters. They can be established through a developed software or by plotting S_{IB}*f as a function of the frequency. In this work, the extraction method used is a developed software on Matlab which allows to deliver a more accurate extraction of the parameters. Figure 2.25 presents a screen caption of the interface presenting both G-R components.

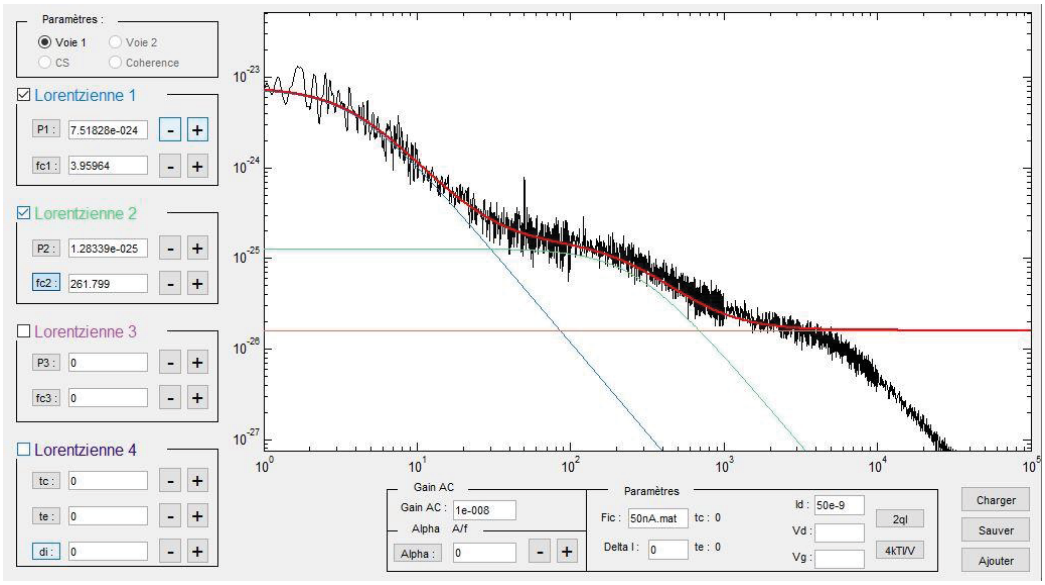

Figure 2.25. Lorentzian parameters extraction via MATLAB interface.

The fitted parameters (A_i and f_{ci}) for the given example are (7.51 10^{-24} A^2/Hz, 4 Hz) and (1.28 10^{-25} A^2/Hz, 260 Hz) for the two G-R components. Independently to A_E and I_B, cut-off frequencies

were found in the frequency range of 20 Hz and 200 Hz for the first and the second Lorentzian respectively.

A RTS study was established on the same technology in [106] to extract the RTS properties (magnitude, time capture and emission). Two discrete RTS levels were examined. A time constant τ in the range of 0.77 ms was explored equivalent to an f_{ci} in the range of 206 Hz which correspond to the second extracted G-R component. However, no sufficient information was given to extract the time constant of the first one. Moreover, investigations on Si/SiGe HBTs developed by Infineon in [86] resulted in two G-R components related to RTS noise. The first one presents an average time constant (τ) in the range of 25 ms equivalent to a f_{ci} of 6 Hz while the second one presents an average τ value in the range of 1 ms equivalent to 150 Hz.

Earlier studies concerning Si [102][103][86][106] and III-V [107][4][81] HBTs highlighted that G-R noise components are mostly originated in the E-B region near the E-B space charge region. Additional studies in [82] highlighted the localization of these trap centers at the E-B periphery. Recently, Unimore group investigation's on the B55 technology in [106] reported an independency of the time constants (τ_c and τ_e) to the output bias V_{CE} contrarily to the input bias V_{BE}. Hence, the localization of the defects was highlighted at the E-B interface close to the E-B space charge region.

To locate more precisely the G-R noise sources, based on the presented work in [86], we will present further investigations on the mean plateau magnitude A_i as a function of emitter geometries and base current bias. The presented mean values are obtained from 4 to 5 dice of the B55.

2.8.3.1.1 Plateau analysis in response to emitter geometries

Figure 2.26 presents the evolution of the two Lorentzian mean plateau magnitudes, A_1 and A_2, in response to emitter area A_E, both G-R components are analyzed for three I_B biases.

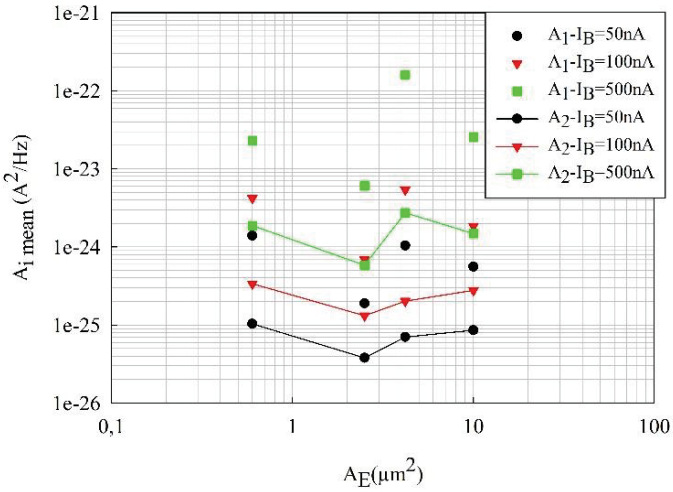

Figure 2.26. First and second Lorentzian mean magnitude level A_i as a function of the A_E.

The first Lorentzian is presented as simple plots while the second G-R is illustrated with additional straight lines. This study is maintained on 4 HBT geometries: 0.6 µm^2, 2.5 µm^2, 4.2 µm^2 and 10 µm^2. Independently to I_B, while considering the dispersion factor, both G-R components presented an independency to A_E. Hence, this tendency underlines a negligible surface impact.

Further investigations were established to narrow the suspected area of the defects localization by examining the perimeter impact on the noise level. This study is presented in Figure 2.27 by plotting the normalized mean G-R magnitude by the emitter surface (A_i/A_E) as a function of P_E/A_E. Each Lorentzian plateau is plotted as a function of the three base currents.

Due to the restricted perimeter geometries, it is problematic to conclude a clear dependency. However, some tendencies can be proposed. As can be seen in Figure 2.27, a decrease in the mean A_i/A_E in response to P_E/A_E is found for the two Lorentzian plateaus. The presented physical model of G-R component in chapter 1 (equation 1.20) presenting a 1/V dependency uphold the $1/P_E$ dependency. This tendency is observed for the three I_B biases. Thereby, the G-R noise sources are suspected to be distributed at the periphery of the E-B junction. The established measurements in [86] presented a peripheral impact as well, however, different P_E dependency were observed comparing to the experimental result in this work.

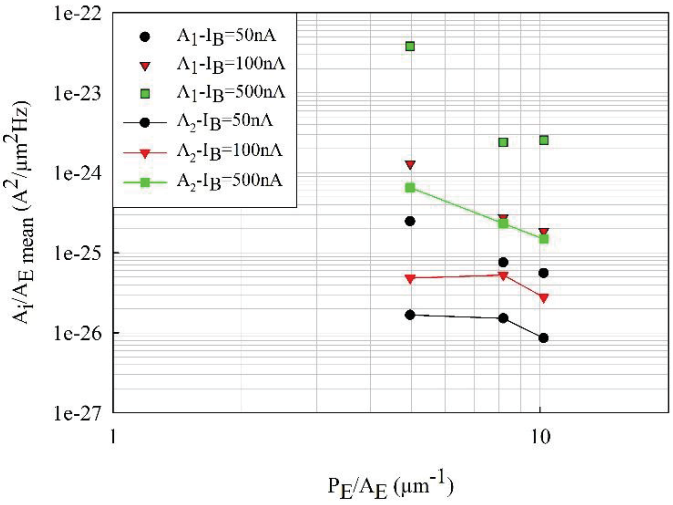

Figure 2.27. First and second Lorentzian normalized mean magnitude level S_{IB}/A_E as a function of the P_E/A_E.

2.8.3.1.2 Plateau magnitude analysis in response to I_B

Moreover, the study of the Lorentzian plateau was examined in response to the current bias. Two A_E HBTs of 0.42*10 µm^2 and 5*0.2*10 µm^2, presented in Figure 2.28, depicts the magnitude plateaus A_i as a function of I_B for both G-R components on several dice.

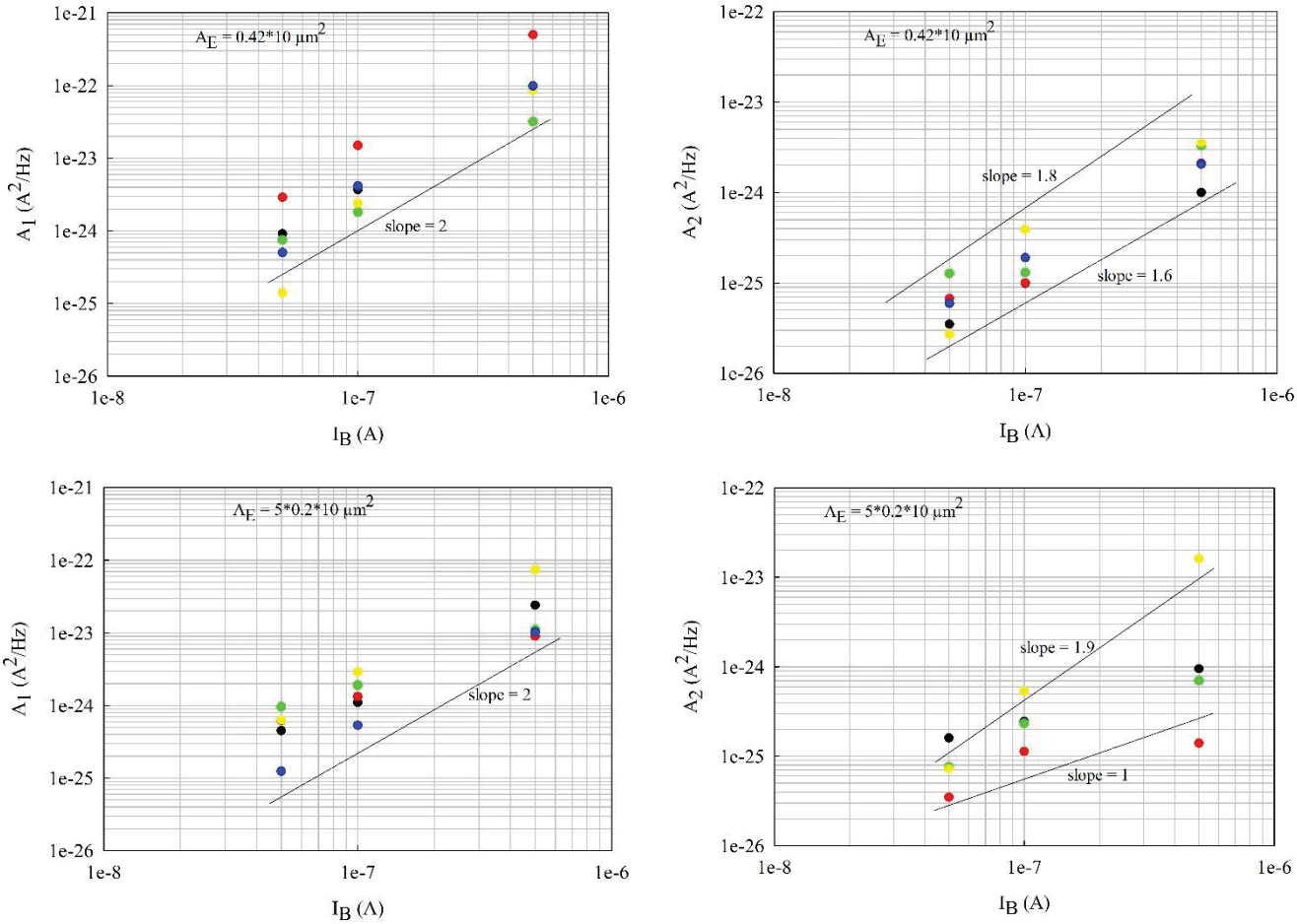

Figure 2.28. First and second Lorentzian mean magnitude level A_i as a function of I_B for two A_E HBTs.

Even though more current biases are required to extract a clear I_B dependency, some tendencies can be observed. By considering the dispersion effect, the first G-R plateau of each A_E clearly presented a quadratic dependency to the current bias (I_B^2 dependency). In contrast, the second Lorentzian component depicted an I_B^{α} dependency where α varies in a range value of 1 to 2 as presented in the right column of Figure 2.28.

Hence, the compact model first approximation of each Lorentzian magnitude can be expressed as followed:

$$A_1 = K_{GR_1} \frac{I_B^2}{P_E} \qquad 2.20$$

$$A_2 = K_{GR_2} \frac{I_B^{\alpha}}{P_E} \qquad 2.21$$

The extraction of compact models presents a delicate interpretation that is limited by several key factors. These limiting parameters are the random presence of G-R components, the disproportion between the mask geometries and the effective geometries, the limited geometrical dimensions range.

Eventually, a $1/P_E$ and an I_B^2 dependency while a $1/P_E$ and an I_B^{α} dependency were extracted for the first and the second G-R respectively. The G-R noise sources are suspected to be located at the periphery of the interface SiO_2/E-B space charge region. The suspected area highlighted for each G-R component is similar to the proposed one in [86][106].

To better locate and investigate the origin of the noise sources, the activation energy E_a of each trap associated to a G-R component must by extracted and analyzed by plotting the Arrheinus graph in either frequency or time domain usually studied in different semiconductor materials and devices [108][109][110][111]. In [81], 4 E_a values were interpreted to distinct the localization in three regions: Si/SiGe, SiO_2 and at the lateral interface of Si/SiGe and SiO_2. In [106], E_a was only presented for the second G-R component with a value of 0.29 eV which was interpreted to traps located in the SiO_2 lateral oxides.

2.9 Conclusion

In this chapter, the high impedance configuration measurement chain was highly introduced to extract the LFN components at the input of the intrinsic HBTs.

Three types of transistors associated to two BiCMOS technologies, BiCMOS9MW and B55, were supplied by STMicroelectronics.

The established investigation is divided into two main categories. The first study held a comparison of the three collector structures of the B55 technology: High Speed, High Voltage, and Medium Voltage. While the second one investigated the two developed flavors of the B55 technology (TH and DSA) and compared to the BiCMOS9MW performance. Each study was initiated by a DC characterization followed by a complete LFN spectroscopy. DC analysis were established by the forward Gummel plots while LFN studies were examined by investigating the input current spectral density S_{IB} study as a function of the base current I_B and the emitter geometries. A sufficient number of HBT devices was selected for each study which allowed to establish a statistical approach.

The three collector structures presented distinct DC performances recording the highest h_{FE} and the lowest BV_{ce0} for HS devices comparing to MV and HV devices. Contrarily to the DC analysis and the HF performances, by considering the acceptable dispersion noise level, the doping level of the collector presented a negligible impact on the noise response. 1/f spectral current density S_{IB} presented a similar typical 1/f noise behavior for the three structures: a quadratic evolution as a function of I_B and an inverse proportionally to A_E. A Figure-Of-Merit (FOM), K_B, allowed the extraction of an average value around 10^{-9} μm^2 for HS, MV and HV devices.

The second study, dependent on the dopant activation techniques, highlighted an improved DC and LFN response. The investigations resulted in an improved K_B value of 7 10^{-10} μm^2 for the B55 DSA comparing to the B55 TH presenting a value of 1.5 10^{-9} μm^2 while the BiCMOS9MW technology presents the best value of 6 10^{-10} μm^2. A second FOM was studied which corresponded to f_c/f_t ratio in response to J_C. This FOM is considered an interesting analysis that combines the device's performances in both High-Frequency response and Low-Frequency noise domain. The extracted tendencies resulted that the B55 DSA revealed a similar behavior to the mature

BiCMOS9MW, a good compromise of both high frequency performance f_t and LFN response f_c was achieved.

Eventually, the G-R components were introduced to lay the basis for the parameter's extraction which will be highly needed in the next chapter. Two G-R components were highlighted from the selected HBTs. Independently to the A_E, the cut-off frequencies were found in the range of 20 Hz and 200 Hz. The magnitude plateaus were investigated as a function of emitter geometries and I_B. This study led to extract compact models for the two G-R components and presented some trends concerning the localization of the defected areas. The $1/P_E$ evolution, found on both G-R plateaus, led to highlight the localization of the defects at the emitter periphery close to the interface oxide / E-B space charge region.

Chapter 3 Heterojunction Bipolar Transistors response after exposure to radiative environments

3.1 Introduction

One of the major restricting factors for integrated circuits is their reliability. Since SiGe HBTs are considered as the prime candidates for many aerospace and military applications, a major interest is found for the irradiation robustness of these devices[112]. Therefore, investigating the irradiation damages mechanisms and their impact on devices characteristics are needed. It can provide accurate information to identify the induced defects and locate the sensitive area. This chapter aims to investigate the induced defaults of the two studied BiCMOS technologies after irradiation exposure.

The first part of this chapter will present a brief introduction to the radiative environments as well as some interaction mechanism with matter and electronics. The presented mechanisms in this chapter are related to the one generated by the used irradiation sources. The investigated sources will depict an X-ray generator and a Cobalt60 source. Each irradiation source presents distinct properties, X-ray irradiations allow to use a higher dose rates while Gamma-ray replicates a more comparable environment to the one found in space.

The second part will be initiated with the irradiation process using the X-ray exposure then the Gamma-ray. Multiple dice will be selected to investigate the irradiation impact of each irradiation source. Several irradiation exposures will be established till reaching a certain Total Ionizing Dose (TID) for X-ray and Gamma-ray. Each step will be followed by both DC and LFN characterizations. The irradiation impact will be investigated on DC through interpreting the Gummel plot and on LFN through interpreting both 1/f noise and G-R components on the base current fluctuation. The induced noise components will be studied as a function of the input current bias and the emitter geometry to locate the defected area in which the induced noise sources occur. DC and LFN results will be interpreted to evaluate the robustness of each technology. To investigate a possible healing effect on both DC and LFN, two annealing processes will take place.

Moreover, further studies will take place to investigate the degradation response of the HBTs in High-Frequency domain after X-ray exposure. S-parameters and Load-pull characterization will be studied.

Eventually, the last part of this chapter will evaluate the induced degradation level of each irradiation source and interpret some complimentary effects.

3.2 Radiation environments impact

3.2.1 Description of radiative environments

Beyond the earth's atmosphere that presents a natural protection layer, several radiation types can be encountered. The first ones are the galactic cosmic rays constituted by highly energetic protons and heavy ions that originate from the outside of our solar system contrarily to the other types. Indeed, the sun represents an important radiation source generating on its surface the solar wind and some erratic explosions called solar flares and Coronal Mass Ejection. These explosions produce a massive amount of energy issued in the form of heavy ions, electrons and protons principally. All these particles are trapped in the earth's magnetic field [113]. These energetic charged particles circling the earth were discovered in 1958 with the beginning of the satellite era,

they are known as the Van Allen radiation belts. Figure 3.1 illustrates the different radiation sources in the earth's space environment.

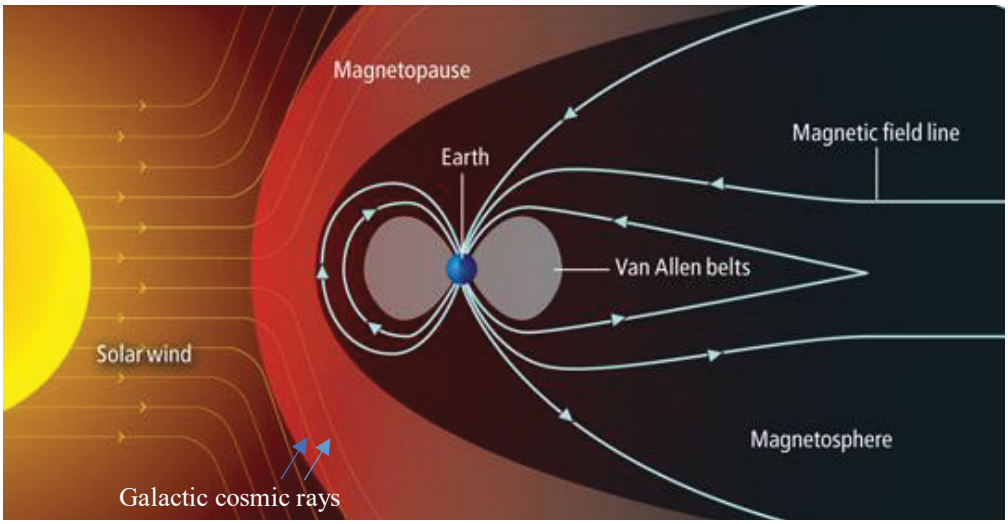

Figure 3.1. Earth's space environment and its radiation sources[114].

Each radiation type emits several kinds of particles that corresponds to a proper energetic range presented in Table 3.1.

Radiation types	Particles	Energy
Galactic cosmic rays	Protons and heavy ions	MeV to TeV
Solar wind	Protons	KeV
	Electrons	eV
Solar flare	Protons and heavy ions	MeV
Van Allen belt	Protons	eV to 500 MeV
	Electrons	eV to 7 MeV

Table 3.1. Characteristics of each radiation type.

Moreover, gamma photons and X-rays can be added to these particles. Gamma could be issued from deep space and X-rays could be produced by the solar flares. Indeed, emissions of X-rays precede the protons arrival (Figure 3.2).

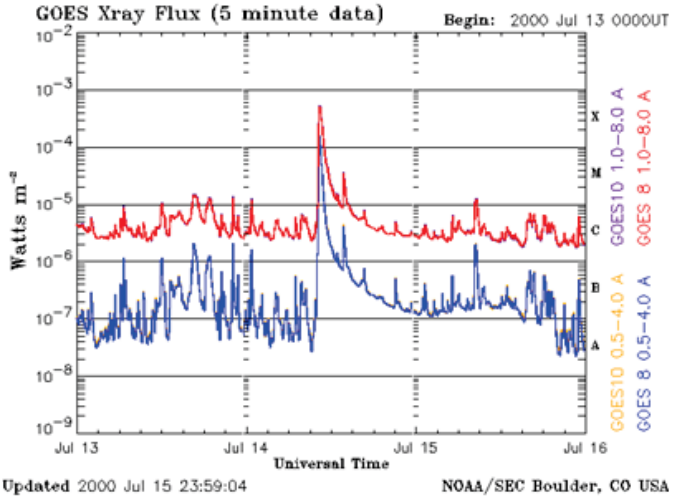

Figure 3.2. X-rays flux issued of the solar flare of the July 14, 2000 [115]

3.2.2 Interaction mechanism with the materials

The interaction mechanisms of particles with atoms is an energy dependent behavior. In this work, the unique investigated particles are the photons. Therefore, collision mechanisms with photons will only be presented. X-rays and Gamma-rays are the most useful means to reproduce on the ground the radiation effects. They are recommended in component and circuit testing standards. It is thus important to understand their interaction mechanisms.

Incident photon collision with atoms can be described by four fundamental behavior: coherent scattering (known as Rayleigh effect), photoelectric effect, incoherent scattering (known as Compton scattering effect), and pair production.

Rayleigh effect describes the interaction of an incident photon with an atom without ionizing nor exciting the atom state. Photoelectric effect corresponds to a total energy transfer, the incident photon is absorbed and an electron is ejected from its binding state. This effect is represented in Figure 3.3.a. Concerning the Compton effect, it occurs once the photon interacted with the matter by ejecting an electron from its biding state while scattering a lower energy photon. This effect is illustrated in Figure 3.3.b. As for the pair production phenomenon, a pair of electron-positron results from the interaction of the photon with the matters. This effect is presented in Figure 3.3.c.

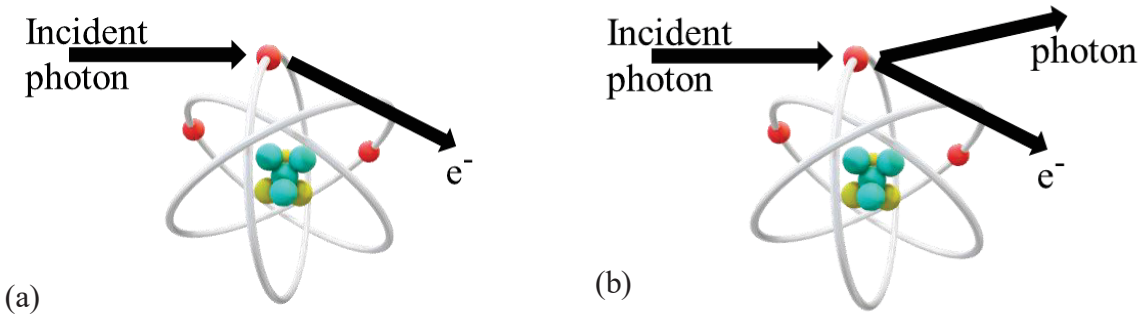

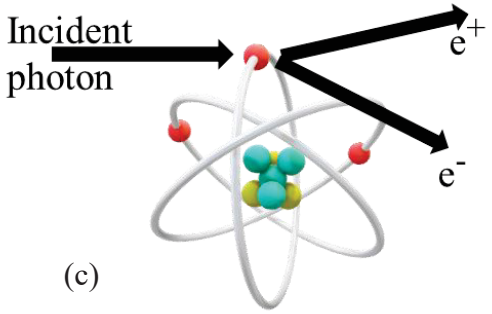

Figure 3.3.Interaction mechanism of photon in (a) photoelectric effect, (b) Compton scattering effect and (c) pair production.

Each of the described interactions dominates in a specific energy range. The dominance of these effects in response to the photon energy is described in Figure 3.4. The photoelectric effect dominates until an energy of 60 keV, then the Compton effect dominates up to an energy of 10 MeV. For higher energy photons, greater than 10 MeV, the pair electron-positron phenomenon dominates.

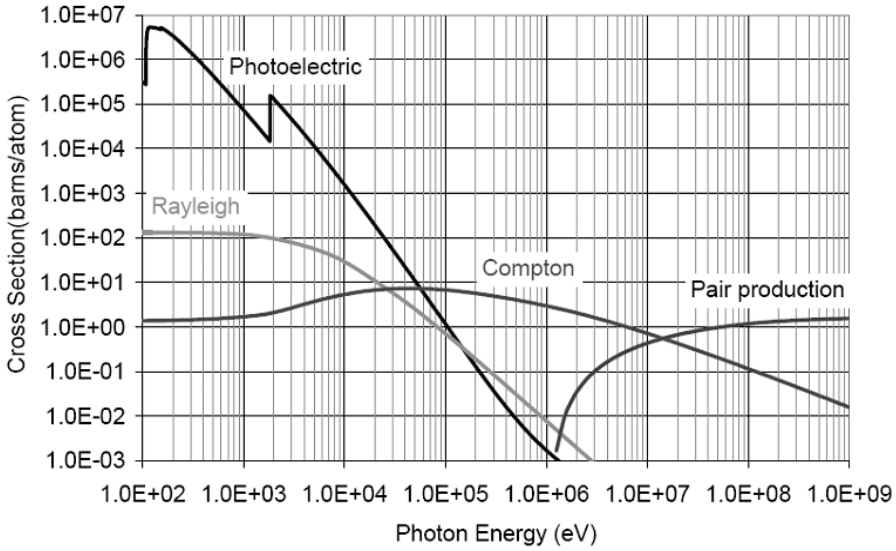

Figure 3.4. Interaction mechanism of photon-material in silicon as a function of photon energy [116].

3.2.3 Irradiation impact on electronics

After irradiation exposure, the produced effects on electronics are sorted into two categories: Single-Event Effect (SEE) and Dose Effect. SEE results from the interaction of a single particle, mainly heavy-ion or proton, with the semiconductor. This effect is not adopted in our study; therefore, it will not be presented in details. The dose effect lies in the interaction of multiple induced particle generating a cumulative dose behavior. This effect can be classified as either a total non-ionizing dose creating some displacement damages or as a total ionizing dose (TID) creating some ionizing damages.

As for the SEE, displacement damages, relate to the interaction of highly energetic particles, mainly protons, neutrons and electrons. Therefore, they will be not presented.

Ionizing damages consists in the interaction of particles or photons with a sufficient energy to ionize atoms or molecules by removing an electron from their orbit and creating a positive charged atom. At the electronic devices' level, these damages result principally in the creation of some interface traps at the silicon-oxide interface and some trapped charges located in the oxide. Since the electron mobility is more significant than the hole's mobility, positive charges will dominate in the oxide. This behavior is illustrated in Figure 3.5.

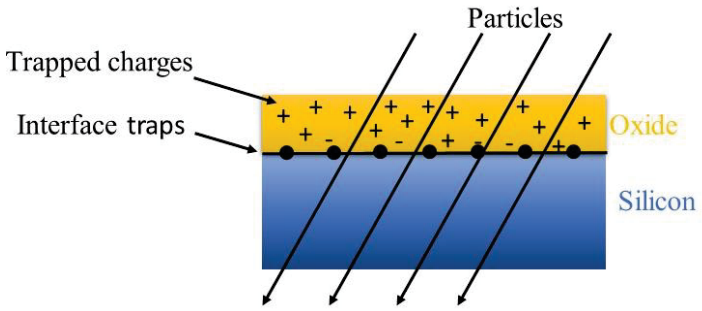

Figure 3.5. Effects on an ionizing dose in a Si semiconductor [117].

3.3 Radiation facilities

The irradiations were established by using a 320 keV X-ray generator and a Cobalt60 source from the University of Montpellier PRESERVE platform located at the IES laboratory. Dose monitoring is accomplished in a plane parallel transmission chamber (type 7862) from PTW in a spectral range of 7.5 keV to 320 keV for the X-ray source and a Farmer ionizing chamber (model 30013) from PTW in a spectral range of 30 keV to 50 MeV for the Cobalt60. These chambers are both calibrated in air and presented in Figure 3.6.

X-ray and Gamma-ray sources are both photon emission techniques. The X-ray source can induce energetic emission spectra in the range of 0-320 KeV. A nominal voltage and current biases of 320KV and 6 mA respectively are used resulting in an energetic emission level of 320 KeV. Two main emission spectra are induced by the Cobalt60 source presenting an energetic level of E_1 = 1.173 MeV and E_2 = 1.332 MeV. By considering the energetic photons emission range of these two sources, based on the Figure 3.4, the interaction mechanisms are the photoelectric and the Compton effects for the X-ray generator while the Compton scattering effect for the Cobalt60 source (two main energies E_1 = 1.173 MeV and E_2 = 1.332 MeV). The induced damages after irradiation exposure, for both sources, consist in the ionizing damages described earlier in Figure 3.5.

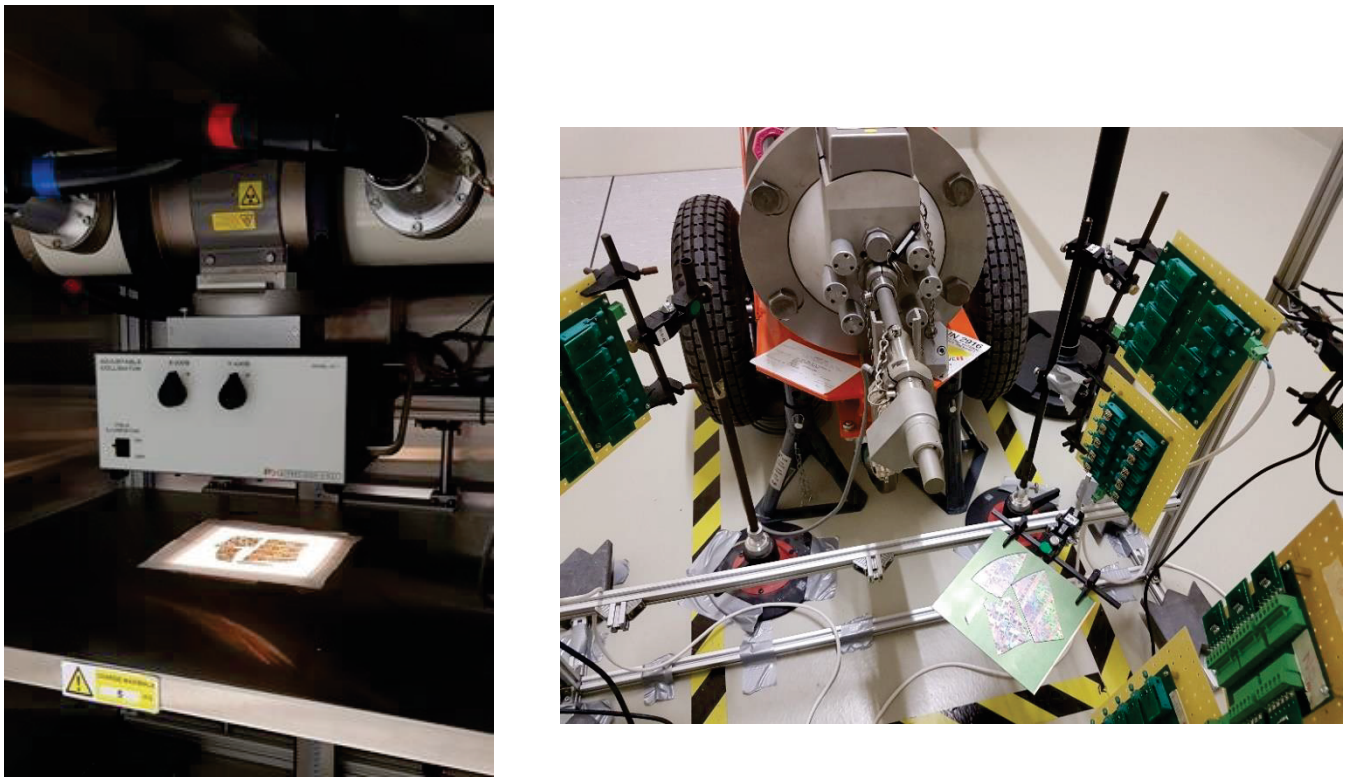

Figure 3.6. Capture the irradiation chamber of the X-ray generator (left capture) and the Cobalt60 source (right capture).

3.4 Studied HBTs

To investigate the irradiation impact on the HBTs, multiple transistors from several dies were selected. The tested components cover an A_E range of 0.8 to 10.8 µm^2 and 0.6 to 10 µm^2, for BiCMOS9MW and B55 respectively. For the B55 transistors, only HS components are examined. The selected HBT geometries are detailed in the Table 3.2. The studied components present multiple architecture that vary from a single finger configuration (i.e. CBEBC) to a multi-finger configuration defined by the number of emitter fingers (i.e. CBEBCBEBCBEBC configuration presenting a three fingers HBT architecture).

Technology	HBT's name	Sample ID	Configuration	W_E (µm)	L_E (µm)	A_E (µm^2)
	NBHSAH	1	1 finger	0.27	3	0.81
		3	1 finger	0.27	5	1.35
	NBHSAI	1	1 finger	0.27	10	2.7
		3	1 finger	0.27	15	4.05
	NBHSAQ	3	5 fingers	0.27	3	4.05

BiCMOS9MW	NBHSAM	3	1 finger	0.4	5	2
	NBHSAO	1	1 finger	1.08	10	10.8
	NBHSAU	1	4 fingers	0.27	10	10.8
B55	QHFB504	HS	1 finger	0.2	3	0.6
	QHFB505	HS	1finger	0.2	5	1
	QHFB506	HS	1 finger	0.2	10	2
	QHFB511	HS	1 finger	0.25	10	2.5
	QHFB514	HS	1 finger	0.42	10	4.2
	QHFB516	HS	1 finger	0.2	5	1
	QHFB517	HS	1 finger	0.2	10	2
	QHFB521	HS	5 fingers	0.2	10	10

Table 3.2. Geometrical characteristics of the irradiated HBTs for both technologies.

To evaluate the die to die dispersion effect (previously exposed in section 2.7), a limited number of dice (semi-statistical approach) was studied. A total of 5 and 6 dice per BiCMOS technology were exposed to X-ray and Gamma-ray sources respectively. To limit the overcharge of the graphs in the chapter, the semi-statistical approach will not be illustrated for devices presenting same tendencies.

3.5 X-ray Irradiation impact on HBTs

Due to the time-consuming electrical characterization (DC and LFN), the high number of selected HBTs and the limited accessibility to the irradiation facilities, we started by investigating a possible relaxation effect between each irradiation step that could occur.

3.5.1 Time interval and measurement impacts on DC and LFN measurements

In this section, time and measurements effects after the first irradiation step (10 krad) are investigated over 12 days. Two HBT geometries are selected from each technology, 0.27*5 μm^2 and 0.4*5 μm^2 for the BiCMOS9MW and 0.2*5 μm^2 and 0.2*10 μm^2 for the B55. Two dice were specifically reserved for this study with a total of 4 HBTs per technology. Both DC and LFN characterization are carried out during this test at 4 states: before irradiation, directly after irradiation exposure, after 5 and 12 days.

Figure 3.7 presents the time relaxation impact on the Gummel plots for the 2 μm^2 A_E HBTs of each technology. On the contrary to the B55, BiCMOS9MW marked a degradation response after exposure. A negligible relaxation impact is detected along the investigated period for I_B and I_C levels of both technologies.

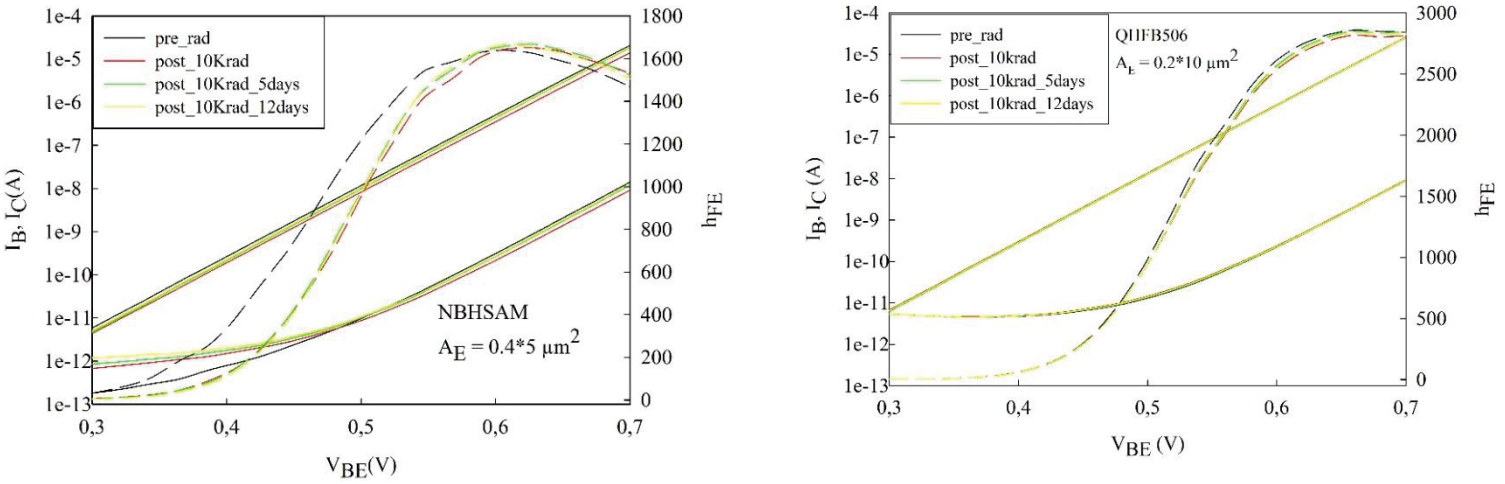

Figure 3.7. Impact of time relaxation on DC measurements for both BiCMOS9MW and B55. Solid lines: I_B and I_C currents – Dash lines: DC current gain h_{FE}.

LFN characterization are presented in Figure 3.8 for the two technologies. 1/f noise level of the BiCMOS9MW HBT exceeded the pristine 1/f noise level by one decade. The induced noise recorded after exposure maintained a stable level, an independency to any relaxation effect was preserved in the following 12 days. Concerning the B55 technology, a stable noise level is respected after irradiation and during the tested period.

LFN results, plotted in the figure below, correspond to an I_B value of 100 nA. The three tested currents presented a similar behavior.

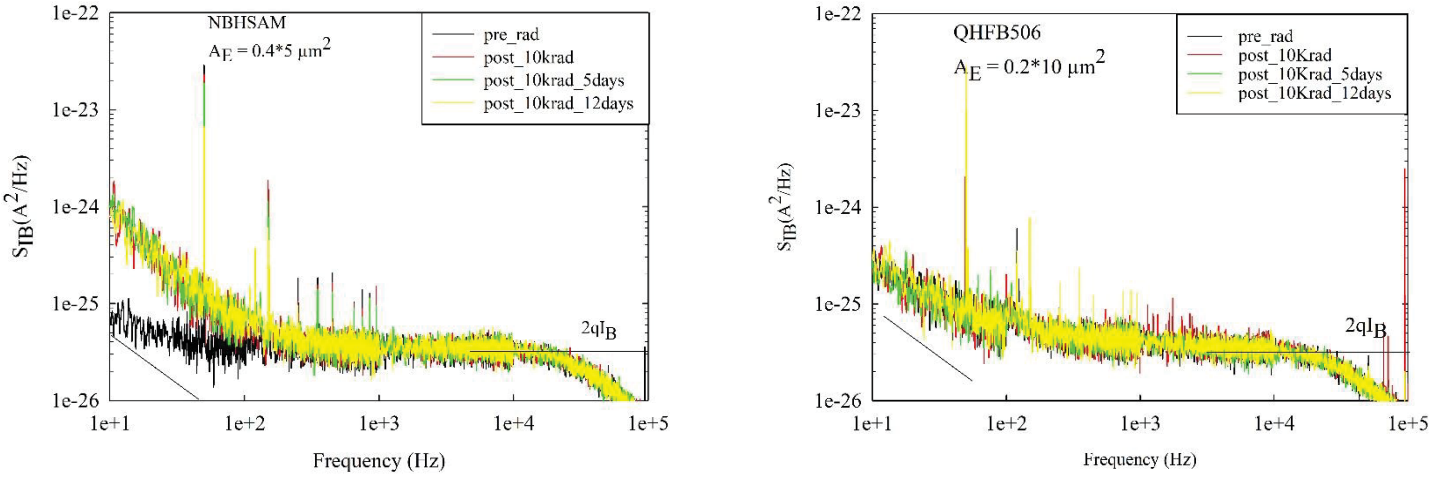

Figure 3.8. Impact of time relaxation on LFN measurements for both BiCMOS9MW and B55.

The second tested geometry, 0.27*5 μm^2 and 0.2*5 μm^2 of the BiCMOS9MW and the B55 respectively, presented similar tendencies for both DC and LFN measurements. Thus, we can state that the irradiation studies are not affected by the time interval and the measurements during the irradiation process.

3.5.2 Methodology of the irradiation process

To investigate the irradiation impact on HBTs, unbiased components are irradiated using the X-ray generator. A nominal voltage and current biases of 320 kV and 12.5 mA respectively are used. This study is performed at room temperature with a dose rate of 4.0433 rad/s until reaching a Total Ionizing Dose (TID) of 151 krad. A total of 10 irradiation steps are established that are presented in Table 3.3. This investigation is held on 3 dice with a total of 15 HBTs for each BiCMOS technology.

	Dose rate (rad/s)	Dose (krad)	TID (krad)
1st step	4.0433	6	6
2nd step	4.0433	5	11
3rd step	4.0433	5	16
4th step	4.0433	10	26
5th step	4.0433	10	36
6th step	4.0433	15	51
7th step	4.0433	20	71
8th step	4.0433	20	91
9th step	4.0433	30	121
10th step	4.0433	30	151

Table 3.3. X-ray irradiation steps for both technologies until reaching the total dose.

After each irradiation step, DC (Gummel plot) and LFN characterizations are carried out. LFN was measured at three I_B current biases: 50, 100 and 500 nA.

Once the TID reached a dose of 151 krad, a study of long-time and thermal annealing effects are done to investigate a possible healing effect. The long-time effect was examined 8 months after the last irradiation dose. The annealing effect was studied by isothermal annealing processes: two annealing temperature, 100 °C and 130 °C, were applied on HBTs.

3.5.3 DC characteristics for the irradiated HBTs

As examined in chapter 2, the DC characteristic corresponds to the Forward Gummel mode characterization. The impact of irradiations is studied in a bias voltage range of 0.3 to 0.7 V. The respected bias range represents a section of the low injection regime (0.3 to 0.4 V) and the diffusion regime of the HBTs (0.4 to 0.7 V).

3.5.3.1 Gummel-plot analysis

Graphs in this section represent the evolution of the forward Gummel mode characteristics for both BiCMOS9MW and B55 technologies after each TID step. Each technology revealed a distinct behavior.

The first behavior presented in Figure 3.9 for BiCMOS9MW, is identified by a significant increase in the I_B level and a decrease in the current gain h_{FE} which tends to saturate after a certain dose. These two factors are visible in both low-level injection regime and diffusion regime. A slight impact on I_C is observed after irradiation exposure, along with the high increase of I_B.

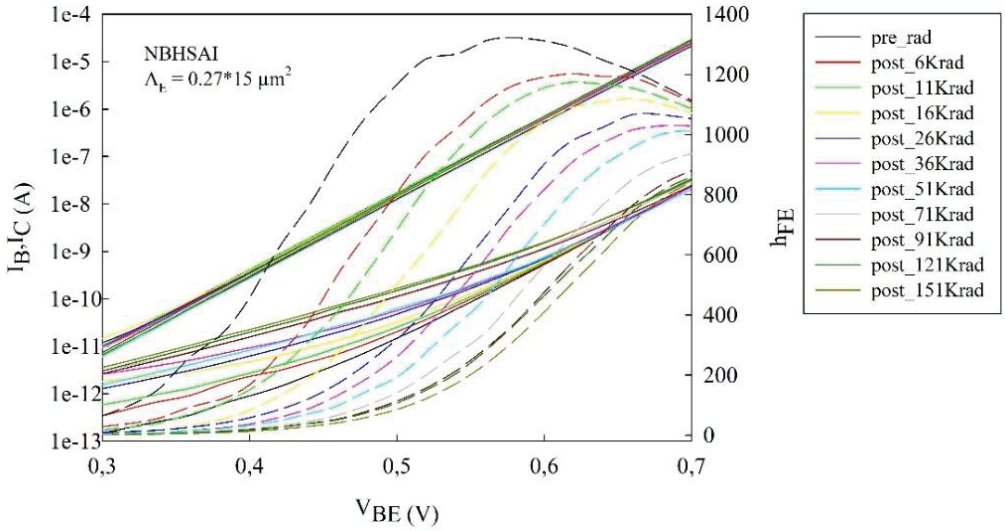

Figure 3.9. Gummel characteristics for a BiCMOS9MW HBT (A_E = 4.05 µm²). Solid lines: I_B and I_C currents – Dash lines: DC current gain h_{FE}.

Figure 3.10Figure 3.10 illustrates the second behavior which depicts the B55 HBT's response. Contrarily to the described one for BiCMOS9MW a near negligible impact occurred on I_B after a TID of 151 krad.

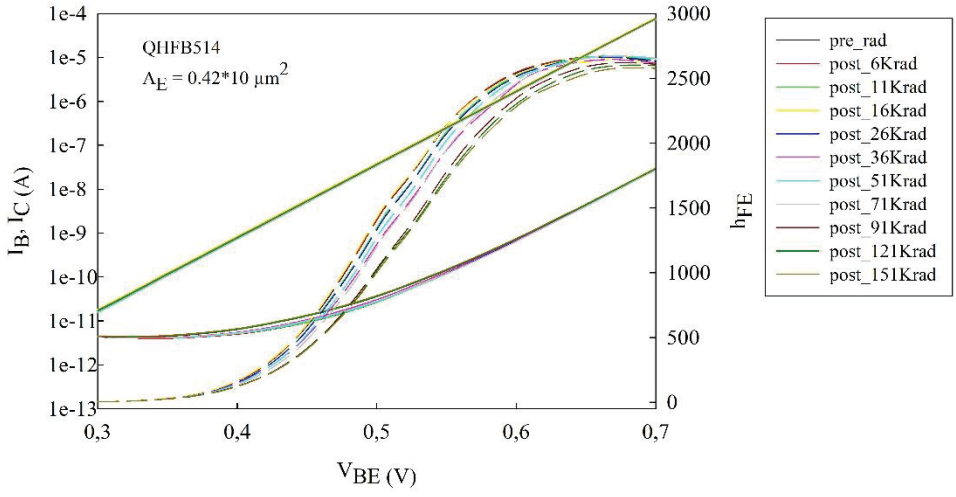

Figure 3.10.Gummel characteristics for a B55 HBT (A_E = 4.2µm²). Solid lines: I_B and I_C currents – Dash lines: DC current gain h_{FE}.

Next, a quantitative approach of the X-ray irradiation effects is presented for each BiCMOS technology.

I-V characteristics indicated the base current as the primary factor affected by the irradiation process. Therefore, I_B current is considered as the main investigated parameter in this study. A Figure-Of-Merit is studied, the normalized excess forward current, to evaluate the effect of TID on the input current of the HBTs. It is presented in equation 3.1.

$$\frac{\Delta I_B}{I_B} = \frac{I_{B_{post\,rad}} - I_{B_{pre\,rad}}}{I_{B_{pre\,rad}}} \qquad 3.1$$

This FOM is examined for V_{BE} values that consider the highest I_B degradation. These values correspond to 0.42 V and 0.46 V for BiCMOS9MW and B55 respectively. The FOM are plotted in Figure 3.11 as a function of TID.

Figure 3.11 presents two graphs corresponding to two A_E of each technology. As can be seen, a unique irradiation response is found for each BiCMOS technology. The degradation impact on BiCMOS9MW HBTs exceeded by no less than one decade the irradiated B55 ones. Independently to the emitter geometries, an increase of the normalized excess base current was systematically observed in response to TID. Both technologies presented a near linear increase in $\frac{\Delta I_B}{I_B}$ as a response to the TID. This tendency was already observed in earlier studies [72][118].

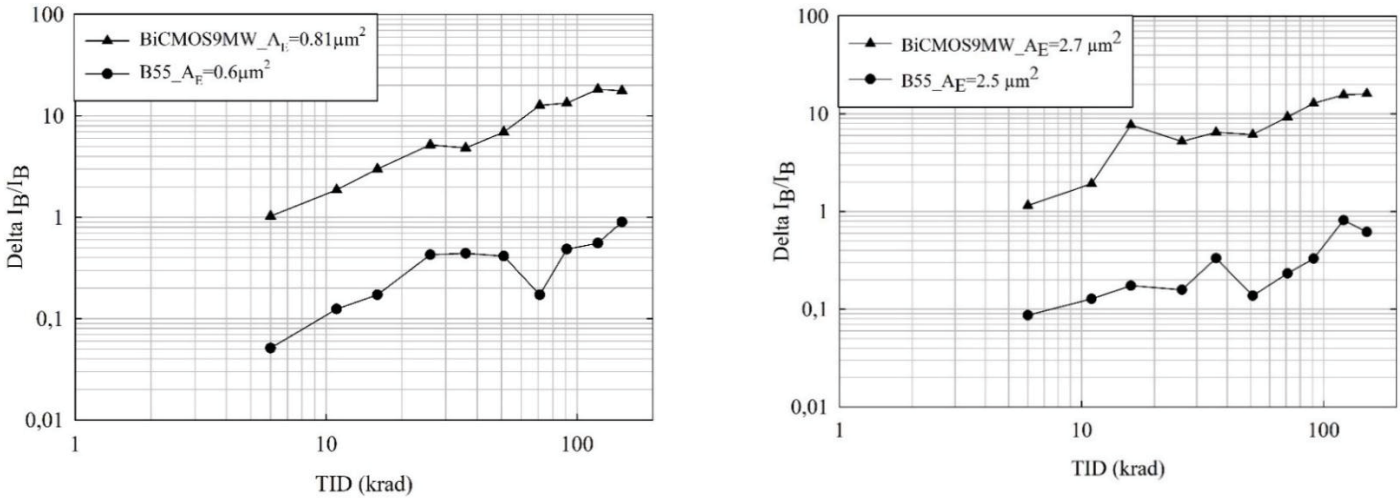

Figure 3.11. Excess forward mode variation, respectively for BiCMOS9MW and B55, as a function of TID

To investigate a possible surface dependency, Figure 3.12 illustrates the excess current base response to TID for all of the tested geometries. A comparable degradation response is found for the BiCMOS9MW HBTs while a negligible dispersion is observed for the B55 HBTs caused by the low degradation impact (less than 10%). Therefore, the irradiation response can result in an independency to A_E for both technologies.

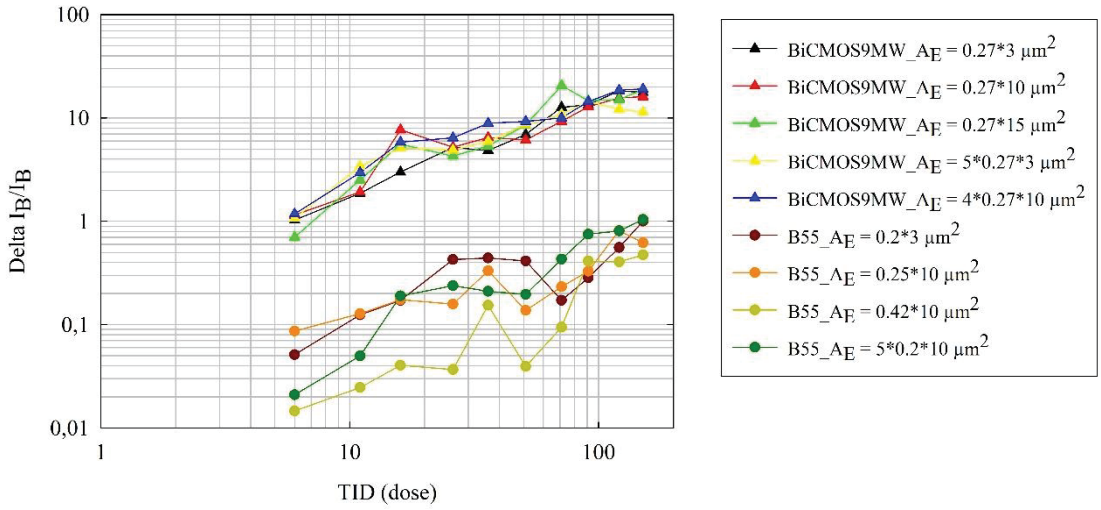

Figure 3.12. Dependency of the excess current base to A_E

3.5.3.2 Discussion on the degradation impact

The increase of I_B level was attributed to induced Generation-Recombination centers in the emitter-base region [118][119] especially at:

- The E-B spacer oxide. The induced trapped charge in the E-B spacer oxide is responsible for the increase of the base current.
- The Collector side, some authors identified the STI oxide as a localization area of the induced traps [72]. Nevertheless, the created traps in the STI oxide are not examined since I_C did not presented a significant irradiation response. Generally speaking, to investigate the impact on STI oxide, the inverse Gummel mode must be studied.

The suspected areas of the induced trap centers are illustrated in Figure 3.13.

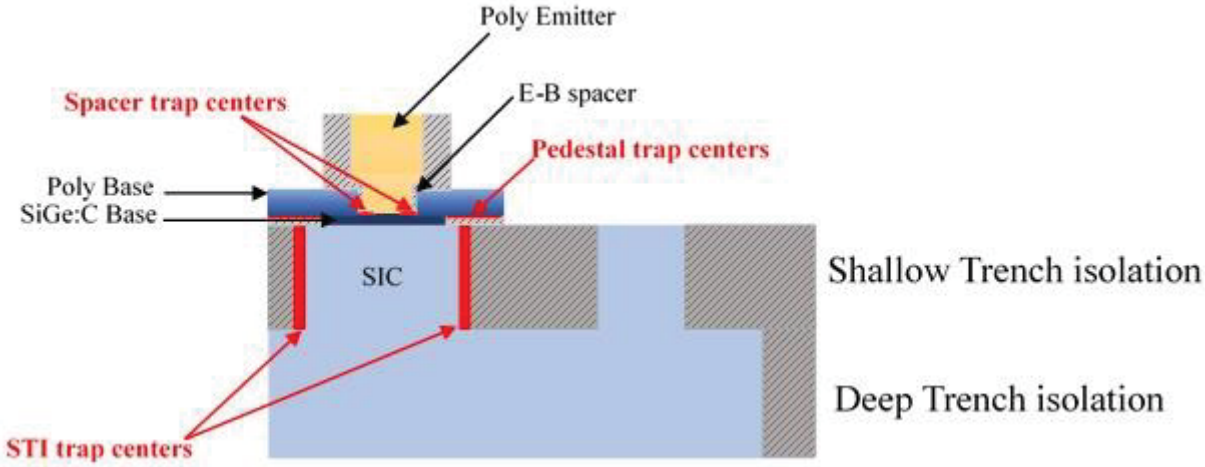

Figure 3.13. Possible induced oxide trap centers in the schematic cross section of an HBT.

By considering the induced excess current as a peripheral current component, the base current is presented as followed [120]:

$$I_{B\ post\_rad} = I_{B\ \text{pre\_rad}} + P_E J_{bl} \exp\left(\frac{qV_{BE}}{n_{B_{G-R}} KT}\right) \quad 3.2$$

where $n_{B_{G-R}}$ represents the Generation-Recombination ideality factor respectively, P_E the emitter perimeter and J_{bl} the leakage current at the emitter-edge length expressed in pA/µm.

Eq. 3.2 is composed of two terms: the first one corresponds to the initial HBT state before irradiation. While the second term constitutes the induced current (recombination current) proportional to emitter perimeter P_E and presenting an ideality factor $n_{B_{G-R}}$ of 2.

One of the geometrical shrinking dimensions consequences in the newest BiCMOS generation is the reduction of the oxide thicknesses in the HBTs. Thus, compared to BiCMOS9MW, B55 technology presents reduced oxide thicknesses especially at the spacer oxide located at the E-B periphery. Thereby, we can suggest that by reducing the peripheral oxide, the created trap number in the emitter periphery decreases and so the impact of the second term of 3.2 is reduced. The reduction of the oxide layer can be considered as the key parameter to explain the higher robustness of the B55 technology. This behavior is consistent with previous studies on the irradiation impact in response to the gate oxide thickness of MOSFET devices [121].

3.5.4 Low-Frequency Noise measurements for stressed HBTs

In this paragraph, the evolution of LFN after X-ray exposure is reported by measuring the fluctuation of the input base current, S_{IB}, for the two BiCMOS technologies. Irradiation impact is investigated on both flicker noise (1/f noise) and G-R components. Before irradiation exposure, the predominance of ideal spectral (1/f noise followed by the shot noise $2qI_B$) recorded a percentage of 86 % for tested BiCMOS9MW transistors and 27 % for the B55 ones. A detailed study interpreting each of these noise components at their pristine state was established in chapter 2. The presence of G-R components is more conspicuous for the B55 technology compared to the BiCMOS9MW one [122] as already studied in section 2.7. Spectra affected by G-R components mainly presented two Lorentzian components [86][84].

After a brief spectral analysis, we will detail the impact of X-ray irradiation on 1/f noise and G-R components. This study is undertaken as a function of the Base current bias and the geometrical parameters.

3.5.4.1 S_{IB} response towards X-ray exposure

After X-ray exposure, multiple irradiation responses were recorded during LFN measurements. Different behaviors were observed and can be sorted into 4 main categories:

The first category illustrated in Figure 3.14.a presented the overcome of G-R components over the 1/f noise directly after the first irradiation exposure, after a dose of 6 kad. An increase in the G-R magnitude is detected along with the TID increase, this evolution tends to saturate after a certain dose. The current spectral density S_{IB} at 10 Hz mainly increased by 2 decades through the irradiation procedure. This behavior was marked mainly for BiCMOS9MW technology.

The second category recorded during this study is illustrated in Figure 3.14.b. This behavior presented a negligible degradation impact on the 1/f noise until a certain dose followed by the

predomination of the G-R components. In the presented sample, the 1/f noise is maintained at a stable level up to a dose of 91 krad. The induced G-R components present stable magnitude level and fc independently to the dose. This behavior was observed for B55 technology.

The third category, presented in Figure 3.14.c, depicted an increase of the 1/f noise level after each irradiation step until the overcome of the G-R components. The induced G-R components are observed after a dose of 26 krad for the illustrated sample. This behavior is found for both technologies, nevertheless, the increase of the 1/f noise for B55 technology is found to be less pronounced. The irradiations revealed an increase in the G-R magnitude along with the TID. This impact was more observed for the BiCMOS9MW.

Finally, the last behavior illustrated in Figure 3.14.d, presented an independency of the initial G-R components to the irradiation exposure until a certain dose. At a given dose, 91 krad for the presented sample, an increase of the Lorentzian plateau took place especially on the second G-R component. This behavior is marked for the B55 technology.

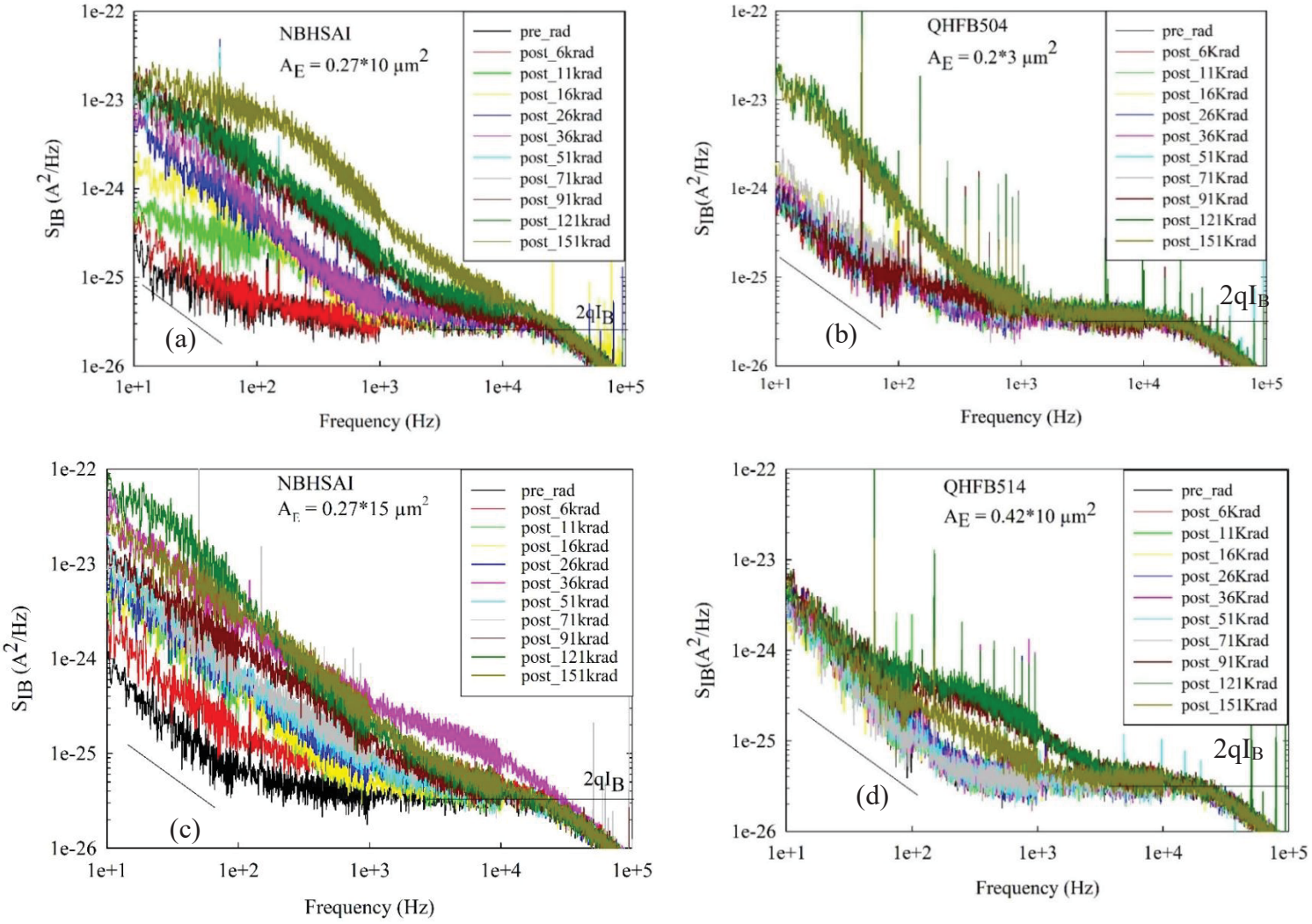

Figure 3.14. Various irradiation responses of S_{IB}, for I_B = 100 nA, after X-ray exposure.

Exceptional cases were revealed for a certain dose presenting a shifted spectrum with a higher noise level than the following spectra. This case can be found in Figure 3.14.c at a TID of 36 krad (the pink spectrum). Nonetheless, the observed phenomenon, for random cumulative doses, presented an insignificant percentage of the total tested HBTs. Therefore, it will not be considered.

3.5.4.2 Impact of TID on the 1/f noise

In this section, only HBTs presenting a pristine ideal spectrum were examined. Figure 3.15 presents the response of the 1/f noise level after irradiation exposure for both technologies. BiCMOS9MW HBTs maintained an ideal spectrum mainly until a dose of 26 krad, while the ideal spectrum of the B55 HBTs was conserved till a dose of 91 krad. Initial 1/f noise component was detected in 13 and 4 HBTs of BiCMOS9MW and B55 respectively.

Two tendencies were highlighted in Figure 3.15 for the selected A_E emitter surfaces in the range of 4 μm^2. Firstly, a significant increase in the 1/f noise level for the BiCMOS9MW, a factor of 1.5 decade is recorded, while secondly the B55 maintained a stable 1/f noise level through the irradiations. The illustrated data corresponds to an I_B value of 100 nA. The same tendencies are respected for the three tested input currents. Independently to the emitter geometry and the current biases, the 1/f noise irradiation response respected a similar behavior for all of the tested transistors of each technology.

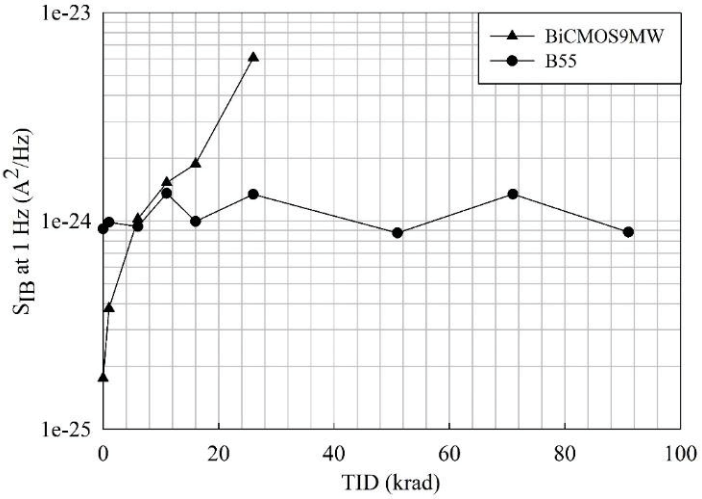

*Figure 3.15. Evolution of S_{IB} at 1 Hz in response to the TID, for BiCMOS9MW (A_E = 0.27*15 = 4.05 μm^2) and B55 (A_E = 0.42*10 = 4.2 μm^2).*

The predominance of the 1/f noise component, over the irradiation procedure, is encrypted in Table 3.3.

	Pre-rad	Post 6 krad	Post 16 krad	Post 26 krad	Post 36 krad	Post 51 krad	Post 71 krad	Post 91 krad	> 91 krad
BiCMOS9MW	86 %	45%	27%	9%	0%	0%	0%	0%	0%
B55	27%	27%	27%	27%	27%	27%	20%	20%	0%

Table 3.3. Ideal spectral tolerance of each BiCMOS technology as a function of TID.

3.5.4.2.1 1/f noise study as a function of I_B

Since, the 1/f noise extraction is possible for HBTs presenting G-R free spectra, ideal spectra are investigated up to the dose of 26 krad for BiCMOS9MW and 91 krad for B55. Figure 3.16 illustrates the irradiation response of S_{IB} at 1 Hz as a function of I_B for each technology. The selected devices in the graph below correspond to a 4.05 µm² and 4.2 µm² A_E HBT. A quadratic evolution of S_{IB} at 1 Hz in response to the I_B is recorded for both technologies before irradiation. This dependency is a typical behavior found for these components as presented in section 2.8.2.2.1. After X-ray exposure, the B55 technology maintained a quadratic evolution up to the dose of 91 krad, as can be seen in Figure 3.16. This behavior was already observed by A.K. Sutton in [72]. Nevertheless, BiCMOS9MW HBTs presented a significant shift in the slope value among with the increase of the total dose. The slope value varies within a range of 1 and 1.5 depending on the A_E, a value of 1.3 is found for the 4.05 µm² A_E HBTs presented in Figure 3.16.

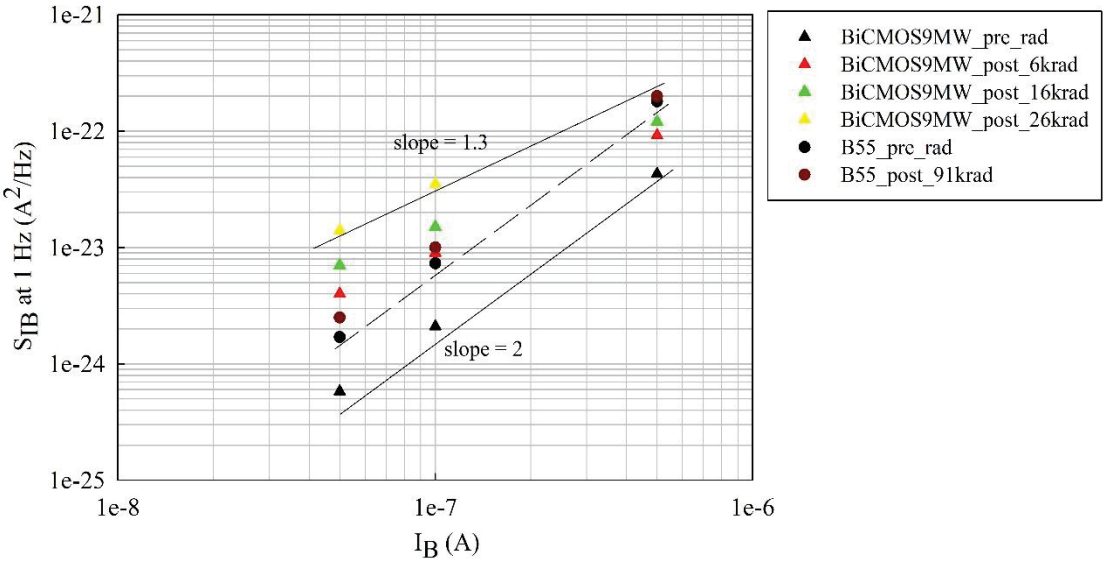

*Figure 3.16. Evolution of SIB at 1Hz as a function of I_B, both before and after irradiation, for BiCMOS9MW (A_E = 0.27*15 µm²) and B55 (A_E = 0.42*10 µm²).*

As previously demonstrated in [72] [103], the shift of the quadratic law after irradiation exposure is caused by the creation of additional noise component. A similar behavior was detected after the application of hot-carrier stress [46]. These components are associated with a non-ideal surface recombination base current induced by trap centers located at the emitter periphery close to the E-B depletion junction. After irradiation exposure, the 1/f SPICE model introduced in chapter 1 is presented as followed:

$$S_{IB\ post-rad}^{1/f} = K_F \frac{I_B^2}{f} + K_P \frac{I_B^{2/m}}{f} \qquad 3.3$$

The added term in relation 3.3 corresponds to a recombination base current therefore $I_B^{2/m}$ is roughly equal to I_B ($m \approx 2$).

Moreover, after irradiation exposure, a negligible impact on the 1/f noise level is observed for the B55 contrarily to the BiCMOS9MW.

3.5.4.2.2 1/f noise study as a function of A_E

To investigate the irradiation impact of 1/f noise in response to the geometrical parameters, K_F values are plotted as a function of A_E. Since K_F is a unit less value, it can be extracted only if the quadratic evolution law of I_B is respected. Analysis in the previous section demonstrated that only B55 technology respected an I_B^2 dependency after X-ray exposure while a shift from the I_B^2 law to an approximate I_B law is found for the BiCMOS9MW, see Figure 3.16. When I_B^2 is respected, K_F values are extracted from the SPICE model (as previously presented in section 1.4.1) and plotted as a function of A_E in Figure 3.17.

As can be seen in Figure 3.17, K_F is inversely proportional to A_E for the initial HBTs of both technologies as well as for the irradiated ones of the B55. This evolution is a classical behavior reported for unstressed Bipolar transistor indicating that the 1/f noise sources are homogenously distributed over the intrinsic E-B junction surface [123]. The presented data corresponds to an I_B value of 100 nA which corroborates with the other tested I_B.

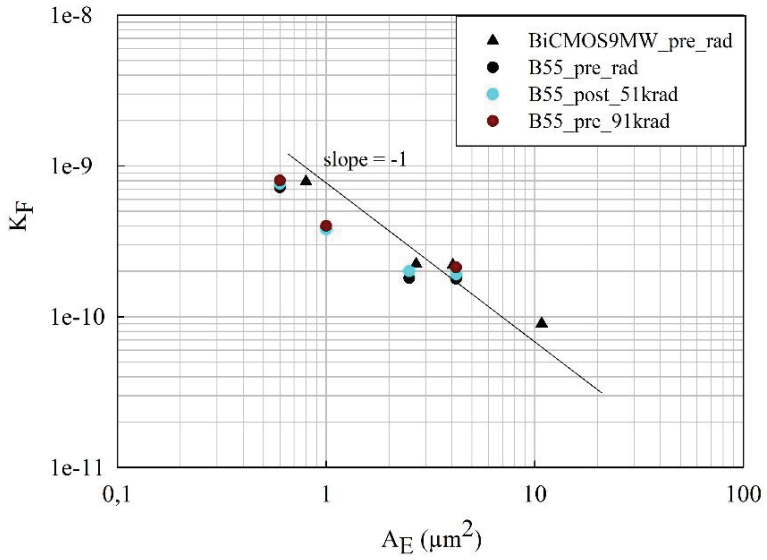

Figure 3.17. Figure of merit, K_F as a function of A_E for B55, both before and after irradiation, and for BiCMOS9MW before irradiation.

Regarding the irradiated BiCMOS9MW HBTs which disrespect the I_B^2 law, the evolution of the 1/f noise level at 1 Hz is plotted as a function of A_E in Figure 3.18 for an I_B of 100 nA. A shift in the A_E dependency from a slope value of -1 for pristine devices to a slope value in the range of 0.5 after a dose of 16 krad is observed. Hence, the predominant 1/f noise sources are no longer homogenously distributed at the E-B junction surface. The degradation impact is found to be more important for bigger A_E HBTs. The same behavior was respected for the three tested input currents. The non-respect of the usual laws concerning the evolution of the 1/f noise with the base current and the emitter area does not go in the direction of an aerial localization of the noise sources. However, a peripheral localization can be suggested.

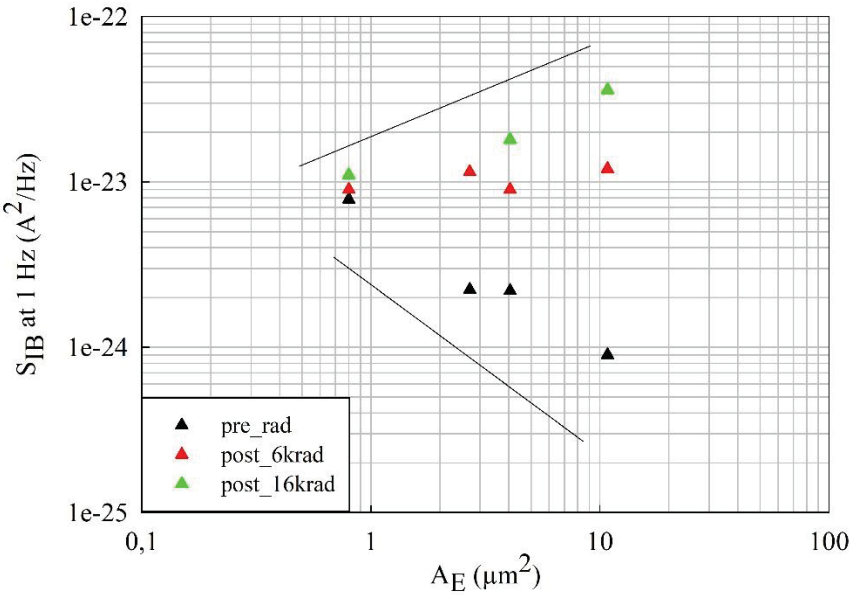

Figure 3.18. Impact on 1/f noise level at 1 Hz as a function of A_E for BiCMOS9MW technology, after irradiation exposure.

3.5.4.2.3 1/f noise study as a function of P_E

To narrow the suspected area of the HBT and to highlight its sensitive section, the emitter perimeter effect must be studied. However, this investigation is constrained by the limited P_E range due to the manufacturing boundaries in the HBTs geometries. Therefore, the extraction of a clear P_E dependency can be challenging in some cases. To discriminate between an aerial and peripheral localization of the 1/f noise sources, we used a model introducing a SCR recombination current induced by irradiation.

This model follows the Van der Ziel approach used to express the SCR recombination current using the Hooge formalism [124]. It reflects the empirical model of 3.3. The model is expressed in 3.4, for the irradiated spectral density of the base current [72] [125].

$$S_{IB\,post-rad}^{1/f} = \frac{K_B}{A_E} I_B^2 \frac{1}{f} + C I_B N_T \frac{P_E}{A_E} \frac{\alpha_H}{f} \qquad 3.4$$

- C is a none depending bias or geometry constant
- N_T is the trap density at the E-B junction surface
- α_H is the Hooge parameter depending on the carrier's mobility directly related to lattice scattering.

The first term of this model is associated to the classical empirical model presenting an I_B^2 and a $1/A_E$ dependency and supported by several physical models as presented in chapter 1 which corresponds to pristine HBTs. The second term, induced after the irradiation exposure, presents I_B and P_E/A_E ratio dependencies.

Figure 3.19Figure 3.19 represents the evolution of $S_{IB}*A_E$ during the irradiation procedure, for the B55 technology, as a function of P_E.

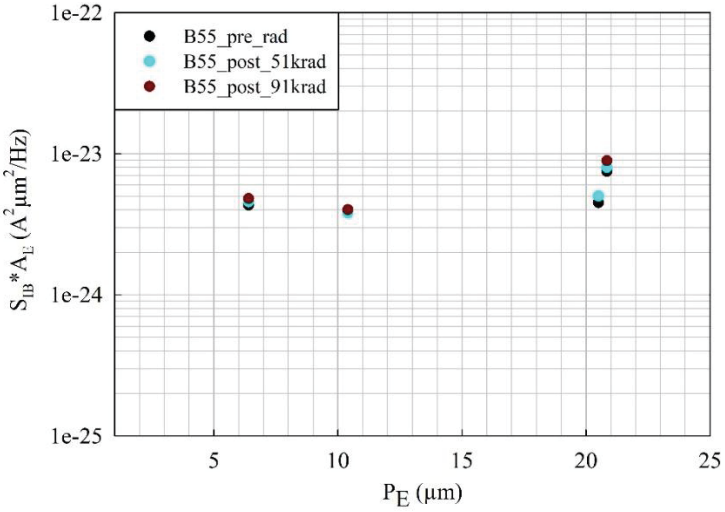

Figure 3.19. Irradiation impact on K_F as a function of P_E/A_E ratio for the B55 technology

An independency to the emitter perimeter is observed for devices before irradiation, this behavior was already observed in chapter 2. This tendency is also respected by the irradiated HBTs up to the dose of 91 krad. Since a $1/A_E$ dependency was earlier found associated with a P_E independency, we can conclude that the 1/f noise sources are located at the intrinsic E-B junction surface.

Concerning the BiCMOS9MW, S_{IB} at 1Hz*A_E evolution is plotted as a function of P_E at 0 krad, 6 krad and 16 krad, as can be seen in Figure 3.20Figure 3.20. Pristine components presented an independency to the P_E parameter which is considered a typical behavior for these devices. Nevertheless, after the irradiation exposure, a modification in the P_E tendency is found. A near linear increase of S_{IB} at 1 Hz *A_E is observed as a function of the P_E parameter. Hence, a P_E dependency can be concluded after irradiation exposure.

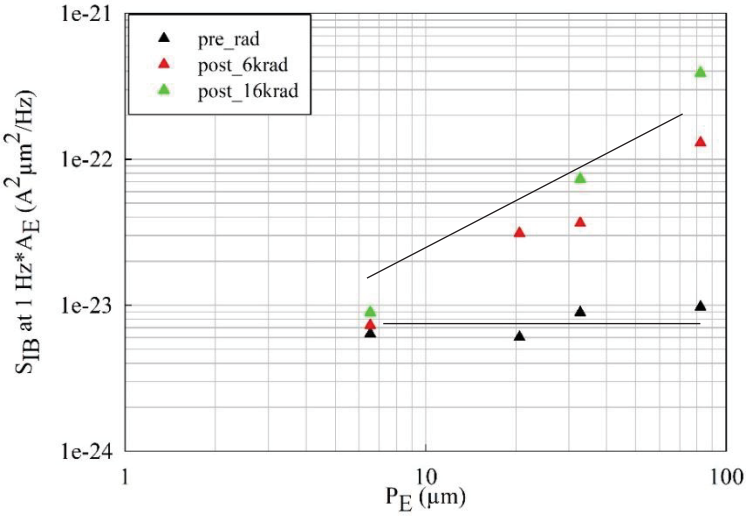

*Figure 3.20. Irradiation impact on the product S_{IB} at 1 Hz * A_E as a function of P_E for the BiCMOS9MW technology.*

After irradiation exposure, the induced noise component in the relation 3.4 is pronounced on the BiCMOS9MW devices concluding in the predomination of the SPR recombination current component fluctuations at the emitter perimeter. Thereby, the induced 1/f noise sources for BiCMOS9MW are located at the intrinsic E-B periphery. On the other hand, 1/f noise results of the B55 clearly demonstrated that the initial 1/f noise sources are not impacted after irradiation. Thereby, these noise sources are still described as an aerial effect.

3.5.4.3 Impact of TID on G-R component

In this section, Lorentzian parameters (cut-off frequency and plateau magnitude), of each G-R component, are investigated in response to the TID effects. Cut-off frequency f_{ci} analysis allows to identify the different trapping levels while the magnitude analysis allows to detect any potential modification of trap density after irradiation exposure. The extraction of these parameters was presented in detail in section 2.8.3.1. The empirical G-R SPICE model, for the irradiated HBT, is presented in 3.5 as followed:

$$S_{I_{B_{post\_rad}}}^{G-R} = S_{I_{B_{pre\_rad}}}^{G-R} + \sum_{i=1}^{N} \frac{A_i'}{1+\left(\frac{f}{f'_{ci}}\right)^2} \qquad 3.5$$

The first term is related to the presence of G-R components before irradiation, referred to as initial or pre_rad G-R devices. The second term is related to the induced or post_rad G-R components after irradiation exposure presenting a plateau magnitude A_i' and cut-off frequency f_{ci}'. As for the initial state, two G-R components were mainly found.

In this study, we will investigate the irradiation response of both components as a function of I_B and the emitter geometries. A comparison between initial and induced G-R components is established.

Initial G-R components are found in 2 and 11 HBTs for BiCMOS9MW and B55. Table 3.5 present the statistic of the induced G-R components.

	Pre-rad	Post 6 krad	Post 16 krad	Post 26 krad	Post 36 krad	Post 51 krad	Post 71 krad	Post 91 krad	> 91 krad
BiCMOS9MW	14 %	55%	73%	91%	100%	100%	100%	100%	100%
B55	73%	73%	73%	73%	73%	73%	80%	80%	100%

Table 3.5. Presence of G-R components of each BiCMOS technology as a function of TID.

3.5.4.3.1 Cut-off frequency study

3.5.4.3.1.1 Cut-off frequency evolution of initial G-R as a function of TID

The evolution of cut-off frequency in response to the irradiation dose will be depicted in this paragraph along with an investigation of I_B and A_E dependency.

Figure 3.21 represents the second cut-off frequency f_{c2}' of the G-R component in response to TID effect for three input current biases. The examined sample is a 0.27*15 μm^2 A_E HBT from the BiCMOS9MW technology. The irradiation exposure presented a negligible impact on f_{c2}' by

maintaining a stable f_{c2} in the range of 150 Hz. An independency to currents biases is concluded by presenting comparable dispersed fc values for the three I_B. Concerning the first G-R component, the cut-off frequencies respected a similar behavior to the one described in Figure 3.21 with cut-off-frequency values in the range of 20 Hz. The depicted behavior, of both cut-off frequencies, was respected by B55 HBT of a similar A_E HBT.

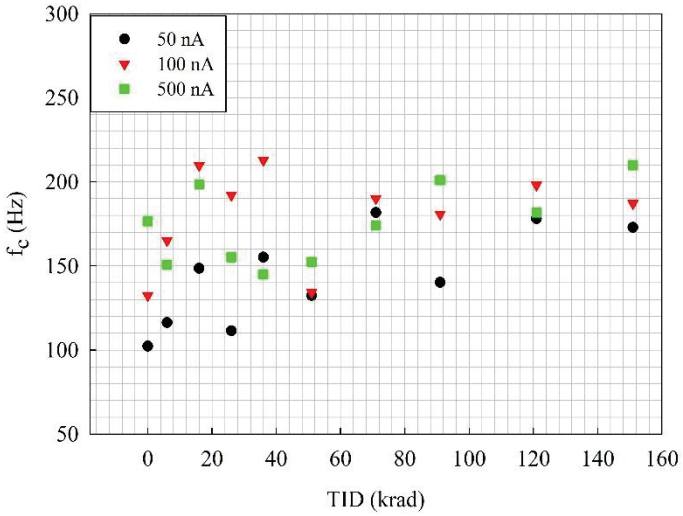

Figure 3.21. Cut-off frequency f_{c2} of the second G-R component versus TID from a 4.05 µm² A_E HBT of the BiCMOS9MW technology

Moreover, this tendency was studied in response to several emitter geometries. Figure 3.22 illustrates the first Lorentzian cut-off frequency f_{c1} evolution as a function of TID for several A_E HBTs of the B55. A negligible dependency to A_E can be concluded from the presented study. The same tendency was observed for the second cut-off frequency of the B55.

Moreover, a similar independency to A_E was found for the BiCMOS9MW HBTs presenting initial G-R components.

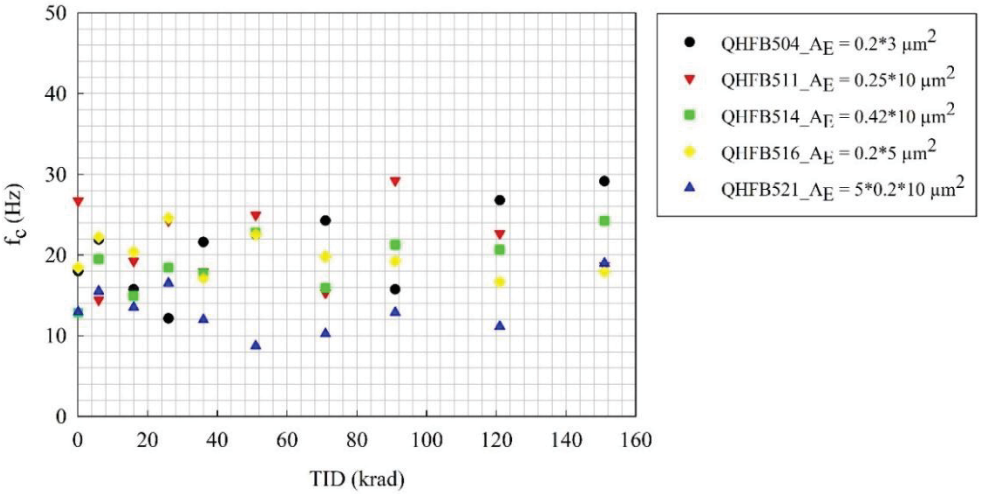

Figure 3.22. Evolution in function of TID of the first cut-off frequency f_{c1} for several A_E HBTs of the B55 technology

3.5.4.3.1.2 Comparison of initial versus induced cut-off frequencies

As presented earlier, the irradiation exposure of initial G-R spectra HBTs maintained two G-R components preserving a similar f_{ci} during the entire irradiation process. Nevertheless, in this section a comparison will take place between initial and induced G-R components after a certain dose exposure. This study is illustrated in Figure 3.23 for two A_E devices around 4 μm^2 of each technology.

As presented in Figure 3.23, the selected devices revealed a coherent behavior in the two studied cases. The induced f_{ci} are found at similar values comparing to the initial ones. This behavior was repeatedly observed, independently to the A_E, on all of the selected dice.

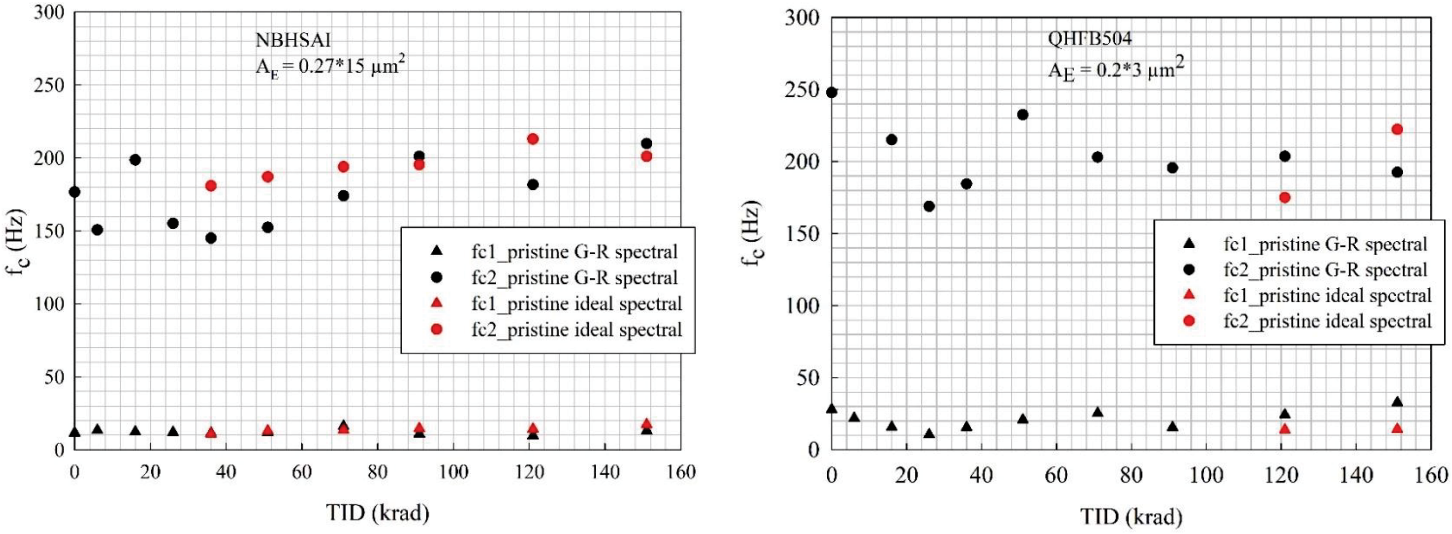

Figure 3.23. fci comparison of pristine G-R versus induced G-R components, for both technologies and two emitter areas.

Thereby, it is suggested that the irradiation exposures of HBTs are responsible for activating the existing defaults in the component detecting initial G-R spectra. Since both Lorentzian components respected a similar f_{ci} independently to the irradiation, the suggested model in eq. 3.5 can be presented as followed:

$$S_{IB\ post-rad}^{GR} = \frac{A_1{}'}{1+(\frac{f}{f_{c1}})^2} + \frac{A_2{}'}{1+(\frac{f}{f_{c2}})^2} \qquad 3.6$$

3.5.4.3.2 G-R plateau magnitude study

In this section, plateau magnitudes A_1' and A_2' presented in eq. 3.6 are investigated as a function of several parameters in response to TID.

3.5.4.3.2.1 Plateau magnitude evolution of initial G-R as a function of TID

In this section, the evolution of the two initial plateau magnitudes are examined as a function of TID for the three current biases. A distinguish dependency is highlighted by each technology

after irradiation exposure. Figure 3.24 illustrates the two plateau magnitudes of each G-R components for both technologies introduced as G-R_1 and G-R_2.

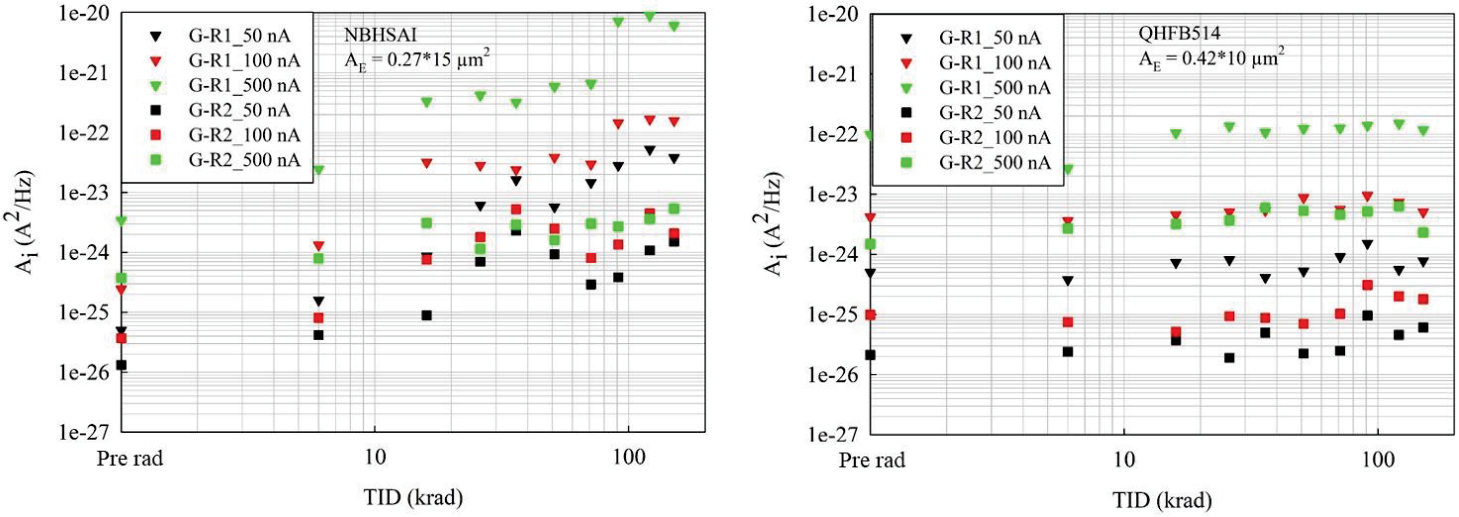

Figure 3.24. Analyses of the normalized G-R magnitudes as a function of TID for BiCMOS9MW (NBHSAI) and B55 (QHFB514)

The presented samples are the 4.05 and 4.2 µm^2 A_E HBTs for BiCMOS9MW and B55 respectively. A linear increase as a function of the cumulative dose of the magnitude levels is detected for the BiCMOS9MW while the B55 presented an independency to the irradiation dose by maintaining stable magnitude levels for the two G-R components. The increase of the plateau magnitudes for the BiCMOS9MW technology is probably related to the increased number of new trap centers after each irradiation step. Similar tendencies are also found for other HBT geometries.

3.5.4.3.2.2 Comparison of initial and induced plateau magnitudes

In this section, a comparison of the irradiation response between pristine and induced G-R magnitudes is established. This study is depicted in Figure 3.25 for both G-R components. The presented data corresponds to an I_B bias of 50 nA.

Over the irradiation exposure, the induced G-R components, after a dose of 36 krad and 121 krad, respected the same signature and tendency as the initial components. A significant increase of the plateau magnitudes for BiCMOS9MW while a stable level for B55 was detected. This phenomenon is reproduced by both I_B values of 100 nA and 500nA. By comparing the two G-R components of the BiCMOS9MW, induced magnitude is more pronounced for the first G-R component.

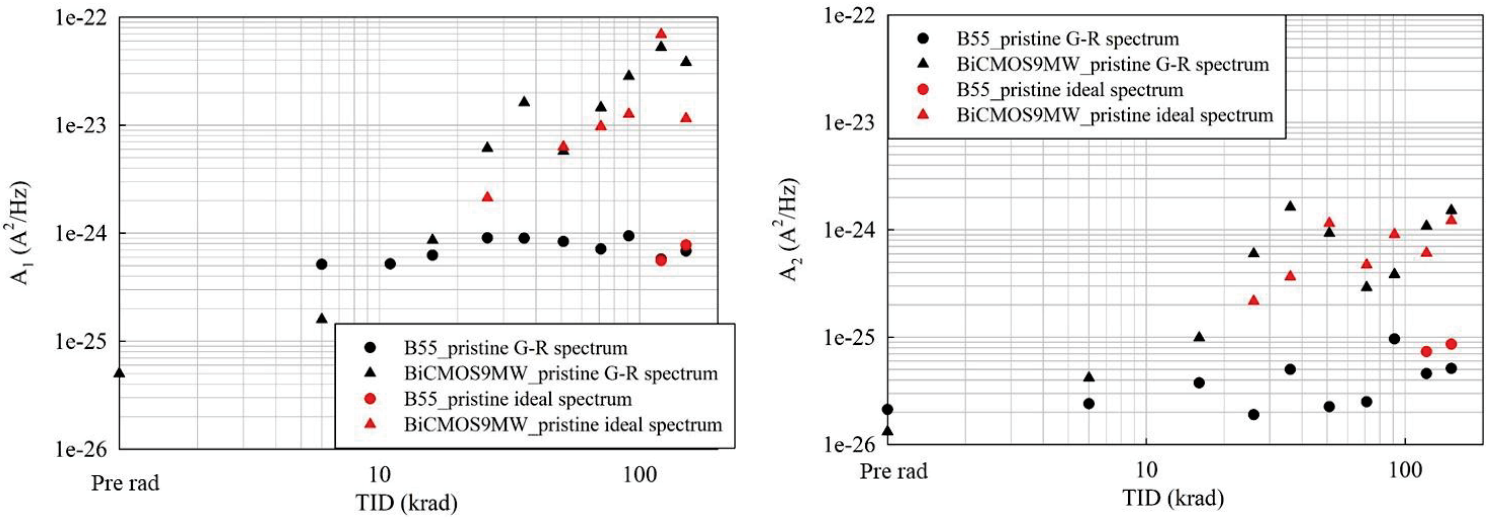

Figure 3.25. Study of the Lorentzian magnitudes of both BiCMOS9MW (4.05 µm²) and B55 (4.2 µm²) technologies.

3.5.4.3.2.3 Plateau magnitudes evolution in response to the geometrical parameters

The geometrical parameter study presented in this paragraph follows the same procedure established in chapter 2.

In Figure 3.26, the extraction of the two G-R magnitudes are plotted as a function of A_E for both technologies. Since the G-R components are less conspicuous in the BiCMOS9MW, only post irradiated G-R magnitudes will be plotted, after a dose of 71 krad and 151 krad, contrarily to the B55 where pristine and irradiated devices are analyzed. The plotted magnitudes correspond to an I_B value of 100 nA.

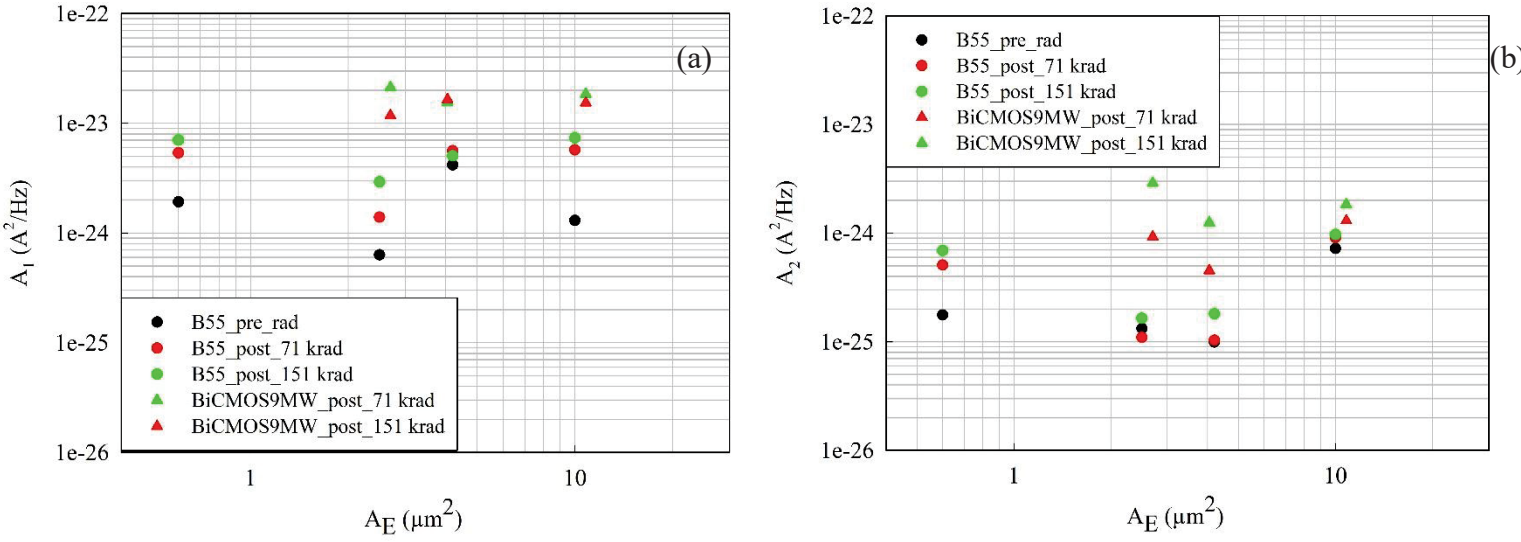

Figure 3.26. Irradiation response of both a) A1 and b) A2 as a function of the A_E for an I_B equals to 100 nA.

The presented results in Figure 3.26.a and Figure 3.26.b for the two G-R components of both technologies depicted an independency of plateau magnitude to the emitter area. The extraction of

the magnitudes in response to the A_E through the irradiation procedure respected the same behavior for the three tested input current.

Furthermore, G-R components are investigated as a function of the emitter periphery. The normalized G-R magnitudes are plotted in Figure 3.27 as a function of the P_E/A_E for an I_B of 100 nA.

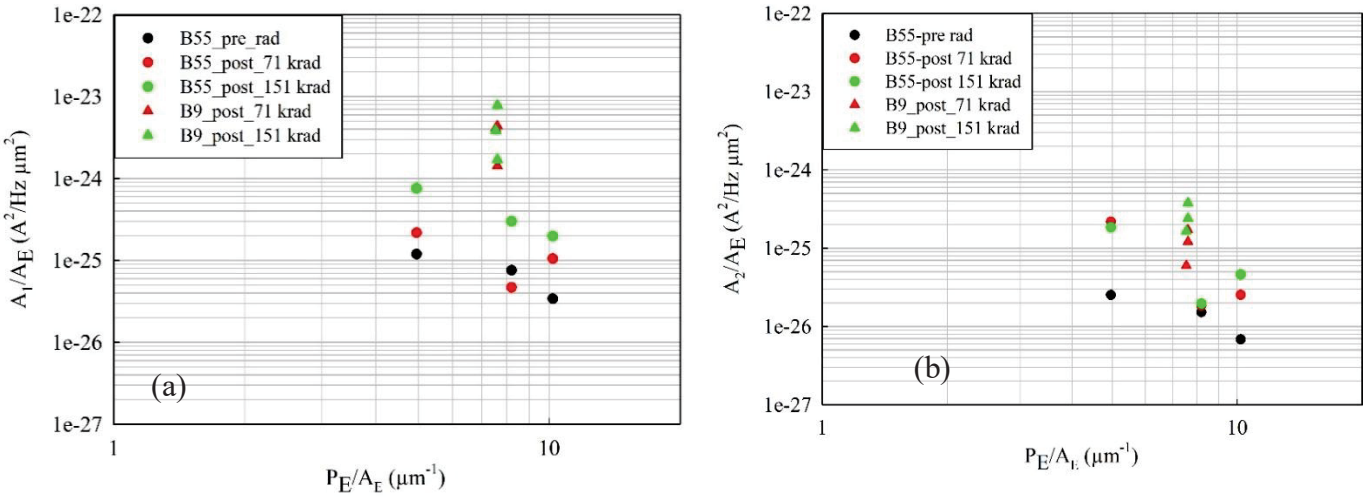

Figure 3.27. Irradiation response of both a) first and b) second G-R magnitude as a function of P_E, I_B equals to 100 nA.

A near linear decrease in the magnitude level in response to the P_E/A_E is found both before and after irradiation exposure for the two G-R components independently for the B55 technology. Nevertheless, the extraction of a BiCMOS9MW plateaus' dependency was not possible due to the limited P_E/A_E ratio. However, since they presented earlier an aerial independency, a peripheral one can be proposed. The magnitude levels of the BiCMOS9MW is found to be higher than the B55 one. This phenomenon can be due to the reduced oxide layer thickness moving toward the recent technology. Thereby, a lower G-R trap centers are found in the periphery of the B55 technology. The described behavior is respected by the three tested I_B values.

Concerning the established geometrical study, a dominance of a peripheral component over the aerial one can be concluded.

3.5.4.3.2.4 Plateau magnitudes evolution in response to I_B

Two geometries of each technology were selected to illustrate the irradiation response of the G-R magnitudes as a function of I_B. The emitter area HBTs are 2.7 μm^2/4.05 μm^2 and 2.5 μm^2/4.2 μm^2 for the BiCMOS9MW and the B55 technologies respectively. The A_E HBTs in the range of 2.5 μm^2 will be presented as HBT1 and the ones in the range of 4 μm^2 will be presented as HBT2. The first and the second G-R plateau magnitudes are presented in Figure 3.28.a and Figure 3.28.b respectively both before and after irradiation.

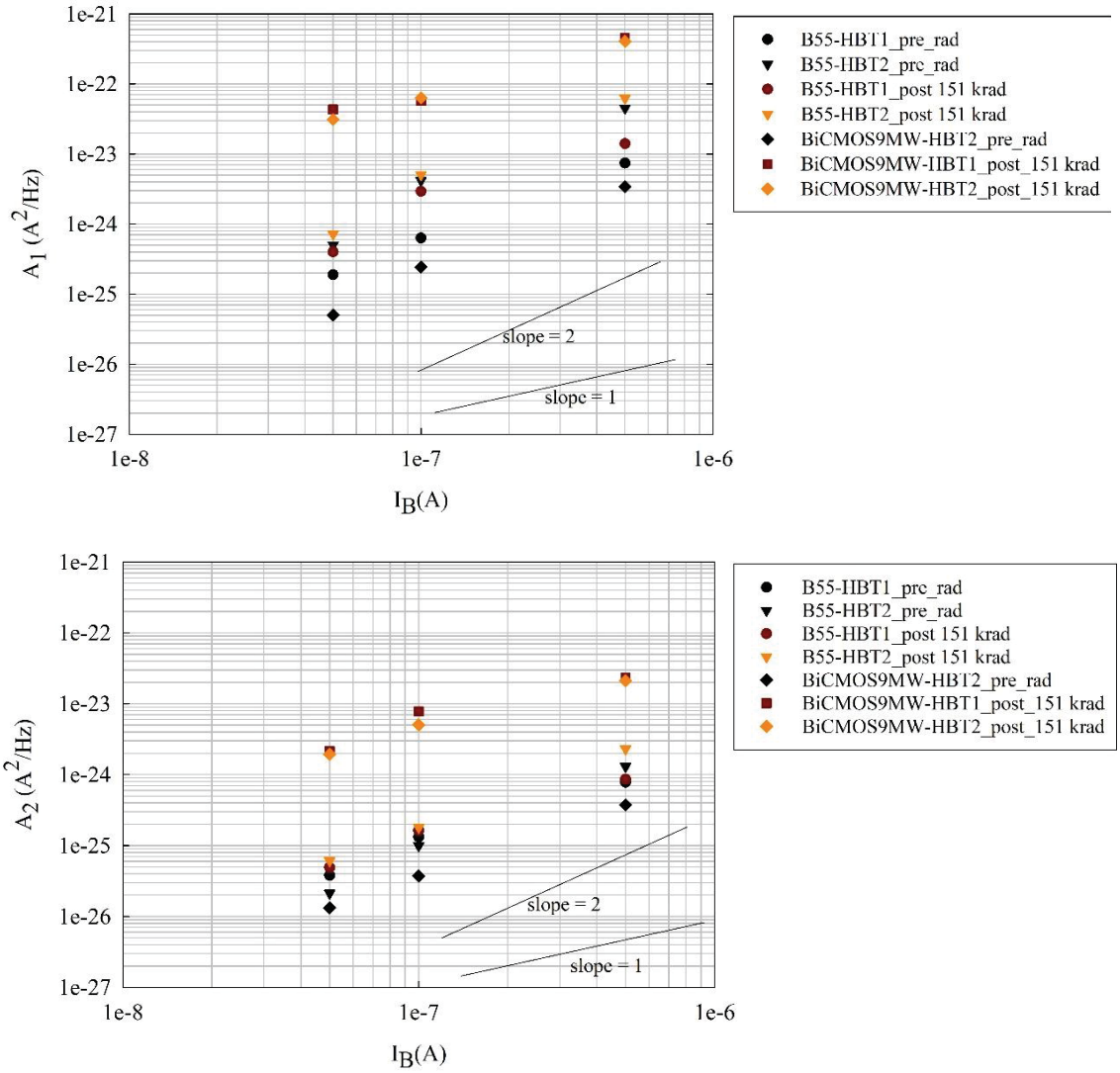

Figure 3.28. Irradiation response of both a) first and b) second normalized G-R magnitude as a function of I_B, HBT1 ≈ 2 µm² and HBT2 ≈ 4 µm².

More I_B values would be needed to establish a clear dependency for the magnitudes. Nevertheless, some tendencies can be extracted with the three tested currents.

The first G-R plateaus, illustrated in Figure 3.28.a, presented a quadratic base current evolution for pre-rad HBTs of both technologies. Lower amplitude is found for the A_E BiCMOS9MW HBT of 4.05 µm² compared to the same A_E B55 HBT. After the irradiation exposure, a distinct behavior was marked by an increase of the plateau magnitude in response to I_B. A near linear increase depicted the BiCMOS9MW while B55 HBTs respected the quadratic evolution observed at initial state. A higher magnitude is detected for the BiCMOS9MW due to a higher number of induced trap centers. An empirical model presenting the first Lorentzian magnitude can be written as followed:

$$A'_1 = K_{GR}\frac{1}{P_E}I_B^2 + K_{GR}{}'\frac{1}{P_E}I_B \qquad 3.7$$

However, the induced second term of the relation 3.7 corresponds only to the BiCMOS9MW technology.

The extraction of the second Lorentzian magnitude tendency was more challenging. Before irradiation, a slight modification in the magnitudes as a function of I_B are found shown in Figure 3.28.b. Before irradiation, the magnitude plateaus presented similar values for both technologies as can be seen in Figure 3.28.b. Hence, after a dose of 151 krad, a similar I_B dependency is observed with an additional increase in the magnitude of the BiCMOS9MW. The increase in the magnitude is less significant for the B55. Thereby, the second Lorentzian magnitude, of both technologies, can be represented as followed;

$$A'_2 = K_{GR}\frac{1}{P_E}I_B^{\alpha} + K_{GR}{}'\frac{1}{P_E}I_B \qquad 3.8$$

After X-ray exposure, both induced G-R components presented a $1/P_E$ dependency along with an I_B dependency. Hence, the G-R noise sources are suspected to take place in the E-B periphery (in the E-B spacer oxide or its interface with the intrinsic E-B junction). Unlike for the 1/f noise, there are few physical models available in the literature concerning G-R components in electronic devices and this is more specifically the case for bipolar transistors. The literature study that was done did not present a detailed investigation of the induced G-R component after irradiation. Nevertheless the proposed localization of G-R noise sources is consistent with the general trend concerning the time domain studies of RTS noise [63][81][82][80] (note that the published results are mainly related to hot-carriers degradation).

3.5.5 Annealing response after X-ray exposure

To test a possible healing effect of the induced traps, two annealing process are carried out: long time and thermal annealing effect. The selected samples for this study presented an ideal behavior before the irradiation exposure.

3.5.5.1 Time effect before annealing

The effect of time was studied, at room temperature, during 8 months after the last irradiation step with a dose of 151 krad. Through this period several DC and LFN characterization were held to investigate any possible relaxation effect.

A negligible healing effect was found on both forward Gummel plots and LFN analysis during the investigated time domain. The same tendency was respected by the two technologies. This confirms the obtained results during the study presented in paragraph 3.5.1.

3.5.5.2 Thermal annealing effect

This annealing process was accomplished in a total period of 950 hours, HBTs were placed in a furnace and held at a constant temperature for a specific time period. First, the devices were annealed at 100°C within 570 hours. Then the annealing temperature was increased up to 130 °C

for the rest of the experiment. An interpretation of DC (excess base current) and LFN measurements was accomplished at several annealing steps.

3.5.5.2.1 DC analysis

Figure 3.29Figure 3.29 illustrates the variation of the normalized excess base current $\frac{\Delta I_B}{I_B}$ in response to the TID and to the annealing time. The extraction of these values is done at a V_{BE} of 0.42 V and 0.46 V for BiCMOS9MW and B55 respectively presenting an A_E of 2.5 μm^2 and 1 μm^2. The data plotted at T0 represents the HBTs' performances after the investigation process held for 8 months. The first part of the annealing process, for a temperature of 100 °C, presented a significant decrease in the excess current of the BiCMOS9MW HBTs. This healing effect in bipolar transistors was already presented by previous studies. It is based on the thermal emission of trapped holes from the SiO_2 bandgap to the SiO_2 valence band [126]. The effectiveness of this healing process takes place from temperature above 100°C. In contrast, the B55 presented a negligible healing effect by preserving a stable excess base current during the first annealing process. To explain the dissimilarity in the healing response, one can suggested the influence of the reduced spacer oxide thickness of the B55 leading to a reduced number of induced trap centers or a different localization at the vicinity of the E-B spacer.

Nevertheless, positive oxide charges and interface traps annealing could be quite important for higher temperature [126][127]. Therefore, an increase in the annealing temperature up to 130 °C is accomplish during the second part of the annealing process. The results are plotted in Figure 3.29 for time values greater than 600 hours. As a result, an important healing effect is marked by both technologies. The excess base current of both technologies decreased by a total of one decade. A 90% of recovery is reached for the B55 HBT.

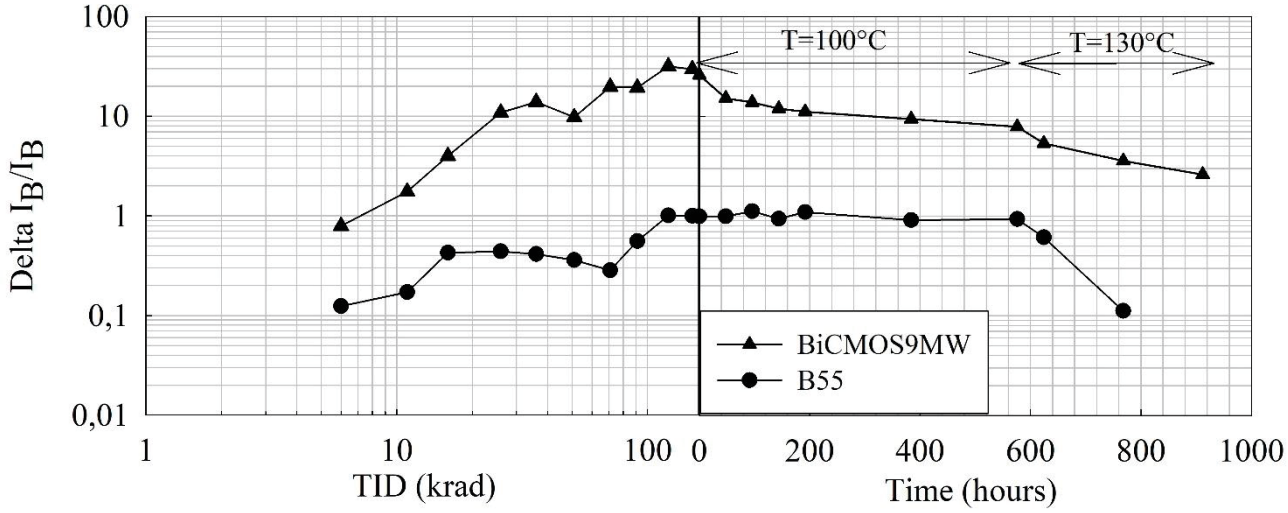

Figure 3.29. Variation of normalized excess base current for irradiated and isochronal annealed HBTs of both technologies.

3.5.5.2.2 LFN analysis

As previously presented, after X-ray exposure, the 1/f noise was overcame by G-R components. Hence, the healing process is expected to take place on the G-R components: amplitude and cut-off frequency.

The annealing impact on the LFN components is presented in Figure 3.30, the presented spectra correspond to a current bias of 100 nA.

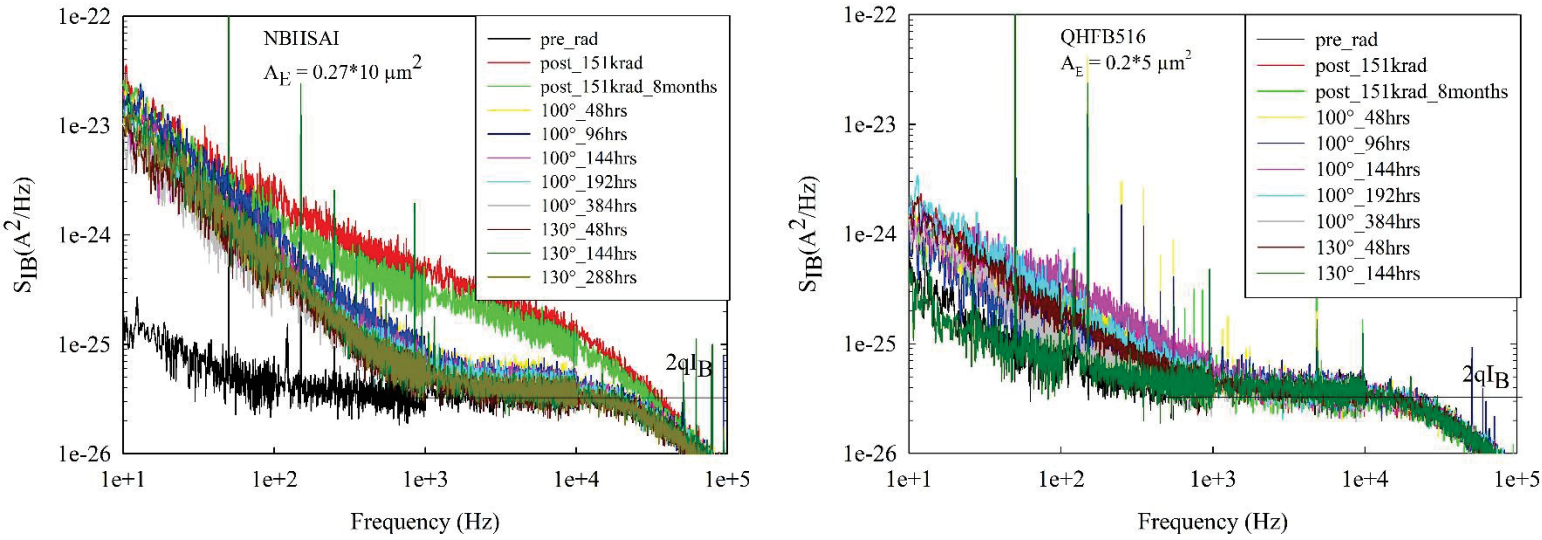

Figure 3.30. Evolution of LFN spectra as a function of multiple annealing process for BiCMOS9MW (NBHSAI) and B55 (QHFB516), for I_B value of 100 nA.

A healing effect was established for the G-R component with the higher cut-off frequency, in the range of 200 Hz, for the BiCMOS9MW HBT. This impact was recorded after the first annealing step at 100 °C. In contrast, the first G-R component presented a near negligible healing behavior through the annealing procedure.

Contrary to the precedent behavior, a near negligible healing impact was pronounced after the annealing process at 100°C for the B55 device. Nevertheless, during the annealing process, a substantial healing effect was recorded. The device spectra regained its ideal behavior, 1/f noise followed by the shot noise $2qI_B$, after an isochronal annealing of 130°C for 144 hours.

The observed annealing response at 100 nA is a representative example for the thermal annealing effect found on the both technologies.

The LFN analysis corroborates with the DC analysis, for both technologies, to indicate an important interface traps and oxide trap centers especially in the E-B oxides are created in the BiCMOS9MW. The different healing dynamic could be associated to the decrease in the E-B oxide thicknesses.

3.6 Irradiation impact on both High-Frequency and Low-Frequency domain

In the frame of TARANTO project, a collaboration with the IEMN laboratory at Lille University was done to accomplish the study of the impact of X-ray exposure on these devices.

The irradiation impact, in the high frequency domain, is reported on a 94 GHz large signal load-pull characterization. Both S-parameters and power performance were investigated as a response

to X-ray exposure. The HBTs were exposed to a cumulative dose of 50 krad. LF and HF characterizations were established before irradiation and after a dose of 20 krad and 50 krad for both technologies. This study was established on 4 dice of each BiCMOS technology.

3.6.1 HF analysis

Figure 3.31 represents the irradiation response of the S-parameters and the Power added efficiency (Pae) analysis. The irradiation response of the Re(S_{21}) is illustrated in Figure 3.31.a for a 2.5 µm^2 A_E HBT of the B55 technology. After a dose of 50 krad, a slight modification in the mod(S_{21}) level was recorded lower than 10 %. The described behavior was found for the others S-parameters of the presented HBT. Independently to the AE and the BiCMOS technology, a modification in the S-parameters lower than 10 % was extracted.

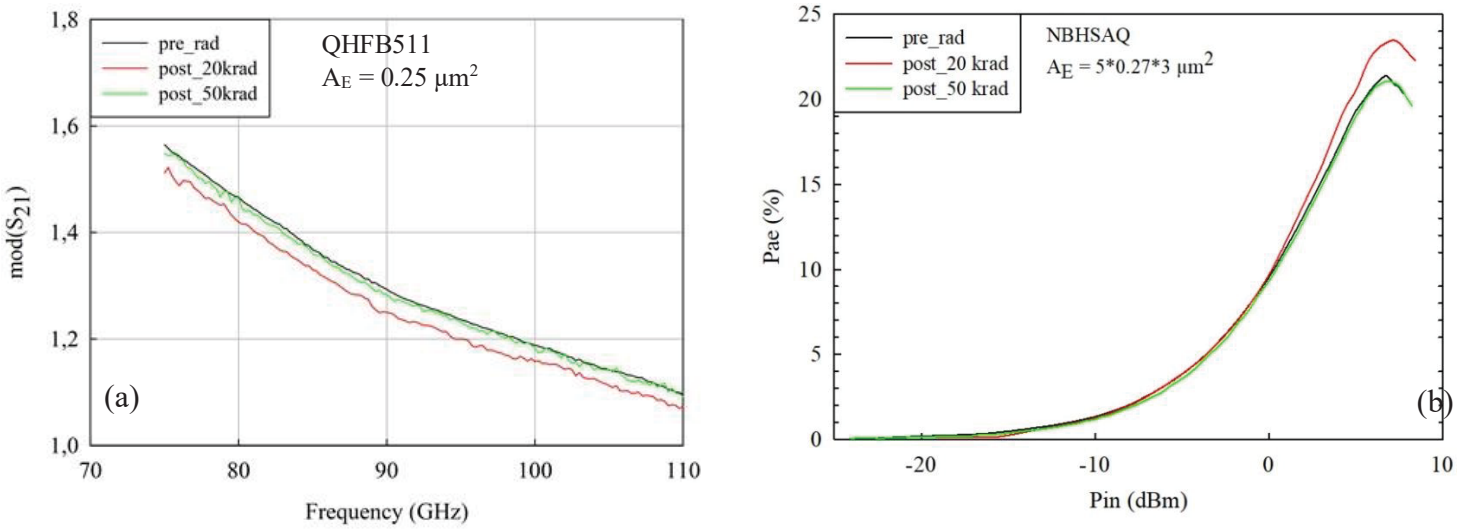

Figure 3.31. Irradiation impact deduced from a) S-parameters and b) load-pull characterization presented respectively for a B55 (2.5µm^2) and a BiCMOS9MW (4.05µm^2)

The load-pull characterization was initiated by a research of the bias and impedance that corresponds to the best Pae performance. This study is done at pristine state for two emitter area HBTs of each technology. After irradiation exposure, the investigation of the optimal impedance was carried out at the best polarization (extracted from the pristine HBTs). HBTs biases are maintained the same before and after irradiation so that a comparison can be possible. Irradiation response of Pae for a 4.05 µm^2 A_E HBT of the BiCMOS9MW is illustrated in Figure 3.31.b. A negligible impact was detected for the presented device. Similar behavior was concluded independently to the AE and BiCMOS technology presenting a variation in the range of 10 %. A more detailed representation of the irradiation impact on the load-pull characterization is summarized in Table 3.6.

	TID	V_{BE}	V_{CE}	I_B (µA)	I_C (mA)	Γ tuner	Gp (dB)	Pout at Pae max	Pae max (%)
	0 krad	0.89	1	4.6	2	0.71/95	5.5	0.5	19.7

BiCMOS9MW	20 krad	0.89	1	4.75	2	0.7/99	5.5	0.4	19.3
	50 krad	0.889	1	4.75	2	0.68/99	5.1	0.5	18.5
B55	0 krad	0.849	1	1	2	0.54/118	6.5	1.3	16.8
	20 krad	0.849	1	1.19	2	0.58/117	6.2	1.4	17.8
	50 krad	0.847	1	1.19	2	0.56/119	5.65	1.3	16.8

Table 3.6. Load pull characterization of irradiated HBTs of the BiCMOS9MW (NBHSAH) and B55 (QHFB505).

After irradiation exposure, both S-parameters and load-pull characterizations presented a low variation impact (< 10%). This slight variation is difficult to interpret as an irradiation impact, it could be related to the degradation of the HBTs contacts for instance. Thus, a negligible irradiation impact can be deduced after a dose of 50 krad for both technologies.

3.6.2 LF analysis at high current bias

After a dose of 50 krad, LFN measurements presented a coherent behavior to the one concluded in section 3.5.3. A higher degradation impact was extracted for the BiCMOS9MW. Nevertheless, this result contradicts with the obtained behavior in the HF analysis. Each characterization was accomplished in a well-defined bias range, I_B values are in the order of some µA and some nA for HF and LF measurements respectively.

To investigate the dissimilarity of the obtained results some additional tests were achieved in an adapted bias range. The LFN measurements are examined for higher I_B values in the range of 500 nA to 5µA. Figure 3.32 represents the irradiation response of the LFN after a dose of 30 krad for both technologies. The selected devices present a 0.27 μm^2 and a 2.5 μm^2 A_E for BiCMOS9MW and B55 respectively.

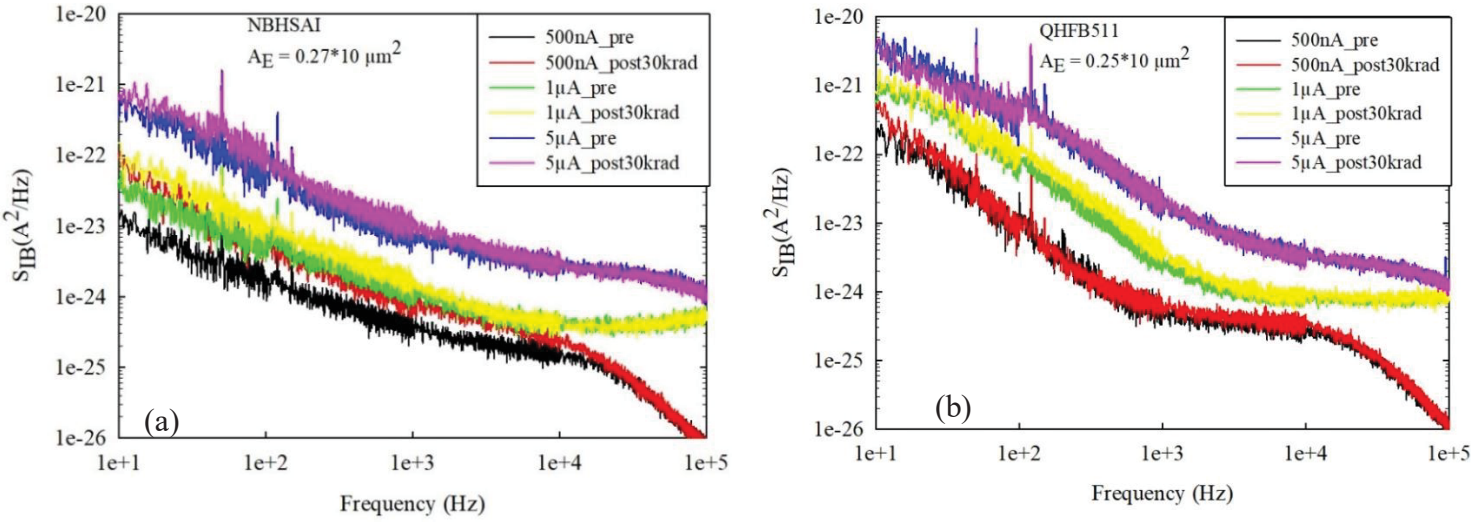

Figure 3.32. Irradiation impact on the LFN spectra of irradiated HBTs in a higher bias range for both technologies.

More significant results can be extracted for the BiCMOS9MW which presented a higher degradation impact to the irradiation compared to the B55. The degradation response is found to be inversely proportional to the current bias, as can be seen in Figure 3.32.a. In particular, a negligible impact is marked for the 5 μA current bias. The LFN results obtained in the same bias range correlate with the concluded ones found from the HF measurements.

3.7 Irradiation impact of the Cobalt60 source on HBTs

The use of a Cobalt60 source (Gamma-ray irradiation) aims to reproduce a more realistic radiative environment, resulting in a degradation behavior similar to the one confronted in real conditions. The Cobalt60 source results in the emission of higher energetic photon over, comparing to the emission of the X-ray, a larger period of time.

3.7.1 Methodology

Both BiCMOS technologies were exposed to Gamma-ray irradiation. Unbiased HBTs are irradiated at room temperature with a dose rate of 50 rad/h until reaching a cumulative dose of 330 krad. This TID is reached after 8 irradiation steps. Each dose step is established with either a dose of 30 krad or 60 krad, details are given in Table 3.7. A 30 krad step corresponds to an exposure time of 25 days and twice for 60 krad. This investigation is established on 4 dice with a total of 16 and 36 HBTs for BiCMOS9MW and B55 respectively.

	Dose rate (rad/h)	Dose (krad)	TID (krad)
1st step	50	30	30
2nd step	50	30	60
3rd step	50	30	90
4th step	50	30	120
5th step	50	30	150
6th step	50	60	210
7th step	50	60	270
8th step	50	60	330

Table 3.7. Gamma irradiation steps until reaching the total dose.

Each irradiation step is followed by a DC and a LFN characterization. A time interval of 5 to 10 days was required between each step. LFN studies are accomplished for three base current biases of 50 nA, 100 nA and 500 nA. The degradation impact of Gamma-ray irradiation is investigated by studying the excess current level, the 1/f noise and the G-R components.

After irradiation exposure, the effects of time and thermal annealing will be examined, for both technologies, 4 months after the final dose step of 330 krad. Two annealing temperature, 100 °C

and 130 °C, were investigated. Both DC and LFN are analyzed, after each annealing step, to report a possible healing effect.

The investigations after Gamma-ray exposure will present an identical methodology, for both DC and LFN measurements, comparing to the performed one with the X-ray source.

3.7.2 DC characteristics for the irradiated HBTs

3.7.2.1 Gummel plot analysis

The impact of Gamma-ray irradiation on the forward Gummel mode characteristics are represented in Figure 3.33 and Figure 3.34 for BiCMOS9MW and B55 technology respectively.

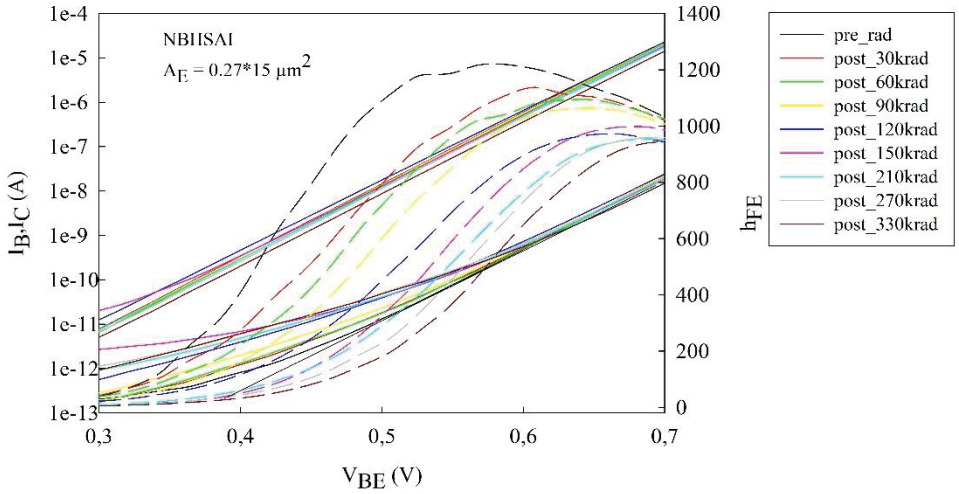

Figure 3.33. Gummel characteristics for a BiCMOS9MW HBT (A_E = 4.05 µm²). Solid lines: I_B and I_C currents – Dash lines: DC current gain h_{FE}.

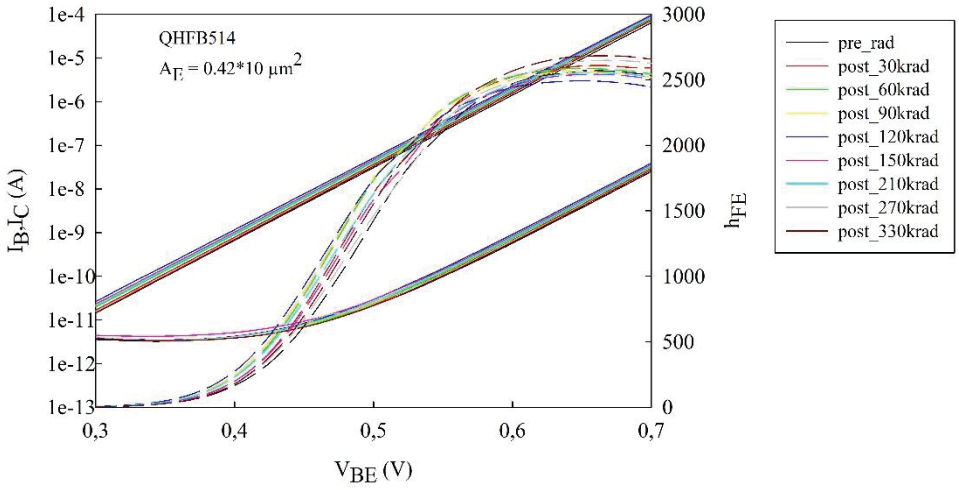

Figure 3.34. Gummel characteristics for a B55 HBT (A_E = 4.2 µm²). Solid lines: I_B and I_C currents – Dash lines: DC current gain h_{FE}.

As can be seen from the two figures, the irradiation effects are similar to the ones obtained after X-rays exposure. The B55 technology presented a higher tolerance to the Gamma-ray irradiations

while a significant increase of I_B associated to an important decrease of h_{FE} are found for the BiCMOS9MW. However, a distinct behavior from X-ray irradiations occurred on the collector current of both technologies. Moreover, regardless to the BiCMOS generation and the HBTs surfaces, a dispersion marked both I_B and I_C characteristics in the low-injection and the diffusion regime.

In the literature, the I_B parameter was presented as the key interest to detect the degradation response of the stressed components. Therefore, we will be mainly focusing on the normalized excess base current $\frac{\Delta I_B}{I_B}$ study which presented a higher degradation impact. It is studied in the low injection area and plotted in Figure 3.35.a. $\frac{\Delta I_B}{I_B}$ are extracted for the voltage biases that consider the highest degradation impact, 0.42 V and 0.46 V for BiCMOS9MW and B55 respectively.

Both technologies presented a linear increase in the $\frac{\Delta I_B}{I_B}$ level as a function of the cumulative dose that correlates with some previous results in the literature [118][120]. The same tendencies were induced after X-ray exposure. A higher degradation behavior was found for the BiCMOS9MW technology higher than the B55. The illustrated devices presented a higher degradation for the BiCMOS9MW by 1.5 decade.

Due to the observed impact on I_C, the normalized excess collector current was examined in Figure 3.35.b. The degradation response presented an independency to the device geometries. A linear decrease of $\frac{\Delta I_C}{I_C}$ level is found as a function of the TID. The excess I_C level is found slightly higher for the BiCMOS9MW. This tendency is respected by all the tested devices.

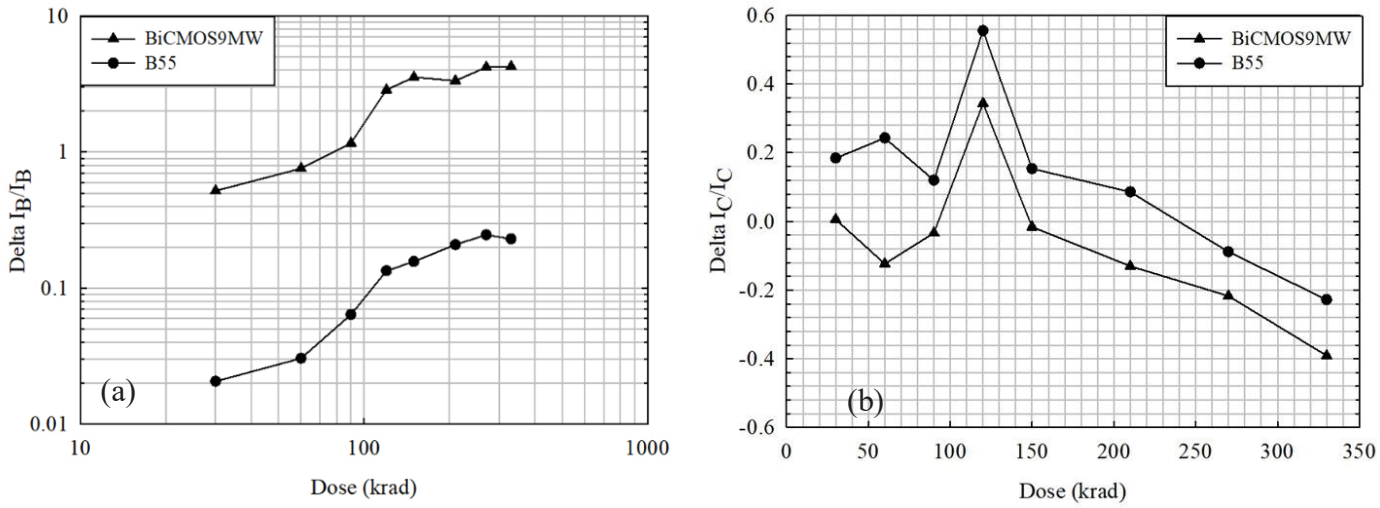

Figure 3.35. TID impact, for both BiCMOS9MW and B55, on the excess forward mode variation of I_B and I_C.

3.7.2.2 Discussion

The Gamma-ray exposure induced ionizing damages responsible for the degradation in the HBTs' performances. These damages, mainly found in the BiCMOS9MW, are responsible for the I_B increase in the low-injection regime and the dispersion found in the I_B and the I_C levels in the

diffusion regime. After irradiation exposure, the base current degradation can be approached using the same model presented earlier in eq. 3.2. The induced recombination current component after irradiation exposure is found to dominant in a bias range lower than 0.6 V as can be seen in Figure 3.33. Concerning the base current, the described tendencies are similar to the one induced by X-rays.

Therefore, we can suggest the same conclusion for the localization of the induced traps. They are located at the vicinity of the E-B spacer oxide with a strong tendency to highlight the emitter perimeter. In particular, to explain the robustness of the B55 technology, we suggested a probable influence of the reduction of the spacer oxide thickness. Complementary results and discussion will be presented in section 3.9 dedicated to the comparison of the effect of two irradiation sources.

Previous studies in the literature presented the degradation impact on both Forward and Inverse Gummel mode in order to discriminate the impact on spacer and STI oxides. These studies resulted in a higher tolerance for the E-B spacer oxide compared to the collector STI oxide towards the Gamma exposure due to the existence of nitride in the spacer oxide which improves the radiation hardness [72][128]. Even though only forward Gummel mode was examined, the observed degradation of I_C can be directly associated to the fact that Gamma-ray exposure can induce significant damages in the STI oxide.

3.7.3 Low-Frequency Noise measurements of stressed HBTs

The impact of Gamma-ray irradiation on 1/f noise and G-R components will be detailed in this paragraph after a brief spectral analysis. The irradiation impact on both LFN components will be investigated as a function of the base current bias and the geometrical parameters.

3.7.3.1 S_{IB} response after exposure to Gamma-ray

Before irradiation, the studied HBTs presented a dispersion effect related to multiple 1/f noise levels and G-R dependency that varies from a die to another [84]. These G-R components are mainly associated with an RTS noise [86] [106].

The degradation impact of Gamma-ray exposure recorded on LFN can be classified into four categories. The first category outlines in an increase of the 1/f noise level until a certain dose where the G-R components predominate, an increase in the G-R magnitude was found along with the increase of the total dose. This behavior, represented in Figure 3.36.a, is mainly found for BiCMOS9MW. The second category, represented in Figure 3.36.b, describes the irradiation response of some B55 devices presenting a slight increase in the 1/f noise level until the final TID of 330 krad. As for the third one, found in Figure 3.36.c, G-R components are witnessed directly after the first dose, the 1/f noise is masked by the induced G-R components. Finally, some HBTs exhibited a stable 1/f noise level during the irradiation exposure until the overcome of the G-R components. This behavior, presented in Figure 3.36.d, was observed only for B55 technology. The depicted behavior of LFN is similar to the one found after X-ray exposure.

Some random effects were recorded during the irradiation procedure. An example is presented also in Figure 3.36.d, where a sudden shifted spectrum is observed after a certain dose (blue

spectrum, at a dose of 120 krad). This behavior was not considered due to the non-reproducibility of this effect for the tested transistors.

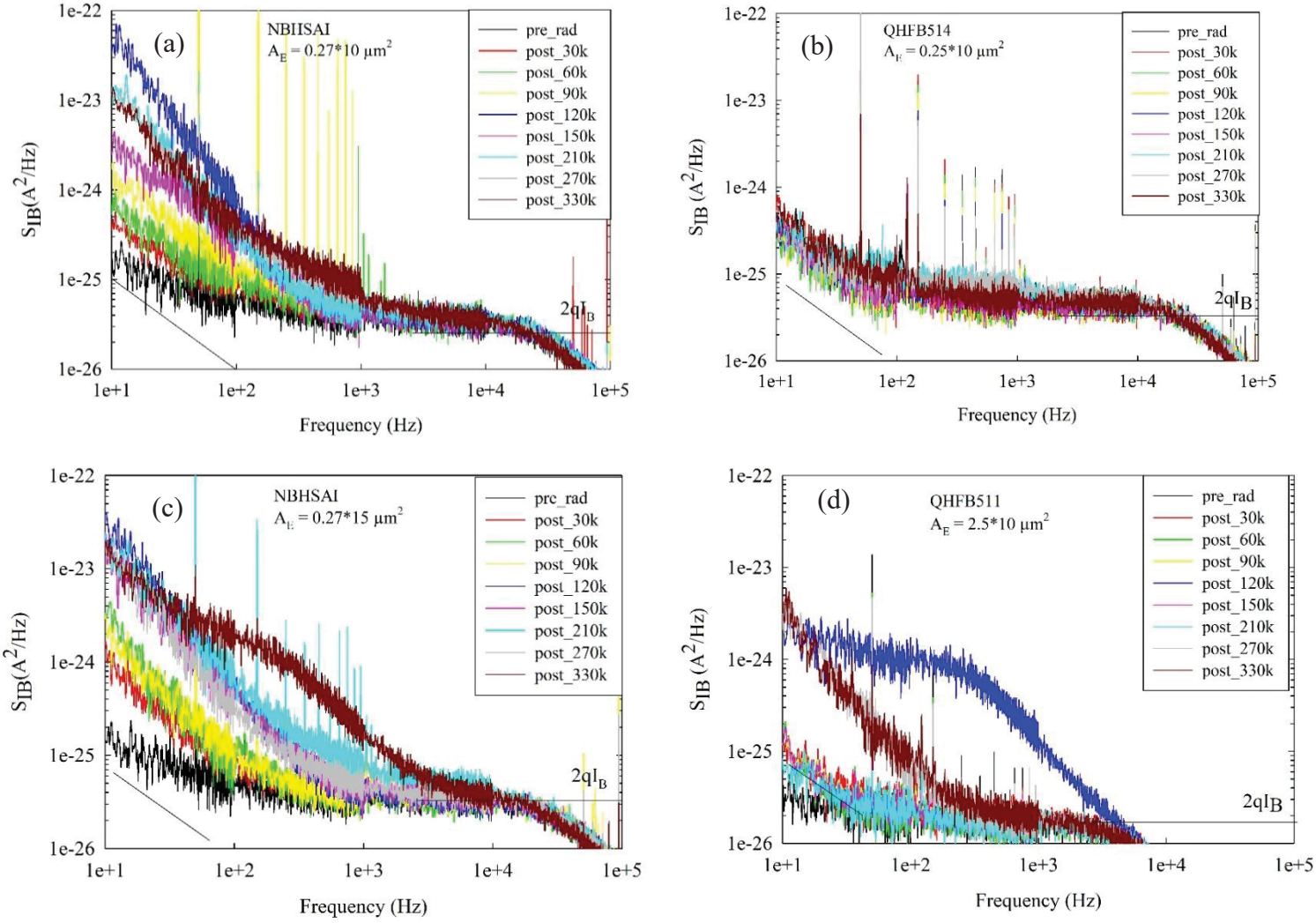

Figure 3.36. Irradiation response towards Gamma ray exposure for a, b, c) an I_B value of 100 nA and d) an I_B value of 50nA.

The study of a possible relaxation effect was accomplished during a period of 15 days after a 30 krad dose. It resulted in a negligible relaxation impact in response to the considered time interval for both DC and LFN measurements. This behavior is similar to the presented one in 3.5.4.

3.7.3.2 Impact of TID on the 1/f noise

LFN analysis resulted in a total of 10 and 13 HBTs presenting pristine ideal behaviors for the BiCMOS9MW and the B55 respectively. The irradiation response of the 1/f noise level was investigated as a function of the total ionizing Gamma dose. Irradiation response of the 1/f noise is presented in Figure 3.37 for both technologies on two dice (#1 and #2). Some HBTs preserved their ideal spectra (1/f noise followed by the shot noise $2qI_B$) up to a dose of 150 krad for the BICMOS9MW and a dose of 330 krad for some HBTs of the B55. Nevertheless, due to the limited number of HBTs at higher TID, the study will be held up to a dose of 90 krad and 150 krad for

BiCMOS9MW and B55 technologies respectively. Each technology presented a distinguished tendency. A significant increase in the 1/f noise level is marked for the BiCMOS9MW while a stable 1/f noise level is maintained for the B55. The induced noise level of BiCMOS9MW exceeded to initial one by one decade.

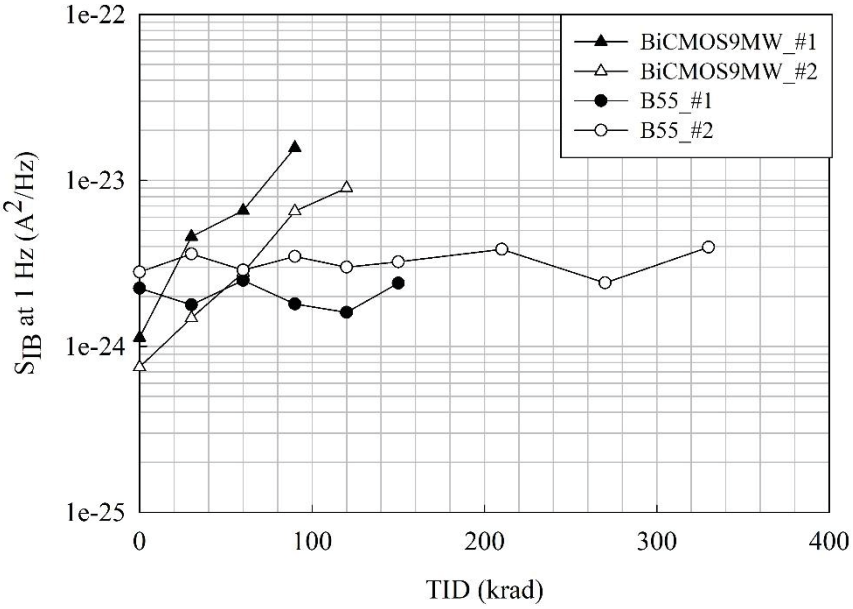

*Figure 3.37. Evolution of S_{IB} at 1 Hz in response to the TID, for BiCMOS9MW (A_E = 0.27*15 µm²) and B55 (A_E = 0.42*10 µm²).*

The presented results in Figure 3.37*Figure 3.37* corresponds to an I_B value of 100 nA for A_E HBTs in the range of 4 µm². Similar behaviors were extracted for the three tested input current. Moreover, the same tendencies were found for the two technologies independently to their geometries.

As usual, the occurrence of the G-R components is more conspicuous for the B55 technology reporting a non-ideal spectral percentage of 63 % while a percentage of 37% for the selected BiCMOS9MW HBTs. The predominance of the 1/f noise component is summarized in Table 3.8 over the irradiation procedure.

	Pre-rad	Post 30 krad	Post 60 krad	Post 90 krad	Post 120 krad	Post 150 krad	Post 210 krad	> 270 krad
BiCMOS9MW	63%	44%	32%	25%	13%	7%	0%	0%
B55	37%	37%	37%	37%	26%	26%	16%	12%

Table 3.8. Ideal spectral tolerance of each BiCMOS technology after Cobalt exposure.

3.7.3.2.1 Irradiation response of the 1/f noise level as a function of I_B

A study of the 1/f noise level as a function of I_B, for several TID, is presented in Figure 3.38. The presented results correspond to a 4.05 µm² and a 4.2 µm² A_E HBTs for BiCMOS9MW and B55 respectively. Pristine devices, of both technologies, presented a quadratic evolution of S_{IB} at

1 Hz as a function of I_B. As detailed in chapter 2, the I_B^2 law is a typical behavior found for these HBT devices. Free G-R spectra of the B55 technology respected an I_B^2 evolution after irradiation exposure until 150 krad as can be seen in the figure below. This dependency is already witnessed in the SiGe HBTs [72].

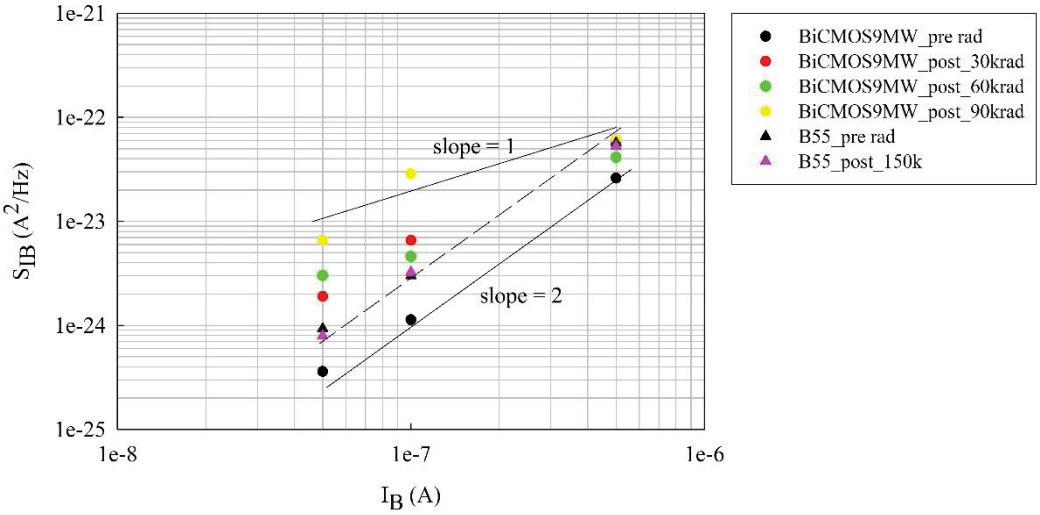

Figure 3.38. 1/f noise response to Gamma irradiation for both BiCMOS9MW (A_E = 4.05 µm²) and B55 (A_E = 4.2 µm²).

Nonetheless, a distinct behavior is found for the BiCMOS9MW HBTs disrespecting the I_B^2 law. Over the irradiation steps, a shift in the slope value is extracted to a value in the range of 1. This behavior was already observed after proton irradiation [72][125]. The drift to an I_B dependency reveals the overcome of an additional recombination current component [103] resulting in the increase of the 1/f noise level. The induced recombination component is less significant for higher current bias (higher tolerance for the 500 nA I_B value comparing to the 50 nA). Hence, the induced 1/f SPICE model after Gamma ray exposure is compatible with the one proposed previously in eq. 3.3.

A slight modification in the 1/f noise level as a response to the TID is found for different A_E HBTs. Hence, the described behavior is respected by both technologies in spite of the emitter geometry.

3.7.3.2.2 Irradiation response of the 1/f noise level as a function of A_E

In this section, a Figure-Of-Merit (FOM) can be used, K_F as a function of the A_E, to investigate the irradiation impact on the 1/f noise. K_F can be extracted from the 1/f SPICE model previously presented in relation 1.23. This parameter is expressed as a unit-less parameter if the I_B^2 law is respected.

Figure 3.39Figure 3.39 presents the FOM of both BiCMOS9MW and B55 pristine devices and irradiated B55 devices up to a dose of 150 krad. Before irradiation, K_F is found to be inversely proportional to A_E for both technologies. As already said, this typical behavior states that the 1/f noise sources are homogenously distributed at the intrinsic E-B interface. The irradiated HBTs of

the B55 presented a non-significant evolution in the K_F values while respecting the same tendency (a $1/A_E$ dependency), thereby we could conclude that no-induced 1/f noise sources are associated to the Gamma irradiations.

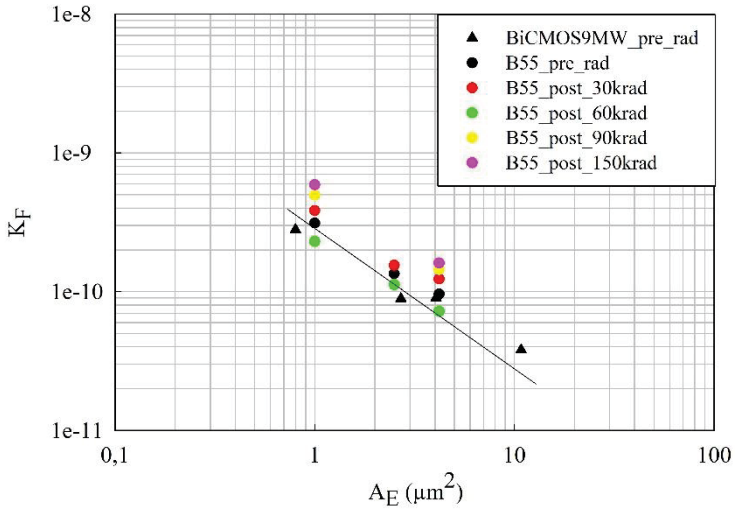

Figure 3.39. Figure of merit, K_F as a function of A_E for B55, both before and after irradiation exposure, and for BiCMOS9MW before irradiation.

Since the irradiated BiCMOS9MW HBTs have disrespected the I_B^2 law, S_{IB} at 1 Hz instead of K_F will be plotted as a function of the device's geometries. This study is plotted in Figure 3.40 for 3 irradiation stages: before irradiation, after 30 krad and 90 krad.

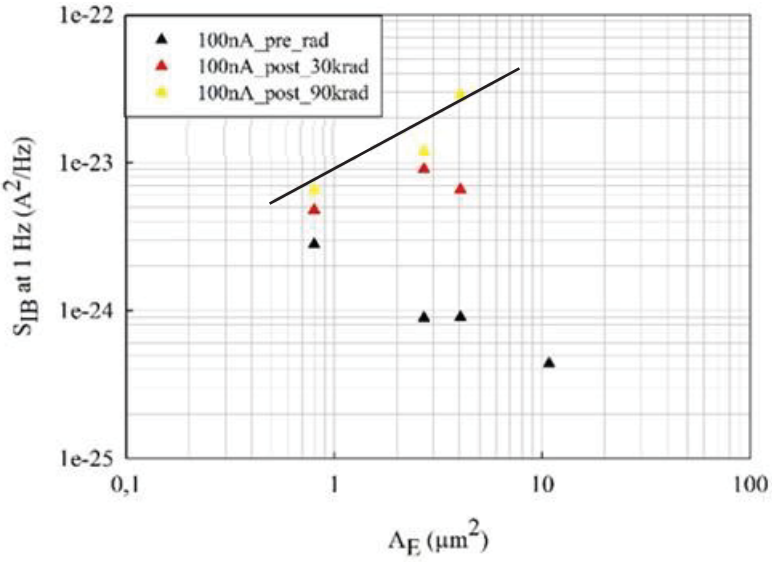

Figure 3.40. S_{IB} at 1 Hz irradiation response as a function of the A_E for the BiCMOS9MW technology.

A shift from the $1/A_E$ dependency to an $A_E^{0.8}$ was found after a dose of 90 Krad. Hence, the induced 1/f noise sources dominating the initial ones are not located at the intrinsic E-B surface, a peripheral effect can be suggested.

3.7.3.2.3 Irradiation response of the 1/f noise level as a function of P_E

For a better localization of the 1/f noise sources, an investigation as a function of the P_E is done. The extraction of a clear perimeter dependency is a challenging study limited by the restrain manufacturing geometries of the HBTs geometries and the maintained of the ideal spectra after irradiation exposure. Following 1/f noise model of relation 3.4 presented in paragraph 3.5.4.2.2, the irradiation response of $S_{IB}*A_E$ is investigated as a function of the P_E and is presented in Figure 3.41 for the B55 HBTs. for the B55 HBTs. An independence to the P_E can be extracted from both pristine and irradiated HBTs. Thereby, the E-B periphery is not the dominant localization of the 1/f noise sources confirming the predominance of the E-B area.

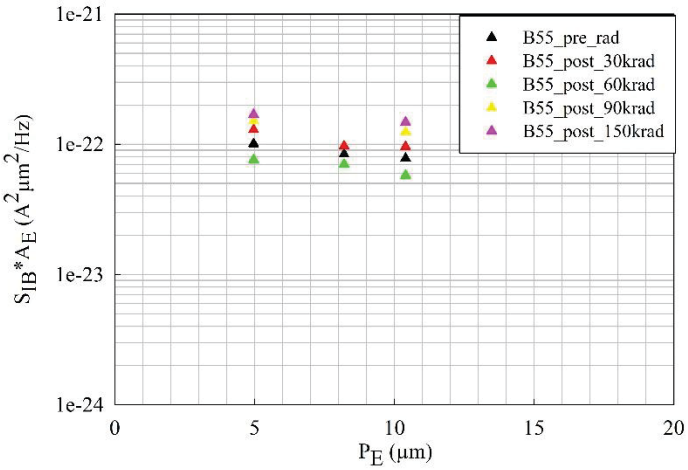

Figure 3.41. Irradiation impact of Gamma exposure on the K_F as a function of P_E/A_E for the B55 technology for I_B =500 nA.

As for the BiCMOS9MW technology, $S_{IB}*A_E$ at 1 Hz is studied as a function of the P_E parameter and represented in Figure 3.42.

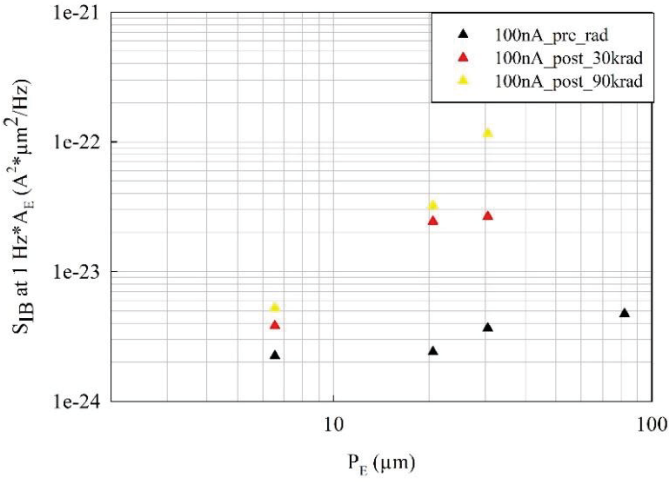

Figure 3.42. Irradiation impact of Gamma exposure on the $S_{IB}*A_E$ at 1Hz as a function of P_E for the BiCMOS9MW technology

The extraction of a clear tendency is more complicated; nonetheless, some tendencies can be proposed. The pristine devices have presented an independency to P_E, this tendency is considered to be the main behavior found for these devices as presented in chapter 2. After irradiation exposure, a P_E dependency occurs in agreement with the proposed Van der Ziel model in 3.4. As a reminder, this model consists of an empirical component with a dependence on I_B^2 and $1/A_E$ and a component associated to the fluctuation of a SCR recombination current, which dominates after irradiation exposure, with a dependence on I_B and P_E/A_E. Thus, the BiCMOS9MW induced 1/f noise sources after Gamma irradiation are found to be located at the periphery of the E-B area, more specifically in the E-B spacer oxide.

Globally, after Gamma-ray irradiation, we found the same tendencies as for X-ray irradiation. The comparison of the excess 1/f noise level observed after the two irradiations sources will be presented in section 3.9.

3.7.3.3 Impact of TID on G-R component

To complete the LFN analysis of the irradiated BiCMOS technologies, the G-R components are investigated as a function of TID. The extraction of cut-off frequency (f_{ci}) and plateau magnitude (A_i) were presented in detail in chapter 2. The empirical model of the irradiated G-R component is represented in 3.6. After Gamma-ray exposure, two main G-R components were detected (A_1', f_{c1}') and (A_2', f_{c2}'). This study was initiated on 6 and 30 HBTs of each BiCMOS technology, BiCMOS9MW and B55 respectively. The total studied HBTs increased along with TID.

3.7.3.3.1 Cut-off frequency study

As for X-ray, after exposure to the Cobalt60 source, two G-R components were mainly detected in the S_{IB} spectrum. As a start, the f_{ci} are investigated as a function of the total dose irradiation. f_{ci} parameter evolution will be studied as a function of several bias values and geometrical parameter.

3.7.3.3.1.1 Evolution of initial G-R components depending on I_B

Figure 3.43 presents the second G-R component cut-off frequency (f_{c2}) found on a 10.8 μm^2 BiCMOS9MW HBT device. The illustrated sample presents an initial G-R behavior. f_{c2} of the three tested currents are plotted as a function of the cumulative dose. An independency to the I_B parameter is detected by presenting f_{c2} values in the range of 200 Hz, for the three tested currents. From the study of several dice, the same f_{c2} range value is respected while presenting a negligible dispersion effect in response to the irradiation exposure.

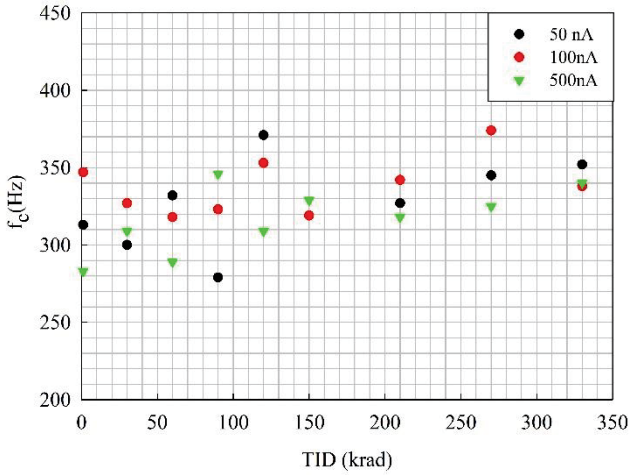

Figure 3.43. Cut-off frequency f_{c2} of the second G-R component for a 10.8 µm² A_E BiCMOS9MW HBT.

The first G-R component submitted a similar f_{c1} tendency comparing to the second G-R component. f_{c1} values in the range of 20 Hz are extracted independently to the bias current and during the irradiation exposure. The B55 technology respected similar f_{ci} behaviors and values for both G-R components. These results can be directly compared to previous ones obtained on the X-ray irradiation study.

3.7.3.3.1.2 Evolution of initial G-R component depending on A_E

The dependency on the emitter surface A_E is examined in this section for several HBT geometries. This study is held with the B55 technology presenting in Figure 3.44 the first G-R component for 4 emitter surfaces. The selected devices have recorded G-R spectra before irradiation. Initial f_{c1} values are detected in the range of 20 Hz independently to the emitter geometry. The f_{c1} values have maintained to the same level over the irradiation exposure. The study of the second G-R component has respected the same tendency described in Figure 3.44.

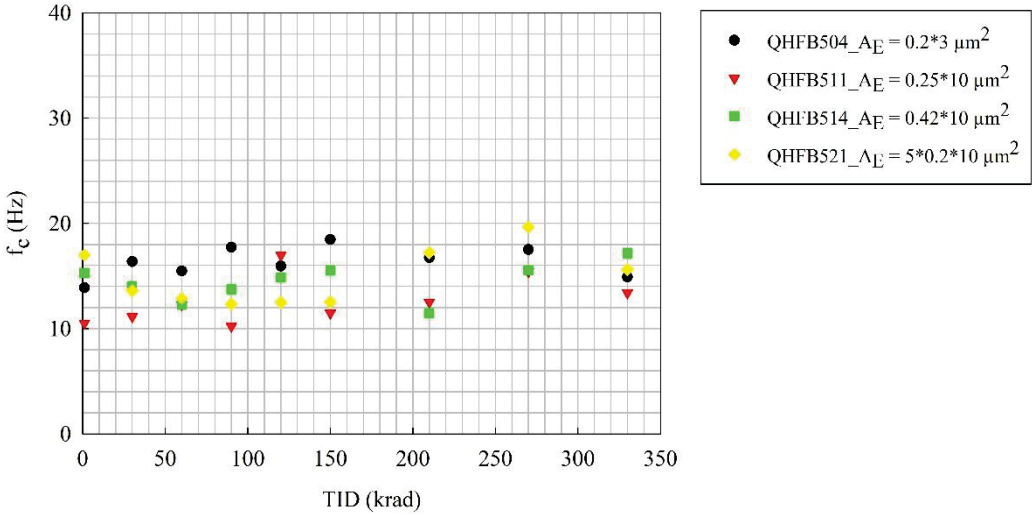

Figure 3.44.Impact of the geometrical parameters on the cut-off frequency f_{c1} of the B55 HBTs first G-R component.

BiCMOS9MW technology has presented fewer HBTs with pristine G-R components. Nonetheless, a f_{ci} independency to the emitter geometry can be extracted from the analysis of two emitter geometries.

3.7.3.3.1.3 Comparison of initial versus induced cut-off frequencies

Irradiation exposure of HBTs with an initial G-R spectrum was found to maintain the same f_{ci} values. In this section, a comparison of the two cut-off frequencies of both induced and initial G-R components will take place as a function of the cumulative dose. Figure 3.45 illustrates their evolution for emitter geometries of 4.05 μm^2 and 2.5 μm^2 for BiCMOS9MW and B55 technology respectively. The overcome of the G-R component over the 1/f noise is recorded at 120 krad and at 210 krad for the presented devices.

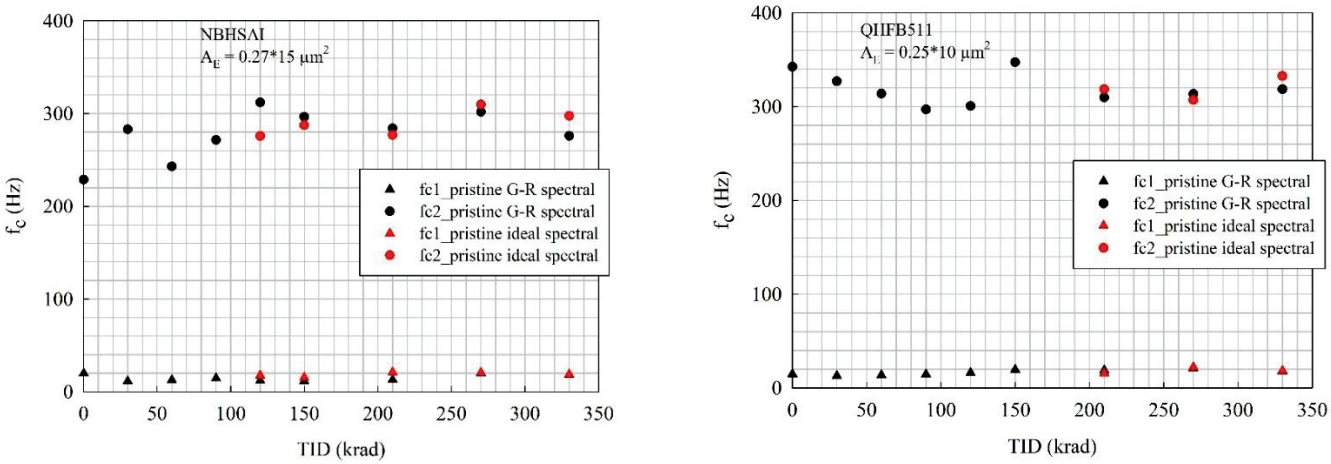

Figure 3.45. Comparison of the fci cut-off frequencies of both pristine and induced G-R components after irradiation exposure for BiCMOS9MW (NBHSAI) and B55 (QHFB511)

The induced G-R components of both technologies have respected the same f_{ci} level found for initial G-R spectrum. This behavior was detected by the two G-R components. Thus, irradiation exposure is responsible for activating the existing trap levels in the devices. The empirical G-R SPICE model correlates with the proposed model in eq. 3.6.

3.7.3.3.2 G-R plateau magnitude study

In this section, the plateau magnitude of both G-R components is investigated as a function of the cumulative dose. This parameter is identified by A'_i in the model 3.6. Both initial and induced G-R components are investigated in response to TID. G-R magnitudes will be studied as a function of emitter geometries and current biases.

3.7.3.3.2.1 Plateau magnitude evolution of initial G-R as a function of TID

The degradation response of the two magnitudes towards the TID effect is studied for both technologies. Figure 3.46 represents the normalized with I_B^2 plateau magnitudes of the two G-R components (G-R1 and G-R2) of each technology as a function of TID for the three base bias currents. The selected devices present a comparable A_E in the range of 2.5 μm^2.

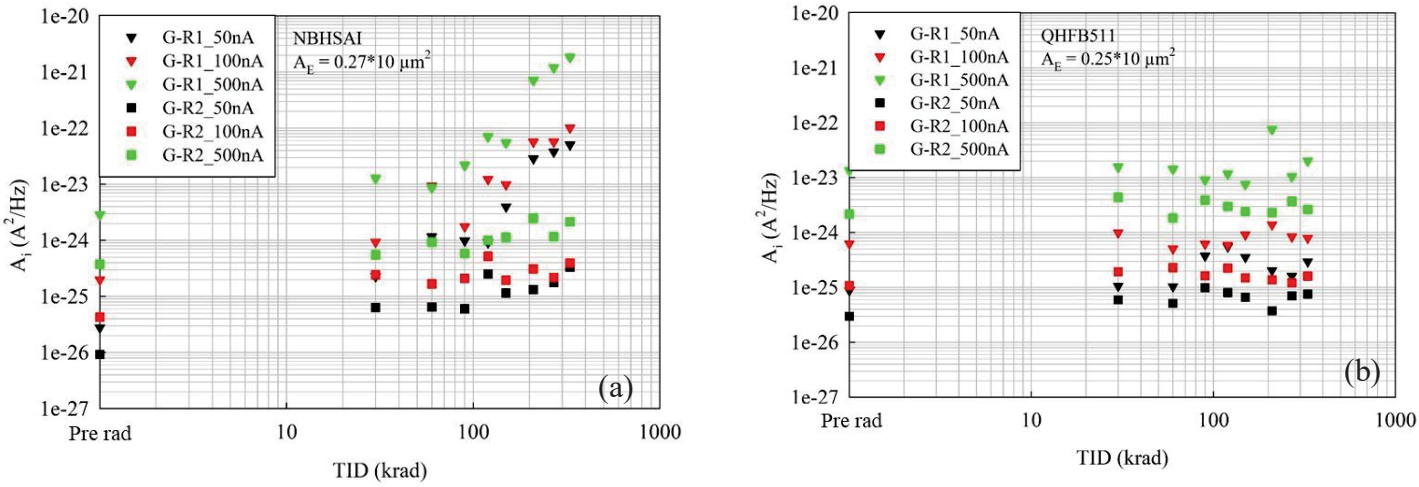

Figure 3.46. Normalised G-R magnitudes analysis of both a) BiCMOS9MW and b) B55 technologies as a function of the cumulative dose.

A distinct degradation response was found for each technology. A linear increase as a function of the cumulative dose is marked for the two BiCMOS9MW G-R plateaus as illustrated in Figure 3.46.a. These increases are due to the creation of new trap centers after each irradiation exposure. Nonetheless, the first G-R component is highly affected by the irradiations with an increase of 2 decades higher comparing to the second G-R component.

Contrarily to the BiCMOS9MW, the B55 technology have preserved the same magnitude level during the irradiation process. Both G-R components have respected the same irradiation response. This behavior is illustrated in Figure 3.46.b.

The same tendencies were extracted for the other HBT geometries and on multiple dice of each technology.

3.7.3.3.2.2 Comparison of initial and induced plateau magnitudes

A comparison of the magnitude level of each G-R component is established for both pristine and induced ones. This study is illustrated in Figure 3.47 for both technologies. The illustrated results correspond to the same HBTs studied in Figure 3.45.

The two induced G-R components, after a dose of 150 krad and 210 krad for BiCMOS9MW and B55 respectively, have presented similar magnitudes level and tendencies compared to the initial ones.

A significant increase of the plateau magnitude occurs for the irradiated HBTs of the BiCMOS9MW over the B55. This effect is clearly observed on the first G-R component comparing to the second one. These tendencies are extracted independently to the HBTs geometry.

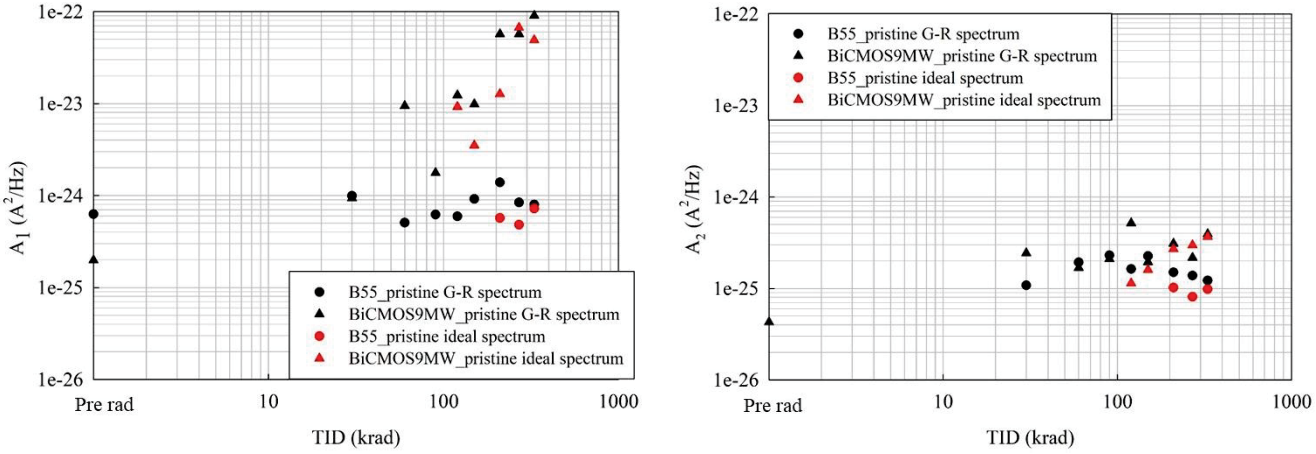

Figure 3.47. Magnitude comparison of both initial and induced G-R components after irradiation exposure, A_E ≈2 µm².

3.7.3.3.2.3 Plateau magnitudes evolution in response to A_E

To localize the G-R components, the two G-R magnitudes are examined as a function of A_E. This analysis is held at three states: before irradiation, after 150 krad and after 330 krad. 5 HBT geometries of the B55 and 3 of BiCMOS9MW are studied. The results are presented Figure 3.48. The presented data presents the magnitude level for an I_B value of 100 nA.

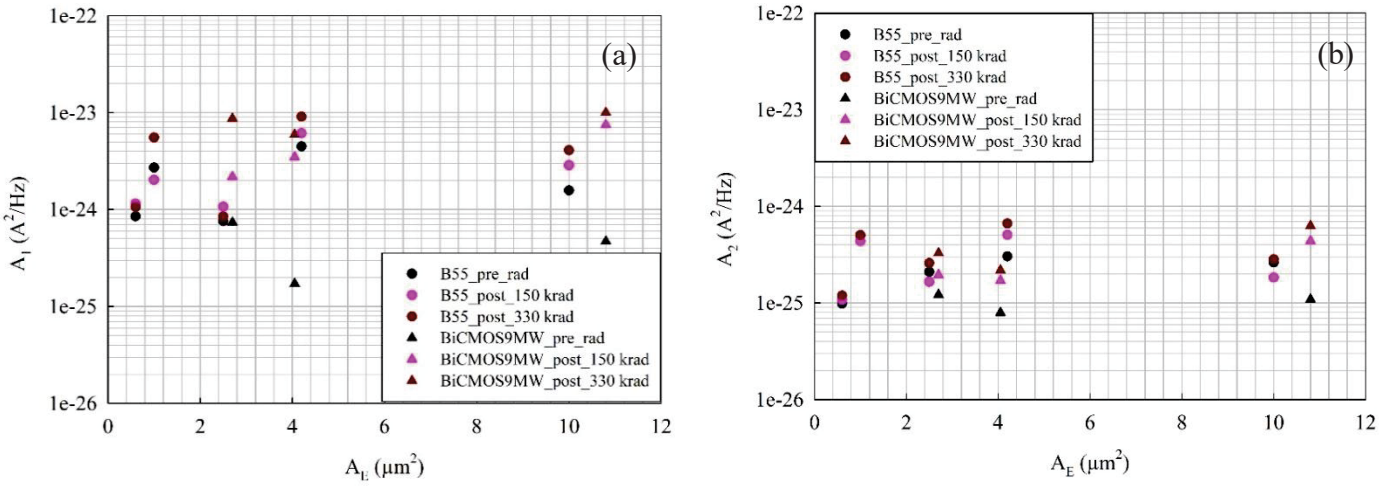

Figure 3.48. Irradiation response of the a) first and b) second G-R magnitude as a function of the A_E for an I_B equal to 100 nA.

The first G-R magnitude, illustrated in Figure 3.48.a, has presented an independency to A_E at initial state. This behavior was examined for both technologies. Regardless of the exposed dose, irradiated HBTs have maintained an A_E independency. Concerning the second Lorentzian magnitude represented in Figure 3.48.b, the same behavior can be concluded. A similar tendency was detected for the three tested currents.

Since both G-R magnitudes are independent of the A_E parameter, the intrinsic emitter surface cannot be the localization of the initial and induced G-R noise sources.

3.7.3.3.2.4 Plateau magnitudes evolution in response to P_E

In this section, the Lorentzian magnitudes are examined as a function of the P_E. Figure 3.49 presents the normalized magnitudes (A_i/A_E) in response to P_E/A_E ratio for several irradiation exposure. The analysis is accomplished at three states: before irradiation, after 150 krad and after 330 krad. An I_B value of 100 nA is considered for the illustrated study.

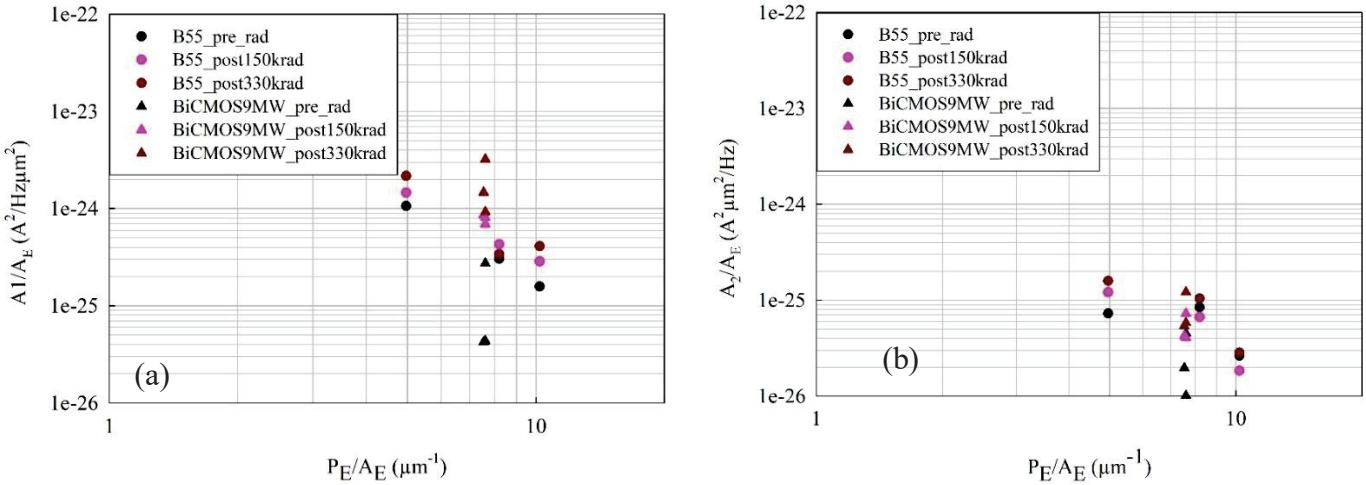

Figure 3.49. Irradiation response of a) A_1/A_E and b) A_2/A_E as a function of the P_EA_E for an I_B value of 100 nA.

As already presented in chapter 2 and during the X-ray study, before irradiation, B55 HBTs have presented a linear decrease in the normalized magnitude as a function of the P_E. This tendency is found for the two studied Lorentzian presented in Figure 3.49.a and Figure 3.49.b. Concerning the BiCMOS9MW, the same difficulty observed in the X-ray irradiation is pointed out due to the limited PE/AE ratio range values.

Both G-R components have presented a linear dependency on the P_E parameter while a none-dependency to A_E. Therefore, we can assume that the G-R noise sources are located at the periphery of the emitter junction.

3.7.3.3.2.5 Plateau magnitudes evolution in response to I_B

The two plateau magnitudes are investigated in response to the input current, for two geometries of each technology, in Figure 3.50. A 0.6 μm^2 and 10 μm^2 for the B55 while 4.05 μm^2 and 10.8 μm^2 for the BiCMOS9MW are presented in the figure below as HBT1 and HBT2 respectively for each technology. Both plateau magnitudes are plotted before and after the irradiation process. With the few current biases, only tendencies can be proposed.

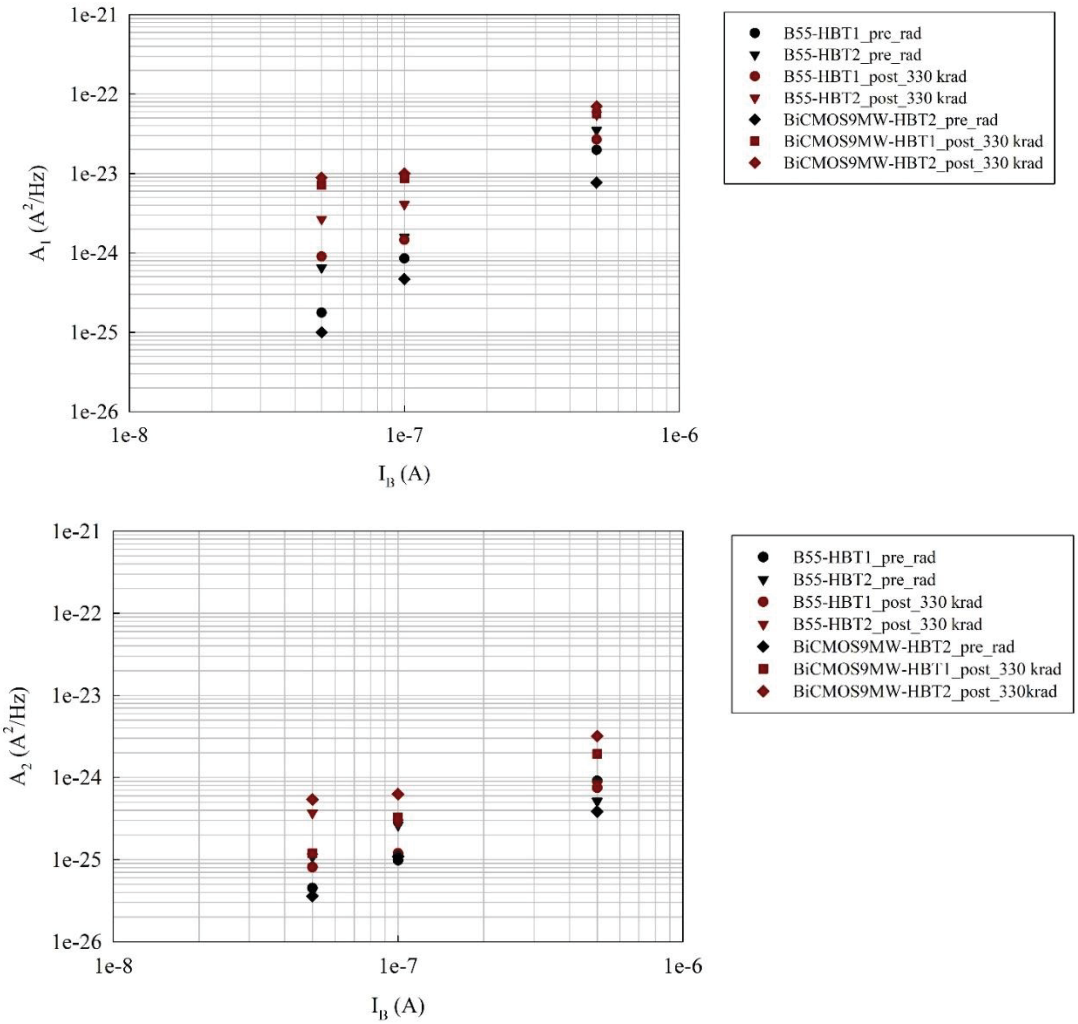

Figure 3.50. Irradiation response of both G-R magnitudes as a function I_B for several HBT geometries.

Figure 3.50 describes a similar behavior than the one found after X-ray exposure. An I_B^2 dependency is found for the first G-R component on initial state HBTs of both technologies. This quadratic dependency shifted to a near linear one after Gamma-ray exposure of the BiCMOS9MW HBTs. While for the second G-R component plateau, the initial I_B^{α} dependency, $1<\alpha<2$ (presented earlier in chapter 2), shifted after exposure to a near linear one for both technologies. On the contrary, both irradiated plateaus of the B55 did not present a change in the slope.

Thereby, the proposed empirical models of both first and second Lorentzian after X-ray exposure, in relation 3.7 and 3.8 respectively, are valid to depict the induced G-R component after Gamma-ray irradiation.

3.7.4 Annealing response after Gamma-ray exposure

As previously established after X-ray irradiation, the induced traps are investigated by two annealing procedures: isothermal and isochronal annealing. 4 selected devices, from each technology, were examined in response to the annealing procedure. The devices that are treated are the ones presenting free G-R spectra at pristine state. DC and LFN analysis were established

for a possible healing effect on the induced defaults in the components after each annealing process.

3.7.4.1 Time effect before annealing

The isothermal at room temperature annealing was processed after 4 months after the last Gamma irradiation exposure (TID = 330 krad).

DC analysis can be examined in Figure 3.51 at t_0 for both technologies. The illustrated devices correspond to an A_E HBTs of 4.05 μm^2 and 4.2 μm^2 for the BiCMOS9MW and the B55 respectively. As presented in Figure 3.51, at Time = 0, a slight healing impact was found at room temperature by presenting a distinct $\Delta I_B/I_B$ level. The time effect presented a higher impact on the BiCMOS9MW technology comparing to the B55, this can be due to their higher degradation after irradiation exposure.

Concerning the LFN analysis, a slight or negligible impact was extracted after 4 months of annealing at room temperature. This behavior can be found in Figure 3.52 Figure 3.52by the red and the green spectra.

These tendencies were systematically extracted for the two technologies independently of the emitter geometry.

3.7.4.2 Thermal annealing effect

This process was established in a total of 434 hours. HBTs were placed in a furnace for 386 hours at a temperature of 100 °C followed by an annealing at 130 °C for 48 hours. As already detailed, the annealing at 100 °C is responsible of healing the induced traps in the oxide layers and at higher temperature the annealing effect leads to a higher healing impact [126]. DC and LFN measurements are done for several steps.

3.7.4.2.1 DC analysis

Figure 3.51Figure 3.51 represents the variation of Delta I_B/I_B as a function of the TID and the annealing time. The normalized excess current is extracted at a V_{BE} value of 0.42 V and 0.46 V for BiCMOS9MW and B55 respectively. The illustrated devices correspond to a 4.05 μm^2 and a 4.2 μm^2 A_E HBTs.

After the first annealing step, after an annealing at 100 °C for 48 hours, a significant healing effect has marked both HBTs, particularly the BiCMOS9MW ones. By establishing other healing steps at the same temperature of 100 °C till a cumulative total hour of 316 hours, the healing effect is less significant for the BiCMOS9MW that have presented a stable excess current level after 96 hours, contrarily to the B55 which have presented a decrease of nearly two orders of magnitude. After 316 hours, the DC performance of the B55 has regained a similar performance recorded on the pristine HBT.

Since the B55 has regained its pristine DC state, only the BiCMOS9MW was examined for the rest of the study. Before initializing new annealing process with an increased temperature, another annealing step of 70 hours was established inducing a low healing effect of the induced traps.

After an annealing process of 386 hours, a new annealing temperature of 130 °C was introduced to examine the BiCMOS9MW response. A high decrease of Delta I_B/I_B is observed, the resulted I_B current has presented a high recovery after 48 hours of annealing.

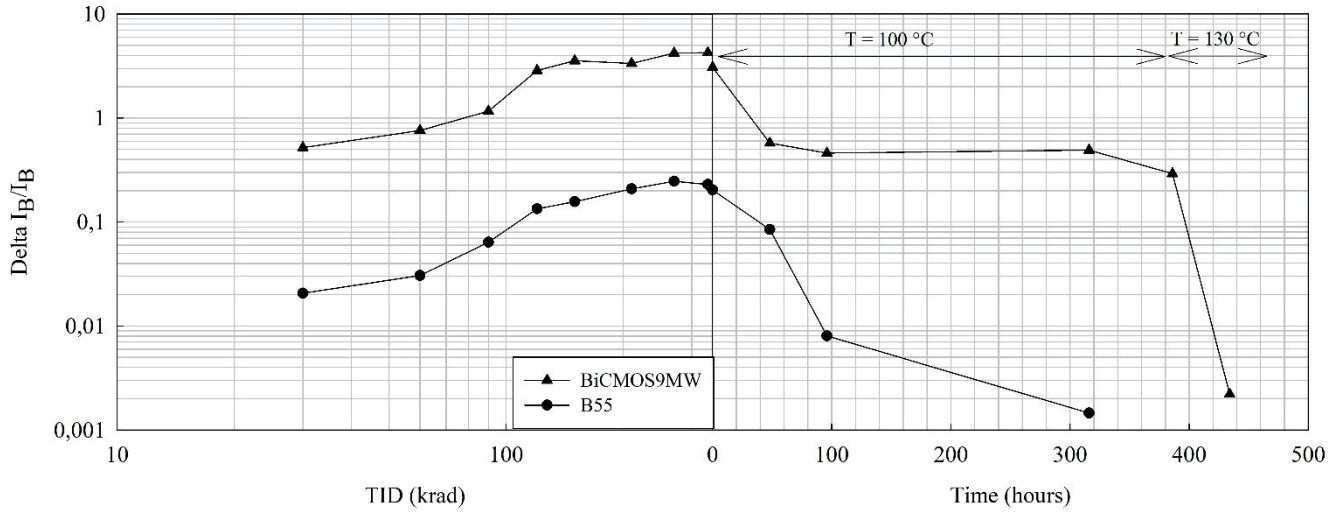

Figure 3.51. Variation of normalized excess base current for irradiated and isochronal annealed HBTs of both technologies.

The recorded behavior was witnessed for the other selected transistors independently to their emitter surface.

3.7.4.2.2 LFN analysis

The annealing impact on the LFN response is illustrated in Figure 3.52 for the two technologies. The HBTs present an A_E of 2.5 µm2 and 4.2 µm2 for BiCMOS9MW and B55 respectively biased at 100 nA.

Contrarily to the observed DC results at Time = 0, a negligible healing effect was depicted for LFN measurements of both technologies. The annealing process of the BiCMOS9MW presented a quasi-healing effect. The 1/f noise components were found after the 130°C thermal annealing with one decade higher comparing to the pristine state. However, a thermal annealing of 100°C was sufficient to restore a total recovery for the B55 device. The described behaviors were observed independently to the current bias and emitter geometries.

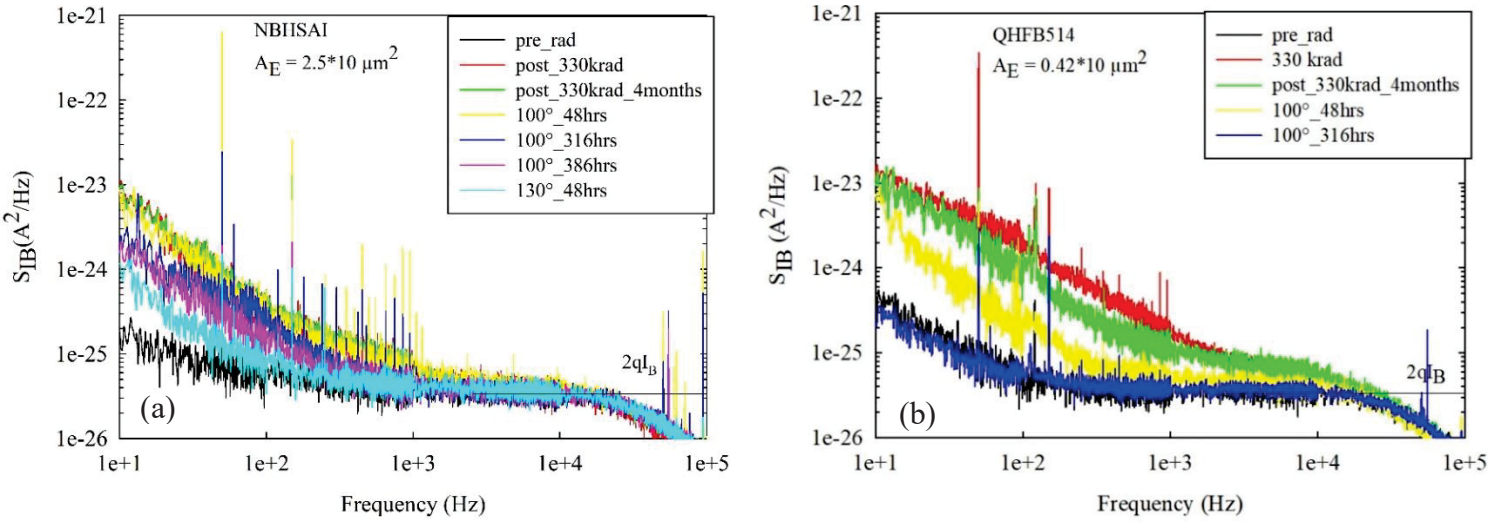

Figure 3.52. Evolution of LFN spectra as a function of multiple annealing processes for BiCMOS9MWand B55, for I_B = 100 nA

3.8 Comparison of X-ray and Gamma ray impacts on HBTs

Each irradiation source emits energetic photons in a specific energy band and a dose rate well defined. Therefore, a comparaison of the induced damages by X-ray and Gamma ray sources will be investigated, based on DC (forward Gummel mode) and LFN (1/f noise and G-R components) analysis. To compare the effects induced by the two sources on DC and LFN levels, an equivalent dose is needed. This conversion, based on NIST tables [129] , was provided by the radiation team. This conversion is presented in 3.9.

$$TID_{Equivalent\ Gamma\ Dose} = 2.8 \times TID_{X-ray} \qquad 3.9$$

3.8.1.1 Comparison of the DC characterization

The analysis of both irradiation sources impacts mainly resulted in a higher radiation tolerance for the B55 over the BiCMOS9MW technology. X-ray and Gamma-ray exposure were found to induce trap centers in the E-B and STI oxides. Nevertheless, the radiation response of each oxide showed dissimilarity in their tolerance according to their composition, an oxide/nitride whereas a silicon dioxide for the E-B spacer and the STI oxide respectively. Thereby, enhanced degradation impact is found in the E-B spacer oxide when compared to the STI oxide during X-ray exposure while a higher sensitivity of STI oxide was found after Gamma ray exposure [128].

At first, a comparison in low-injection regime is presented to resume the results discussed previously for both X-ray and Gamma-ray and to interpret their degradation level. Since an impact on I_C was observed after Gamma-ray irradiation, further investigation will be heled on I_C in both low-injection and diffusion regime.

Figure 3.53 illustrates the excess base current after each irradiation process at VBE values of 0.42 V and 0.46 V, near the recombination area, for B55 and BiCMOS9MW respectively. The presented results correspond to three emiter geometries in the range of 2.5, 4 and 10 µm^2.

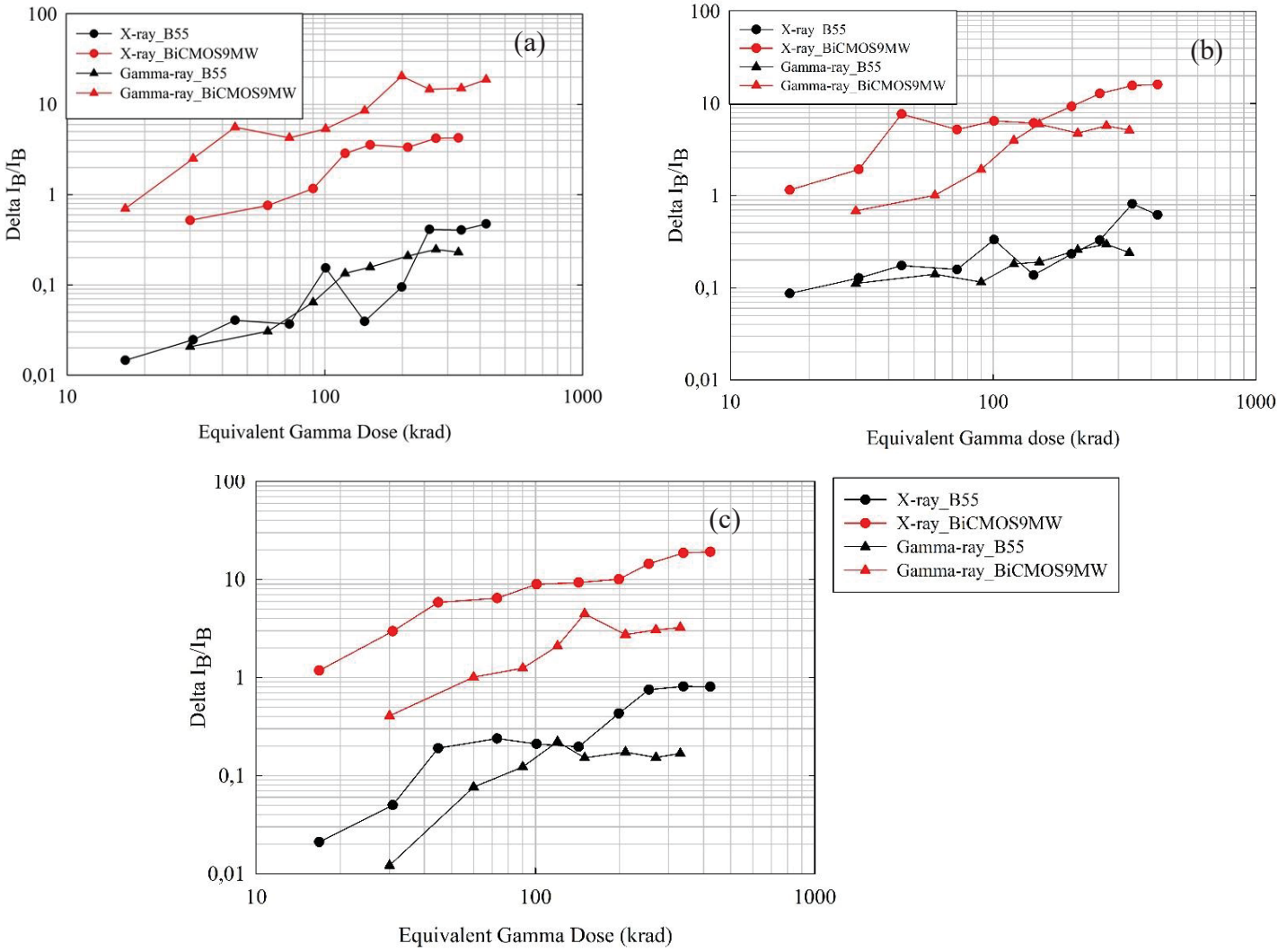

Figure 3.53. X-ray versus Gamma irradiation comparison for I_B, near the low-injection area, for both BiCMOS9MW and B55 respectively a) A_E =4.05µm² and A_E = 4.2 µm², b) A_E =2.7µm² and A_E = 2.5 µm² and c) A_E =10.8µm² and A_E = 10 µm²

As previously concluded after each exposure, a linear increase in $\frac{\Delta I_B}{I_B}$ occured in response to TID. The degradation level of the B55 presents a similar impact level with less than 10% of difference between X-ray and Gamma-source as can be seen in Figure 3.53. Therefore, a dependency to the irradiation source can be assumed. Contrarily to the BiCMOS9MW, a clear depency to the irradiation source can be assumed. The degradation level after X-ray exposure is produced a higher degradation impact on the HBTs comparing to the one after Gamma-ray exposure. The behavior is respected independnetly to the irradiation source as can be found in Figure 3.53.

Since X-rays induce a higher degradation impact in the E-B spacer oxide, the distinct impact on each technology is related to the shrinking of the technology leading to a decrease in the oxide layer thicknesses in the E-B spacer oxide in the B55.

A complementary study on the I_C degradation was done for additionnal information on the comparison of the two sources impact. Figure 3.54Figure 3.54 illustrates the excess collector current bias near the low-injection regime of both technologies in response to TID.

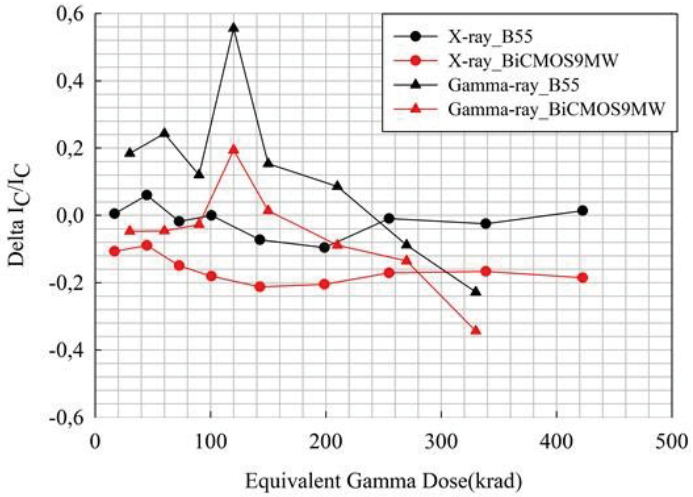

Figure 3.54. X-ray versus Gamma irradiation comparison for I_C, near the low-injection area, for both BiCMOS9MW and B55 with A_E =4.05µm² and A_E = 4.2 µm² respectively

As can be seen in the graph, a distinct degradation response was found after each exposure independently to the BiCMOS9MW technology. A significant degradation impact was marked after Gamma-ray exposure while a near stable level was found after the X-ray exposure. The same tendencies were observed for irradiated HBTs independently to their geometries.

Moreover, the excess collector current was studied in the diffusion regime as presented in Figure 3.55. A similar degradation behavior was depicted comparing to the one found for I_C near the recombination regime.

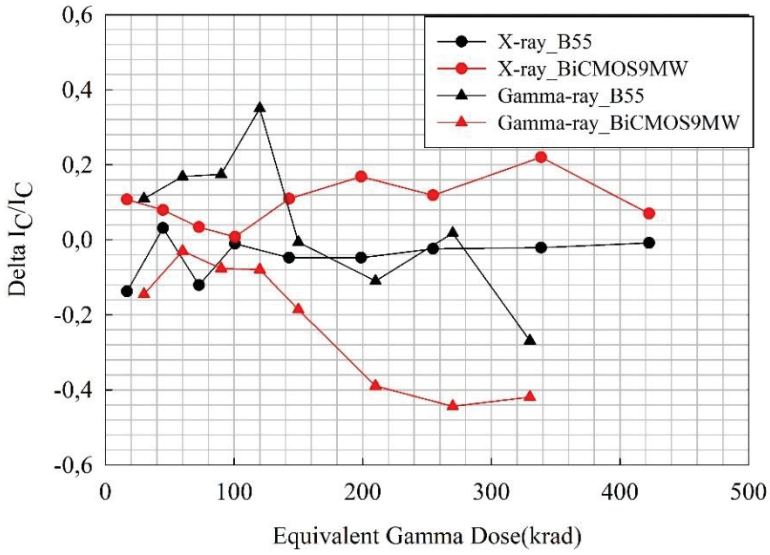

Figure 3.55. X-ray versus Gamma irradiation comparison for I_C, in the diffusion regime, for both BiCMOS9MW and B55 with A_E =4.05µm² and A_E = 4.2 µm² respectively

This phenomenon is related to the fact that STI oxides are more sensitive to Gamma-ray exposure. Hence, more G-R centers are created at the STI oxide causing a higher degradation of the I_C level.

3.8.1.2 Comparison of the LFN characterization

As presented earlier, B55 technology has mainly presented a higher tolerance comparing to the BiCMOS9MW. This behavior was respected by the two irradiation sources. Since the irradiation response of S_{IC} was not examined, the induced damages in the E-B region are only investigated (contrarily to the induced damages in the STI oxide). In this section, a comparison of the induced degradation response will be established for both 1/f noise and G-R component levels.

3.8.1.2.1 1/f noise analysis

Figure 3.56Figure 3.56 represents the 1/f noise evolution as a function of the equivalent gamma dose in response to each irradiation source. Two transistors from each technology are presented. A slightly higher tolerance is found after Gamma-ray exposure, by maintaining an ideal spectrum for a higher TID. The selected devices preserved a pure 1/f noise spectrum for an equivalent dose of 73 krad/90 krad and 254 krad/330 krad after X-ray/Gamma-ray respectively for BiCMOS9MW and B55.

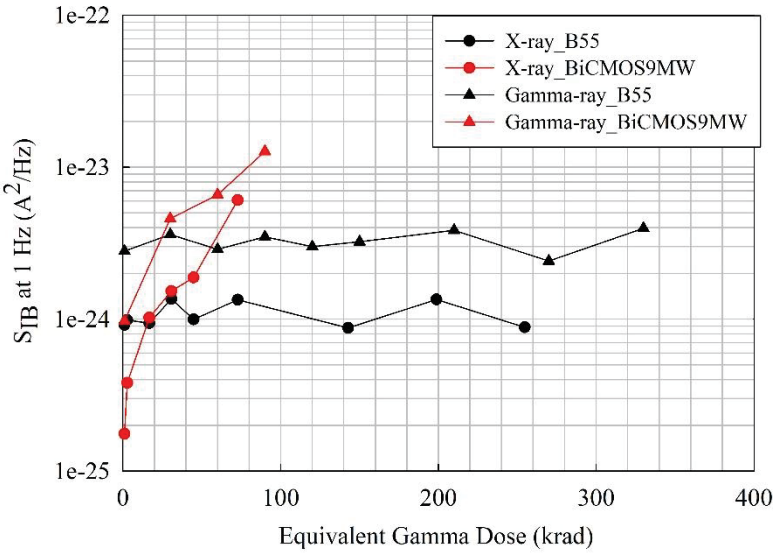

Figure 3.56. Evolution of 1/f noise level as a function of equivalent Gamma Dose for BiCMOS9MW (A_E = 4.05 μm^2) and B55 (A_E = 4.2 μm^2).

The distinct S_{IB} at 1 Hz levels witnessed for the pristine devices of each technology result from the dispersion effect presented earlier in chapter 2. Thus, the direct comparison of the 1/f noise level it is not possible, we will be just discussed about the behaviors. Similar irradiation tendencies were observed after each source exposure. The B55 HBTs have maintained a stable 1/f noise level while an increase with the same dynamic in the noise level marked the BiCMOS9MW ones.

3.8.1.2.2 G-R analysis

Figure 3.57Figure 3.57 depicts the comparison of the two irradiation sources impact on the G-R plateaus, A1 and A2. The two plateaus are plotted as a function of the equivalent gamma dose for the two technologies.

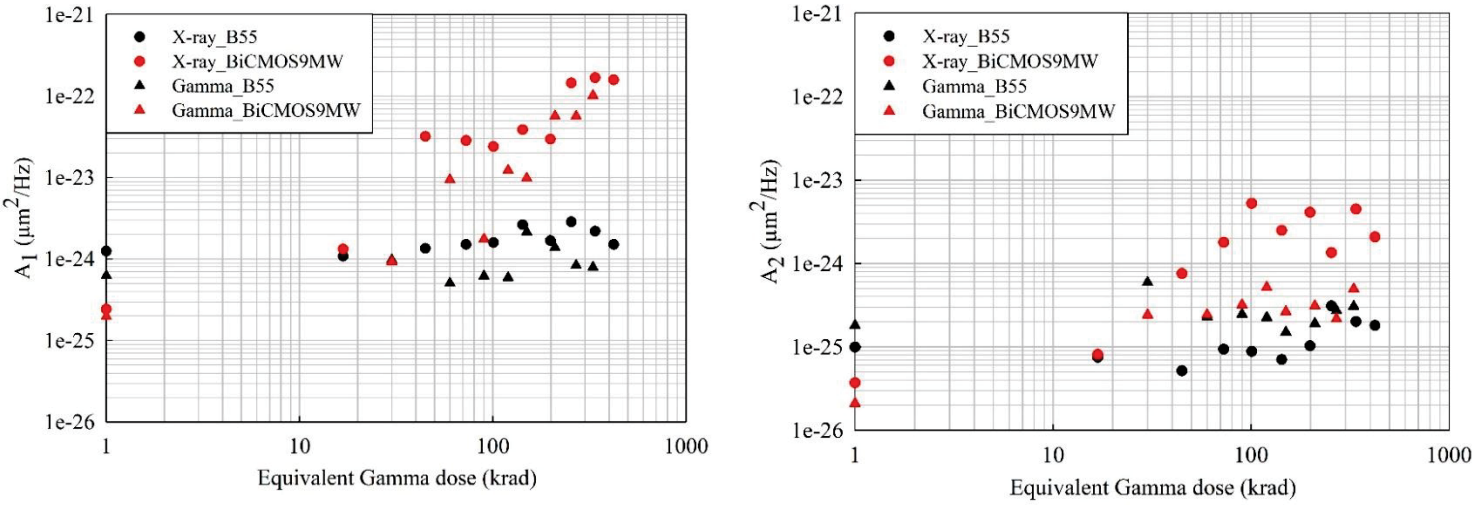

Figure 3.57. Evolution of a) $A_1$and b) A_2 as a function of equivalent Gamma Dose

A negligible dependency to the irradiation source was found for A1 of both technologies as presented in Figure 3.57.a. This effect was respected by A2 of the B55 contrarily to the A2 of the BiCMOS9MW where a higher degradation impact is pronounced after X-ray exposure.

Earlier studies, in 3.5.4.3 and 3.7.3.33.7.3.3, proven that the induced G-R trap centers are suspected to be located at the E-B periphery. Moreover, by comparing the two irradiation sources impact, the second G-R component of the BiCMOS9MW presenting a higher degradation impact after X-ray exposure is suspected at the E-B spacer vicinity.

3.9 Conclusion

In this chapter, X-ray and Gamma-ray TID degradation impact on the DC characteristics and on the LFN was studied on Si/SiGe:C HBTs of the two BiCMOS technologies.

After X-ray exposure, DC and LFN analysis resulted in a higher tolerance for the B55 technology comparing to the BiCMOS9MW. A higher excess I_B current is recorded for the BiCMOS9MW, induced by the generation of trap centers in the E-B area. 1/f noise and G-R components were both investigated in response to the TID. Independently to the noise sources, the B55 presented a more stable noise level. Ideal spectra are mainly recorded until a dose of 26 krad and 91 krad for BiCMOS9MW and B55 respectively. The 1/f noise was examined as a function of I_B and geometrical parameter to locate their noise sources. After irradiation exposure, the 1/f noise sources are mainly located at the intrinsic E-B surface for the B55 HBTs. However, for the BiCMOS9MW HBTs, the induced 1/f noise sources were highlighted at the E-B periphery, mainly at the E-B spacer oxide. Concerning the G-R components, two components were detected with f_{ci} values in the range of 20 Hz and 200 Hz. The irradiation exposure induced significant trap centers

in the BiCMOS9MW contrarily to the B55. The study of the Lorentzian parameters in response to TID were investigated as a function of I_B and geometrical parameters to pinpoint the emitter periphery as a main area for the induced traps. Nonetheless, the localization of the G-R components is more challenging due to the lack of physical G-R models.

Similar studies were established after X-ray and Gamma-ray exposure. The analysis presented similar tendencies depicting a higher tolerance for B55 technology. Ideal spectra were mainly maintained up to a dose of 90 krad and 150 krad for BiCMOS9MW and B55 technology respectively. The 1/f noise study resulted in the creation of induced trap centers at the E-B periphery especially in the spacer oxide of the BiCMOS9MW contrarily to the B55 which presented a negligible irradiation impact. Concerning the G-R components study, both technologies mainly presented two Lorentzian components with f_{ci} values in the range of 20 Hz and 200 Hz. The Lorentzian parameters were examined as a function of I_B and emitter geometry dimensions to identify that both G-R components are located at the E-B periphery.

Each irradiation technique was followed by a time effect and a thermal annealing process. A higher healing impact for the induced damages was more pronounced after the Gamma-ray exposure. In both cases, an enhanced healing behavior was recorded by the B55 technology.

A comparison of each degradation source was examined, a similar degradation response is found for both technologies. Nonetheless, a variation in the degradation level was mainly pronounced for the BiCMOS9MW which is associated to the radiation response of E-B spacer oxide and STI oxide to each source. The induced trap centers responsible of the 1/f noise and the second G-R components is found to be more important after X-ray exposure and is suspected to be located near the E-B spacer oxide, contrarily to the first G-R component that presented ta similar number of trap centers.

DC and 1/f noise results and approaches are similar to what was observed on different types of stress applied to Si PE-BJT and Si/SiGe HBTs : after hot-carrier stress [46][130][10][131], after proton-irradiation [71]. Independently to the applied stress, the E-B spacer oxide region was proposed/demonstrated as the main induced defect localization area. Hence, the origin of these induced defects in electronic devices were earlier suspected as defects in the oxide regions (mainly at SiO_2 interfaces) interacting with charge carriers [132]. Concerning advanced bipolar transistors, studies on different irradiation types, often highlighted the Emitter-Base spacer oxide interface [118][125]. Moreover, recent published data on physical simulation and/or compact modelling of Si/SiGe HBTs [133][134] pointed out the role of the passivated Si-H bonds along Si/SiO_2 interfaces. For instance, such physical approach could be used to confirm the positive role of the reduction of the oxide thickness concerning the hardness of the B55 technology.

Even if in some cases only tendencies were presented, the complete G-R components analysis presented in this work confirms the predominant role of the periphery in the localization of the induced defects by X-ray and Gamma irradiations.

Promising results are found for Si/SiGe HBTs of the BiCMOS technology in extreme environments especially for the B55 BiCMOS technology.

General conclusion

BiCMOS technologies proven to be a superior technology comparing to RF CMOS technologies providing higher gain, lower noise figure and lower power consumption in high frequency systems. Even if SiGe HBTs performances are still a little behind compared to III-V ones, Si technology presented additionally a lower manufacturing cost and an ability to integrate complex digital functionality. Therefore, nowadays, SiGe BiCMOS technology is considered the best candidate for high volume RF and mm-wave applications.

In this thesis, Si/SiGe HBTs issued from a BiCMOS technology were investigated. These HBTs, developed by STMicroelectronics, are issued from a 55 nm BiCMOS technology and are highly studied in the manuscript specially through their LFN characterization. A previous mature technology of a 130 nm CMOS node, BiCMOS9MW, was also investigated as a reference to point out the achieved development through the B55. The technological development, during this project, resulted in an improvement in the frequency response (f_t, f_{max}) from (230 GHz, 280 GHz) to (320 GHz, 375 GHz). Low-Frequency Noise characterization was intensively used in this thesis as a characterization tool to test some specific technological developments and to study the impact of two irradiation sources. Moreover, since the frequency response of the associated IC circuits is directly affected by the low frequency behavior of HBT (up-conversion phenomenon), LFN compact modelling was studied.

At first a general introduction of LFN domain was given presenting the needed test bench and the LFN components that can occur in semiconductor devices. Physical models for the excess noise components, 1/f noise and G-R components, were presented. The given interest by circuit designers in the LFN domain resulted mainly in simplified 1/f noise compact models. A simplified model for G-R components was also presented. The state-of-art, of three types of bipolar transistors (BJT, PE-BJT and HBT) was introduced.

Two variations of the B55 technology were provided in this work to investigate the technological development while referring to the BiCMOS9MW. This investigation presented the studied topic of the second chapter. Two of the developed technological parameters are the Collector structure and the dopant activation technique. The investigation in response to the Collector structures presented three types of HBTs: High Speed, High Voltage and Medium Voltage. The variation of its structure resulted in a distinct DC and HF response while a negligible impact was observed after the LFN spectroscopy mainly through 1/f noise analysis. Based on the usual 1/f noise SPICE modeling, an I_B^2 and $1/A_E$ dependency were respected for each HBTs' structure. The investigated FOM resulted in the extraction of a K_B value in the range of $10^{-9}\mu m^2$ for the three devices. The second investigated technological parameter, dopant activation technique, depicted an improved performance in both DC and LFN response. A K_B value of $7\ 10^{-10}\mu m^2$ for B55 DSA, comparable to the extracted BiCMOS9MW one with a value of $6\ 10^{-10}\ \mu m^2$, while a higher value of $1.5\ 10^{-9}\mu m^2$ was detected for B55 TH. A second FOM, f_c/f_t, was examined which combines the device's performance in both Low-Frequency Noise and High-Frequency domains. This study revealed a similar behavior for B55 DSA and BiCMOS9MW. Moreover, G-R components were also studied for theB55 technology. This study resulted mainly in the presence

of two G-R components attributed to two cut-off frequencies in the range of 20 Hz and 200 Hz. Further investigation on the plateau magnitudes, as a function of emitter geometries and current bias, led to extract a compact model for each Lorentzian plateau. The noise sources were suggested at the Emitter periphery of the interface oxide/E-B space charge region.

Analysis took place in chapter 3 to investigate the irradiation response of the studied HBTs. The irradiation exposure was established in a total ionizing dose process (TID) using X-ray and Gamma-ray sources. These impacts were examined on both DC and LFN measurements for each BiCMOS technology. Independently to the source's type, similar behaviors were concluded resulting in a higher tolerance for the B55 technology. Through DC analysis, excess base current presented a linear increase in response to the TID with a more pronounced excess current for BiCMOS9MW devices. Hence, through LFN spectroscopy, a more detailed analysis was established. The induced noise components, 1/f noise and G-R components, were investigated as a function of the current bias and the geometrical parameters to highlight the HBTs' defected areas. After exposure, a negligible impact was found on the 1/f noise of the B55 contrarily to the BiCMOS9MW. Hence, the induced 1/f noise sources of the BiCMOS9MW were highlighted at the E-B periphery more specifically at the E-B spacer oxide. Concerning the G-R components analysis, the induced noise components of both technologies pinpointed the Emitter periphery as a main localization area for the induced sources. Even though similar tendencies where extracted, each irradiation source presented a more pronounced degradation effect on either E-B spacer or STI oxides. The distinct oxides' response was found by comparing the degradation levels induced after X-ray and Gamma-ray exposure. A higher impact was found in the excess base current of BiCMOS9MW after X-ray exposure related to the E-B spacer oxide response, while Gamma-rays induced a modification in the Collector current depicting the STI oxide response. After the final dose exposure of each irradiation procedure, a healing effect was investigated as a function of a long time period and in response to the thermal annealing effect. The established annealing processes revealed a more significant healing effect for Gamma-ray exposed HBTs. A total healing effect was found for the B55 while a quasi-healing one was revealed from the BiCMOS9MW.

Eventually, along to the standard LFN study mainly established in this community, additional investigations took place in this thesis concerning the G-R components and the irradiation impact on HBTs. The presented results on the two subjects are one of the few investigations established in the literature.

Perspectives

Within this thesis, the Low Frequency Noise research team initiated studies in order to evaluate the impact of irradiations on Si/SiGe HBTS issued from the latest BiCMOS technology developed by STMicroelectronics. However, outstanding issues and results remain to be confirmed such as the origin of the induced defects, their location, … Answers to these questions, as well as new studies, could be investigated within the framework of a new European project.

This European project, called INCREASE, with the same partners in addition to few others, is currently being evaluated. The main objective is to improve the integration of newest technologies while reducing the limiting obstacles. In the continuity of the previous European TARANTO project, the new project will focus on the technological development of Si/SiGe BiCMOS technology at a higher TLR level.

The main aim of industrials is to keep on developing new generations with improved frequency responses corresponding to the demands of future RF, THz and mm-wave applications. This requires the implementation of a new Si/SiGe:C BiCMOS technology. The target of this technology is to reach higher frequency performances in the order of 600 GHz. However, these improvements can present limitations by the system's performance overall resulting, for instance, from the packaging process. Thermal issues, package connections and interfaces problems can be induced. Packaging options will be investigated that covers some issues in the chip/package interactions.

IES laboratory will be involved in the electrical characterization from DC to HF measurements (Gummel plots, LFN and S parameters). In the continuity of this thesis, the induced irradiation effects will be investigated on unbiased and biased HBTs as a function of X-ray and Gamma-ray exposure. Hence, the development of a bench test allowing the irradiation of biased HBTs will be needed. Furthermore, irradiation studies will be established on unbiased and biased elementary systems such as VCOs and Mixers. Comparison between simulation and experimental results on the irradiated components will be done for Model Hardware Correlation. Therefore, the Low Frequency Noise team will strengthen and extend the collaborations initiated during these three years of thesis with two other research groups in the laboratory, RADIAC and TEHO, who will become full partners in this new project.

Beyond the established study on the Si/SiGe BiCMOS HBTs in this manuscript, these devices were investigated as potential THz detectors for applications such telecommunication, safety and industrial control. Thanks to the expertise of the TEHO group, the HBTs' evaluation as elementary component for communications systems based on THz frequency carriers was recently initiated and could result in an interesting research topic for the future. First results obtained on the BiCMOS9MW technology are presented in the annex "Si/SiGe HBTs as potential THz detector" of this document.

ANNEX

Beyond the study of SiGe transistors that was presented in this manuscript, we investigated the potential of these components as THz detectors, for attractive applications such as telecommunications, safety, industrial control [1][2][3]. Thanks to the available expertise at IES, we specifically focused on the evaluation of these transistors for communications based on terahertz-frequency carriers. The interest of such a carrier frequency is to offer very broadband transmissions at data rates up to hundreds of Gbps. Experimental demonstrations were already performed using different kinds of transistors such as GaAs High-Electron-Mobility Transistors (HEMT) used either as an incoherent detector for a successful 8.3-Gbps error-free communication at 300 GHz [4], or as a heterodyne detector [5]. Plasma-wave CMOS (Complementary metal–oxide–semiconductor) transistors are also attractive candidates for high-data-rate communications as reported for example in 2016 [6].

In terms of Heterojunction Bipolar structure for Transistors (HBTs), SiGe transistors have shown their potential for THz detection [7] and mechanisms of detection and noise were already investigated in [8][9]. As high-data-rates communications are concerned, InGasAs/InP were explored at Montpellier Univ. [10][11][12]. It was demonstrated that InGaAs/InP DHBTs can operate at room temperature in a large frequency range (0.14– 3.2 THz). The performances of the DHBTs as THz sensors for communications were evaluated showing that the modulation bandwidth was expected to reach 10 GHz.

As the SiGe transistors studied in this manuscript are concerned, we could validate their sensitivity to an incoming THz radiation using a carrier-less amplitude-modulated source emitting an output power close to 100 µW. Transistors were bounded to 50-ohms microstrip lines in a common-emitter configuration. As shown in Fig. 1, for a modulation frequency of 500 MHz, using a base–emitter polarization of 0.77 V, we could detect a beat signal at 1 GHz between collector and emitter, and evaluate a transistor sensitivity (detected signal in volts for a 50-ohms measurement, divided by the incoming THz power) between 0.05 V/W to 1 V/W for a 670-µm incoming beam waist. Such values are comparable to the ones reported for transistors as long as they are not coupled to an antenna. This measurement was conducted for different numbers of fingers for the transistors, as we expected a better sensitivity for an increasing number of fingers, but this was not confirmed by the experiment.

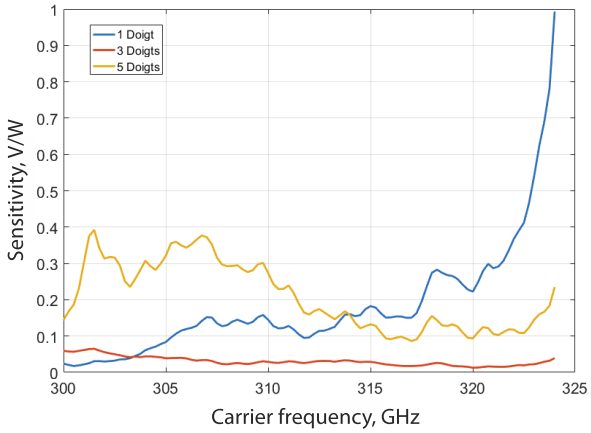

Fig. 1. Sensitivity of the SiGe transistor to a 0.5-GHz carrier-less amplitude-modulated signal at carrier frequencies varying from 300 GHz to 325 GHz. The detected signal is the 1-GHz signal measured at the collector-emitter output of the transistor using a RF spectrum analyzer. The noise level represents the measurement noise of the spectrum analyzer without any incoming THz signal on the transistor.

The capability to detect high-data-rates signals was evaluated by measuring the evolution of the detected signal for an increasing modulation frequency. As shown in Fig. 2, we observed a RC-like or RLC-like low-pass filtering of the transistor as the detected signal decreases with the increasing modulation frequency. Additionally, we observe an anti-resonance in the transistor's response as the detected signal drops at a specific frequency around 8–10 GHz. Finally, we observe a similar behavior of the sensitivity of the transistor as the base–emitter bias is tuned, with an increase of the sensitivity up to a given voltage, after which the sensitivity drops. Additionally, we could observe a 20% quasi-linear reduction of the anti-resonance frequency as the base–emitter bias was increased from 0.7 to 0.8 V.

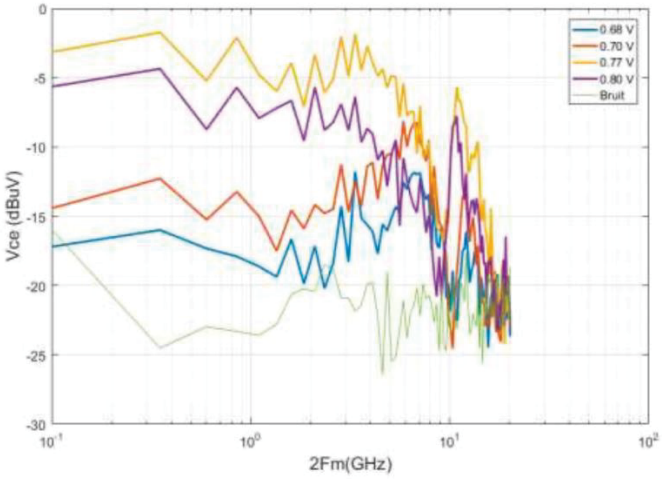

Fig. 2. Transistor's response to a 311-GHz signal with a carrier-less sinusoidal amplitude-modulation at increasing frequencies. The collector-emitter voltage is measured using a spectrum analyzer at twice the modulation frequency (beat frequency).

Similar behavior was observed on InGaAs/InP HBT transistors [11][12], and were correlated to the output impedance mismatch of the transistor with the 50-Ohm electronics connected at his output. Therefore, we conducted measurement of this output impedance as shown in Fig. 3.

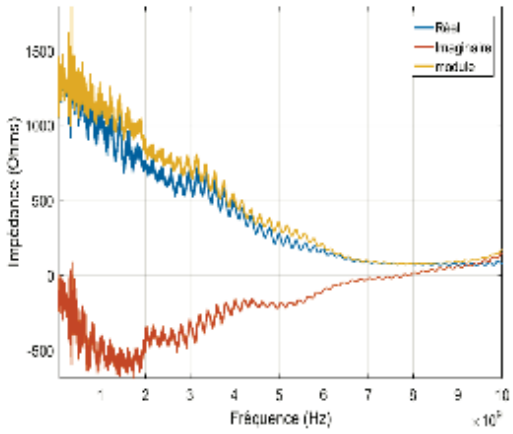

Fig. 3. RF output impedance of the transistor showing the strong impedance mismatch to 50-ohms electronics.

This figure shows the strong impedance mismatch, both for the real and imaginary parts of the transistor's output (collector–emitter). We could show that this mismatch was reduced as the base–collector biasing was increased. As done for the InGaAs/InP HBT [12], it is also possible to correlate the transistor's response to increasing modulation frequencies (Fig. 3) by extracting the transmitted power from the impedance measurement. This analysis shows that the transistor could be sufficiently adapted in broad frequency band to allow up to 10 Gbps communications.

As a conclusion for these preliminary studies of the SiGe transistor at THz frequencies, we have shown that these transistors present performances as THz detectors that are similar to other kinds of transistors, either in terms of structure (HEMT for example) or technology (GaAs or InGaAs for examples). We observed that the HBT structure requires careful impedance mismatch in the case of high-data-rate communications objectives. Further studies would be required to understand more precisely the anti-resonance response of the transistor at some specific modulation frequencies. If coupled to a THz antenna to increase the effective sensitivity of the detector, and coupled to an integrated amplifier to ease the impedance matching, such transistors could be attractive as detectors for THz communication in the next-generation wireless communication systems.

[1] T. Kleine-Ostmannand, T. Nagatsuma, “A review on terahertz communications research,” *Journal of Infrared, Millimeter, and Terahertz Waves*, vol. 32, no. 2, pp. 143–171, 2011
[2] A. Luukanen, L. Gröberg, M. Grönholm, P. Lappalainen, M. Leivo, A. Rautiainen, A. Tamminen, J. Ala-Laurinaho, C. R. Dietlein, and E. N. Grossman, “Real-time passive terahertz imaging system for standoff concealed weapons imaging,” in *Passive Millimeter-Wave Imaging Technology XIII*, vol. 7670. International Society for Optics and Photonics, 2010, p. 767004
[3] M. Tonouchi, “Cutting-edge terahertz technology,” *Nature photonics*, vol. 1, no. 2, p. 97, 2007
[4] https://ieeexplore.ieee.org/document/6713771
[5] https://ieeexplore.ieee.org/document/7733144
[6] https://www.epjap.org/articles/epjap/abs/2016/11/ap160302/ap160302.html
[7] R. Al Hadi, J. Grzyb, B. Heinemann, and U. Pfeiffer, “Terahertz detector arrays in a high-performance SiGe HBT technology,” in *Bipolar/BiCMOS Circuits and Technology Meeting (BCTM), 2012 IEEE*. IEEE, 2012, pp. 1–4.
[8] V. Vassilev, H. Zirath, R. Kozhuharov, and S. Lai, “140–220-GHz DHBT detectors,” *IEEE Transactions on Microwave Theory and Techniques*, vol. 61, no. 6, pp. 2353–2360, 2013
[9] N Dyakonova, D Coquillat, D But, C Consejo, F Teppe, W Knap,L Varani, S Blin, V Nodjiadjim, and A Konczykowska.Reducingnoise equivalent power in InP DHBT terahertz detector by biasingthe collector. In Noise and Fluctuations (ICNF), 2017 InternationalConference on, pages 1–4. IEEE, 2017
[10] https://www.worldscientific.com/doi/abs/10.1142/S0129156416400115
[1] https://jnrdm2019.sciencesconf.org/data/pages/proceedings.pdf
[2] http://www.theses.fr/s174753]

References

[1] Albert Van Der Ziel, *Noise in Solid State Devices and Circuits*. Wiley-Interscience, 1986.

[2] Alexander A. Balandin, *Noise and Fluctuations Control in Electronic Devices*. 2002.

[3] A. Van Der Ziel, A. H. Pawlikiewicz, X. Zhang, and X. Zhang, "Location of 1/f Noise Sources in BJT's and HBJT's—I. Theory," *IEEE Trans. Electron Devices*, vol. 33, no. 9, pp. 1371–1376, 1986, doi: 10.1109/T-ED.1986.22672.

[4] D. C. and J. S. Harris, "Low-Frequency Noise Properties of N-p-n AlGaAs/GaAs Heterojunction Bipolar Transistors," *IEEE Trans. Electron Devices*, vol. 39, no. 10, pp. 2383–2394, 1992, doi: 10.1109/16.158813.

[5] J. B. Johnson, "Thremal agitation of Electricity in Conductors," *Nature*, 1927.

[6] H. Nyquist, "Thermal agitation of electric charge in conductors," *Phys. Rev.*, vol. 32, no. 1, pp. 110–113, 1928, doi: 10.1103/PhysRev.32.110.

[7] A.Van Der Ziel and E.R.Chenette, "Noise ion solid State Devices," *ELSEVIER*, vol. 46, pp. 313–383, 1978.

[8] W. Schottky, "Über spontane Stromschwankungen in verschiedenen Elektrizitätsleitern," *Ann. Phys.*, vol. 362, pp. 541–567, 1918.

[9] A. Van der Ziel, "Theory of Shot Noise in Junction Diodes and Junction Transistors," *Proc. IRE*, vol. 43, no. 11, pp. 1639–1646, 1955, doi: 10.1109/JRPROC.1955.277990.

[10] G. Niu, "Noise in SiGe HBT RF technology: Physics, modeling, and circuit implications," *Proc. IEEE*, vol. 93, no. 9, pp. 1583–1597, 2005, doi: 10.1109/JPROC.2005.852226.

[11] R. E. Burgess, "The Statistics of Charge Carrier Fluctuations in Semiconductors," *Phys. Soc. Sect. B*, vol. 69, no. 10, 1956, doi: 10.1088/0370-1301/69/10/308.

[12] V. Mitin, L. Reggiani, and L. Varani, *Generation-Recombination Noise in Semiconductors*. American Scientific Publishers, 2002.

[13] U. J. Strasilla and M. J. 0. Strut, "Measurement of white and 1/ f noise within burst noise," *Proc. IEEE*, vol. 62, no. 12, pp. 1711–1713, 1974, doi: 10.1109/PROC.1974.9691.

[14] M. J. Kirton and M. J. Uren, "Noise in solid-state microstructures: A new perspective on individual defects, interface states and low-frequency 1/ f noise," *Adv. Phys.*, vol. 38, pp. 367–468, 1989, doi: 10.1080/00018738900101122.

[15] T. G. M. Kleinpenning, "On 1/ f noise and random telegraph noise in very small electronic devices," *Physica*, vol. 164, pp. 331–334, 1990, doi: 10.1016/0921-4526(90)90820-K.

[16] K.F.Knott, "Low energy electron beam investigation of planar transiston using scanning electron microscopy with particular reference to burst noise," *Noise Phys. Syst.*, pp. 97–99, 1981.

[17] M. J. Deen and F. Pascal, "Review of low-frequency noise behaviour of polysilicon emitter

bipolar junction transistors," *IEE Proceedings-Circuits, Devices Syst.*, pp. 125–137, 2004, doi: 10.1049/ip-cds.

[18] E. Simoen, S. Decoutere, A. Cuthbertson, C. L. Claeys, and L. Deferm, "Impact of polysilicon emitter interfacial layer engineering on the 1/f noise of bipolar transistors," *IEEE Trans. Electron Devices*, vol. 43, no. 12, pp. 2261–2268, 1996, doi: 10.1109/16.544419.

[19] T. G. M. Kleinpenning and A. H. De Kuijper, "Relation between variance and sample duration of 1/f noise signals," vol. 43, no. 1988, pp. 4–7, 2003, doi: 10.1063/1.340460.

[20] M. A. Caloyannides, "Microcycle spectral estimates of 1⁄f noise in semiconductors," vol. 307, 1974, doi: 10.1063/1.1662977.

[21] A. McWhorter, "1/f noise and germanium surface properties," *Semicond. Surf. Phys.*, pp. 207–208, 1957.

[22] F. Hooge and L. K. J. Vandamme, "Lattice scattering causes 1/f noise," *Phys. Lett. A*, vol. 66, no. 4, pp. 315–316, 1978, doi: 10.1016/0375-9601(78)90249-9.

[23] F. N. Hooge, T. G. M. Kleinpenning, and L. K. J. Vandamme, "Experimental Studies on 1/f Noise," *Reports Prog. Phys. 44(5)479*, vol. 44, no. 5, p. 479, 2000, doi: 10.1088/0034-4885/44/5/001.

[24] F. Hooge, "1/f noise sources," *IEEE Trans. Electron Devices*, vol. 41, no. 11, pp. 1926–1935, 1994, doi: 10.1109/16.333808.

[25] A.L.McWhorter, "1/f noise and related surface effects in germanium," 1955.

[26] F. N. Hooge, "1/f noise is no surface effect," *Phys. Lett. A*, vol. 29, no. 3, pp. 139–140, 1969, doi: 10.1016/0375-9601(69)90076-0.

[27] M. Sanden *et al.*, "Modeling the Variation of the Low-Frequency Noise in Polysilicon Emitter Bipolar Junction Transistors," *IEEE Electron Device Lett.*, vol. 22, no. 5, pp. 242–244, 2001, doi: 10.1109/55.919242.

[28] M. Sanden, O. Marinov, M. J. Deen, and M. Ostling, "A new model for the low-frequency noise and the noise level variation in polysilicon emitter bipolar junction transistors," *IEEE Trans. Electron Devices*, vol. 49, no. 3, pp. 514–520, 2002, doi: 10.1109/16.987124.

[29] M. Sanden, M. Ostling, O. Marrinov, and M. J. Deen, "Statistical simulations of the low-frequency noise and the noise level variation using a model based on generation-recombination centers," *Fluct. Noise Lett.*, pp. 51–60, 2001.

[30] V. Kumar and W. E. Dahlke, "Low frequency noise in Cr-SiO2-n-Si tunnel diodes," *IEEE Trans. Electron Devices*, vol. 24, pp. 146–153, 1977, doi: 10.1109/T-ED.1977.18694.

[31] N. Siabi-Shahrivar, W. Redman-White, P. Ashbum, and I. Post, "Modeling and characterization of Noise of Polysilicon Emitter Bipolar Transistors," *Bipolar Circuits Technol. Meet.*, pp. 236–238, 1990, doi: 10.1109/BIPOL.1990.171172.

[32] E. Zhao *et al.*, "An Investigation of Low-Frequency Noise in Complementary SiGe HBTs," *IEEE Trans. Electron Devices*, vol. 53, no. 2, pp. 329–338, 2006, doi:

10.1109/TED.2005.862698.

[33] M. J. Deen and E. Simoen, “Low-frequency noise in polysilicon-emitter bipolar transistors,” *Proc. - Circuits, Devices Syst.*, vol. 149, no. 1, 2002, doi: 10.1049/ip-cds:20020076.

[34] H. Markus and T. G. M. Kleinpenning, “Low-frequency noise in polysilicon emitter bipolar transistors,” *IEEE Trans. Electron Devices*, vol. 42, no. 4, pp. 720–726, 1995, doi: 10.1109/16.372077.

[35] J. D. Brunett and C. Hu, “Modeling hot-carrier effects in polysilicon emitter bipolar transistors,” *IEEE Trans. Electron Devices*, vol. 35, no. 12, pp. 2238–2244, 1988, doi: 10.1109/16.8798.

[36] A. Mounib *et al.*, “Low frequency (1 / f) noise model for the base current in polysilicon emitter bipolar junction transistors,” *Appl. Phys.*, vol. 3330, no. 1996, 1999, doi: 10.1063/1.361233.

[37] E. Zhao, Z. Celik-Butler, F. Hiel, and R. Dutta, “Temperature dependence of 1/f noise in polysilicon emitter bipolar transistors,” *IEEE Trans. Electron Devices*, vol. 49, no. 12, pp. 2230–2236, 2002.

[38] Y. Zhuang and Q. Sun, “Correlation Between 1/f Noise and hFE Long-Term Instability in Silicon Bipolar Devices,” *IEEE Trans. Electron Devices*, vol. 38, no. 1, pp. 2540–2547, 1991, doi: 10.1109/16.97420.

[39] N. Siabi-Shahrivar, W. Redman-Whit, P. Ashburn, and H. A. Kemhadjian, “Reduction of 1/f noise in polysilicon emitter bipolar transistors,” *Solid-State Electron*, vol. 38, no. 2, pp. 389–400, 1995, doi: 10.1016/0038-1101(94)00126-Z.

[40] T. Kleinpenning, “1/f Noise in pn diodes,” *Phys. B+C*, vol. 98, pp. 289–299, 1980, doi: 10.1016/0378-4363(80)90045-5.

[41] S. M. Kogan and K. Nagaev, “On the low-frequency current 1/f noise in metals,” *Solid States Communcations*, vol. 49, no. 4, pp. 387–389, 1984, doi: 10.1016/0038-1098(84)90593-3.

[42] J. Pelz and J. Clarke, “Quantitative" local-interference" model for 1 f noise in metal films,” *Phys. Rev. B*, vol. 36, no. 8, p. 4479, 1987, doi: 10.1103/PhysRevB.36.4479.

[43] T. Kleinpenning, “1/f mobility fluctuations in pin and p-v-n diodes,” *Phys. B Condens. Matter*, vol. 154, no. 1, pp. 27–34, 1988, doi: 10.1016/0921-4526(88)90014-2.

[44] A. Van der Ziel, “Unified presentation of 1/f noise in electron devices: fundamental 1/f noise sources,” *Proc. IEEE*, vol. 76, no. 3, pp. 233–258, 1988, doi: 10.1109/5.4401.

[45] N. Valdaperez, “Etude des caractéristiques statiques et du bruit basse fréquence de transistors bipolaires NPN intégrés dans des procédés BiCMOS haute fréquence à simple et double polysilicium,” Caen Uniersity, 2002.

[46] E. Simoen, S. Decoutere, C. Claeys, and L. Deferma, “A global description of the base current 1/f noise of polysilicon emitter bipolar transistors before and after hot-carrier stress,” *Solid State Electron.*, vol. 42, no. 9, pp. 1679–1687, 1998, doi: doi.org/10.1016/S0038-

1101(98)00131-2.

[47] A. Pawlikiewicz and A. Van der Ziel, “Location of 1/f noise sources in BJT’s—II. Experiment,” *IEEE Trans. Electron Devices*, vol. 34, no. 9, pp. 2009–2012, 1987, doi: 10.1109/T-ED.1987.23188.

[48] T. G. Kleinpenning, “Low-frequency noise in modern bipolar transistors: impact of intrinsic transistor and parasitic series resistances,” *IEEE Trans. Electron Devices*, vol. 41, no. 11, pp. 1981–1991, 1994, doi: 10.1109/16.333815.

[49] K. Kandiah, “Low Frequency Noise Mechanisms in Field Effect Transistors,” *ELSEVIER*, pp. 19–25, 1985, doi: 10.1016/B978-0-444-86992-0.50008-4.

[50] M. J. Deen and O. Marinov, “Noise in advanced electronic devices and circuits,” *AIP Conf. Proc.*, vol. 780, no. 1, 2005, doi: 10.1063/1.2036687.

[51] J. Vildeuil, M. Valenza, and D. Rigaud, “CMOS 1/f noise modelling and extraction of BSIM3 parameters using a new extraction procedure,” *Microelectron. Test Struct.*, pp. 206–211, 1999, doi: 10.1109/ICMTS.1999.766244.

[52] M. J. Deen, S. L. Rumyantsev, and M. Schrote, “On the origin of 1 / f noise in polysilicon emitter bipolar transistors,” vol. 1192, pp. 13–17, 1999, doi: 10.1063/1.369256.

[53] J. Raoult, F. Pascal, C. Delseny, M. Marin, and M. J. Deen, “Impact of carbon concentration on 1 ⁄ f noise and random telegraph signal noise in SiGe : C heterojunction bipolar transistors,” *J. Appl. Phys.*, vol. 114508, no. 2008, 2012, doi: https://doi.org/10.1063/1.2939252.

[54] M. Mihaila, “1/f, g-r and burst noise induced by emitter-edge dislocations in bipolar transistors,” *Solid. State. Electron.*, vol. 27, no. 7, pp. 675–676, 1984, doi: 10.1016/0038-1101(84)90138-2.

[55] T. G. M. Kleinpenning, “On 1f mobility fluctuations in bipolar transistors,” *Phys. B+C*, vol. 138, no. 3, pp. 244–252, 1986, doi: 10.1016/0378-4363(86)90003-3.

[56] Y. Dai, “Deep-level impurity analysis for p-n junctions of a bipolar transistor from low-frequency G-R noise measurements,” *Solid. State. Electron.*, vol. 32, no. 2, pp. 439–443, 1989, doi: 10.1016/0038-1101(89)90025-7.

[57] Y. Dai, “Generation-recombination noise in bipolar transistors,” *Microelectron. Reliab.*, vol. 41, no. 6, pp. 919–925, 2001, doi: 10.1016/S0026-2714(01)00042-7.

[58] C. Delseny, A. Penarier, F. Pascal, S. G. Jarrix, and P. Llinares, “Comparison of low frequency noise and high frequency performances of double and simple polysilicon BiCMOS BJT,” *Microelectron. Reliab.*, vol. 40, pp. 1869–1874, 2000, doi: 10.1016/S0026-2714(00)00069-X.

[59] J. D. Cressler, L. Vempati, J. A. Babcock, R. C. Jaeger, and D. L. Harame, “Low-frequency noise characteristics of UHV/CVD epitaxial Si-and SiGe-base bipolar transistors,” *IEEE Electron Device Lett.*, vol. 17, no. 1, pp. 13–15, 1996, doi: 10.1109/55.475562.

[60] D. Quon, G. Sonek, and G. Li, “1/f noise characterization of base current and emitter

interfacial oxide breakup in npn polyemitter bipolar transistors," *IEEE Electron Device Lett.*, vol. 15, no. 10, pp. 430–432, 1994, doi: 10.1109/55.320991.

[61] A. Mounib *et al.*, "Low-frequency noise sources in polysilicon emitter BJT's: influence of hot-electron-induced degradation and post-stress recovery," *IEEE Trans. Electron Devices*, vol. 42, no. 9, pp. 1647–1652, 1995, doi: 10.1109/16.405279.

[62] N. Siabi-Shahrivar, W. Redman-White, P. Ashburn, and H. A. Kemhadjian, "Reduction of 1f noise in polysilicon emitter bipolar transistors," *Solid State Electron.*, vol. 38, no. 2, pp. 389–400, 1995, doi: 10.1016/0038-1101(94)00126-Z.

[63] J. Q. Lü and F. Koch, "Random telegraph noise in advanced self-aligned bipolar transistors," *Jpn. J. Appl. Phys.*, vol. 35, p. 826, 1996, doi: 10.1143/JJAP.35.826.

[64] D. Pogany, A. Chantre, and J. A. Chroboczek, "Origin of large-amplitude random telegraph signal in silicon bipolar junction transistors after hot carrier degradation," *Appl. Phys. Lett.*, vol. 68, no. 4, p. 541, 1996, doi: https://doi.org/10.1063/1.116393.

[65] J. Deen, S. Rumyantsev, R. Bashir, and R. Taylor, "Measurements and comparison of low frequency noise in npn and pnp polysilicon emitter bipolar junction transistors," *J. Appl. Phys.*, vol. 84, no. 1, 1998, doi: 10.1063/1.368066.

[66] M. J. Deen and S. Rumyantsev, "Low frequency noise in complementary npn and pnp polysilicon emitter bipolar junction transistors," *Microelectron. Reliab.*, vol. 40, no. 11, pp. 1855–1861, 2000, doi: 10.1016/S0026-2714(00)00090-1.

[67] M. J. Deen, "Low frequency noise in silicon-based devices, circuits and systems," *22nd Int. Conf. Noise Fluctuations*, pp. 1–5, 2013, doi: 10.1109/ICNF.2013.6578876.

[68] R. Plana, J. P. Roux, L. Escotte, J. Graffeuil, A. Gruhle, and H. Kibbel, "Low-Frequency Noise Properties of Si/SiGe Heterojunction Bipolar Transistors," *24th Eur. Solid State Device Res. Conf.*, pp. 481–484, 1994.

[69] R. Plana, L. Escotte, J. P. Roux, J. Graffeuil, A. Gruhle, and H. Kibbel, "l/f Noise in Self-Aligned Si/SiGe Heterojunction Bipolar Transistor," *IEEE Electron Device Lett.*, vol. 16, no. 2, pp. 58–60, 1995, doi: 10.1109/55.386028.

[70] L. S. Vempati, J. D. Cressler, J. A. Babcock, R. C. Jaeger, and D. L. Harame, "Low-frequency noise in UHV/CVD epitaxial Si and SiGe bipolar transistors," *solid state circuits*, vol. 31, no. 10, pp. 1458–1467, 1996, doi: 10.1109/4.540056.

[71] Z. Jin *et al.*, "1/f Noise in Proton-Irradiated SiGe HBTs," *IEEE Trans. Nucl. Sci.*, vol. 48, no. 6, pp. 2244–2249, 2001, doi: 10.1109/23.983203.

[72] A. K. Sutton *et al.*, "An Investigation of Dose Rate and Source Dependent Effects in 200 GHz SiGe HBTs," *IEEE TRASACTION Nucl. Sci.*, vol. 53, no. 6, pp. 3166–3174, 2006, doi: 10.1109/TNS.2006.885382.

[73] R. Gabl, K. Aufinger, J. Bock, and T. F. Meister, "Low-Frequency Noise Characteristics of Advanced Si and SiGe Bipolar Transistors," *ESSDERC*, 1997.

[74] P. O. Staffan, L. K. J. Vandamme, and A. Rydberg, "Measurement of Low-Frequency Base

and Collector Current Noise and Coherence in SiGe Heterojunction Bipolar Transistors Using Transimpedance Amplifiers," *IEEE Trans. Electron Devices*, vol. 46, no. 5, pp. 993–1000, 1999, doi: 10.1109/16.760408.

[75] S. Bruce, L. K. J. Vandamme, and A. Rydberg, "Improved correlation measurements using voltage and transimpedance amplifiers in low-frequency noise characterization of bipolar transistors," *IEEE Trans. Electron Devices*, vol. 47, no. 9, pp. 1772–1773, 2000, doi: 10.1109/16.861592.

[76] Z. Jin et al, "Impact of geometrical scaling on low-frequency noise in SiGe HBTs," *IEEE Trans. Electron Devices*, vol. 50, no. 3, pp. 676–682, 2003, doi: 10.1109/TED.2003.810483.

[77] E. Zhao, J. D. Cressler, M. El-Diwany, T. Krakowski, A. Sadovnikov, and D. Kokoski, "On the Geometrical Dependence of Low-Frequency Noise in SiGe HBTs," *Solid. State. Electron.*, vol. 50, no. 11–12, pp. 1748–1755, 2006, doi: 10.1016/j.sse.2006.09.018.

[78] F. Pascal, C. Chay, M. J. Deen, S. G. Jarrix, C. Delseny, and A. Pénarier, "Comparison of low frequency noise in III-V and Si/SiGe HBTs," *IEEE Proc. Circuits Devices Syst*, vol. 151, no. 2, pp. 138–146, 2004, doi: 10.1049/ip-cds:20040505.

[79] J. A.Johansen and Z. Jin et al, "On the scaling limits of low-frequency noise in SiGe HBTs," *Solid State Electron.*, vol. 48, pp. 1897–1900, 2004, doi: 10.1016/j.sse.2004.05.032.

[80] L. Militarua, A. Souifia, M. Mouisab, and G. Brémonda, "RTS noise in submicron SiGe epitaxial base bipolar transistors," *Microelectron. Reliab.*, vol. 40, no. 8–10, pp. 1585–1590, 2000, doi: 10.1016/S0026-2714(00)00143-8.

[81] M. Von Haartman, M. Sandén, M. Östling, and G. Bosman, "Random telegraph signal noise in SiGe heterojunction bipolar transistors," *J. Appl. Phys.*, vol. 92, no. 8, pp. 4414–4421, 2002, doi: 10.1063/1.1506197.

[82] C. Mukherjee *et al.*, "Random telegraph noise in SiGe HBTs: Reliability analysis close to SOA limit," *Microelectron. Reliab.*, vol. 73, pp. 146–152, 2017, doi: 10.1016/j.microrel.2017.05.001.

[83] P. Cheng *et al.*, "An Investigation of Low-Frequency and Phase Noise in Complementary SiGe HBTs on SOI," *IEEE Bipolar/BiCMOS Circuits Technol. Meet.*, pp. 165–168, 2010, doi: 10.1109/BIPOL.2010.5667937.

[84] M.Seif *et al.*, "Dispersion study of DC and Low Frequency Noise in SiGe:C Heterojunction Bipolar Transistors used for mm-Wave to Terahertz applications," *Microelectron. Reliab.*, vol. 54, no. 9–10, pp. 2171–2175, 2014, doi: 10.1016/j.microrel.2014.07.027.

[85] C. T. Coen, A. Ildefonso, Z. E. Fleetwood, and J. D. Cressler, "A 19-34 GHz SiGe HBT Square-Law Detector with Ultra-Low 1/f Noise for Atmospheric Radiometers," *12th Eur. Microw. Integr. Circuits Conf.*, pp. 163–166, 2017, doi: 10.23919/EuMIC.2017.8230685.

[86] C. Mukherjee *et al.*, "Low-Frequency Noise in Advanced SiGe : C HBTs — Part I : Analysis," *IEEE Trans. Electron Devices*, vol. 63, no. 9, pp. 3649–3656, 2016, doi: 10.1109/TED.2016.2589159.

[87] J. ElBeyrouthy *et al.*, *European Microwave Week 2019 - EuMW 2019, 29th Sept – 4th Oct*

2019, Paris (France). .

[88] T. G. M. Kleinpenning, "Low-Frequency Noise in Modern Bipolar Transistors: Impact of Intrinsic Transistor and Parasitic Series Resistances," *IEEE Trans. Electron Devices*, vol. 41, no. 11, pp. 1981–1991, 1994, doi: 10.1109/16.333815.

[89] M. J. Deen and F. Pascal, "Electrical characterization of semiconductor materials and devices — review," pp. 549–575, 2006, doi: 10.1007/s10854-006-0001-8.

[90] F. Pascal, J. Raoult, B. Sagnes, A. Hoffmann, S. Haendler, and G. Morin, "Improvement of 1/f noise in advanced 0.13 m BiCMOS SiGe:C Heterojunction Bipolar Transistors," *Proc. IEEE 21st Int. Conf. Noise Fluctuations, ICNF 2011*, pp. 279–282, 2011, doi: 10.1109/ICNF.2011.5994321.

[91] G. Avenier and P. Chevalier et al., "0 . 13µm SiGe BiCMOS Technology for mm-Wave Applications," *IEEE Bipolar/BiCMOS Circuits Technol. Meet.*, pp. 89–92, 2008, doi: 10.1109/BIPOL.2008.4662719.

[92] E.CANDERLE, "Etudes et developpement de transistirs bipolaires Si/SiGe:C rapides dans un noeud BiCMOS 55 nm," Lille University, 2014.

[93] P. Chevalier *et al.*, "A 55 nm Triple Gate Oxide 9 Metal Layers SiGe BiCMOS Technology Featuring 320 GHz f T / 370 GHz f MAX HBT and High-Q Millimeter-Wave Passives," *IEEE Int. Electron Devices Meet.*, pp. 77–79, 2014, doi: 10.1109/IEDM.2014.7046978.

[94] A. Gauthier, P. Chevalier, G. Avenier, G. Ribes, M. Rellier, and Y. Campidelli, "SiGe HBT / CMOS Process Thermal Budget Co-optimization in a 55-nm CMOS Node," *IEEE Bipolar/BiCMOS Circuits Technol. Meet.*, pp. 58–61, 2017, doi: 10.1109/BCTM.2017.8112911.

[95] S. M. Sze and K. K. Ng, *Physics of semiconductor devices: John Wiley & Sons*. 2006.

[96] W. Shockleyt, "Carrier Generation and Recombination in P-N Junctions and P-N Junction Characteristics," *Proc. IRE*, vol. 45, no. 9, pp. 1228–1243, 1956, doi: 10.1109/JRPROC.1957.278528.

[97] S. A. Campbell, *The science and engineering of microelectronic fabrication*. Oxford University Press, 2001.

[98] M. Sandén, O. Marinov, M. J. Deen, and M. Östling, "A New Model for the Low-Frequency Noise and the Noise Level Variation in Polysilicon Emitter BJTs," *IEEE Trans. Electron Devices*, vol. 49, no. 3, pp. 514–520, 2002, doi: 10.1109/16.987124.

[99] F. Pascal, J. Raoult, C. Delseny, P. Benoit, M. Marin, and M. J. Deen, "Impact of Technological Parameters on the Low Frequency Noise of Advanced Heterojunction Bipolar Transistors," *AIP Conf. Proc.*, vol. 922, no. 1, pp. 77–83, 2007, doi: 10.1063/1.2759640.

[100] C. Theodorou and G. Ghibaudo, "Low - frequency Noise and Random Telegraph Noise in Nanoscale Devices : Modeling and Impact on Circuit Operation," *ICNF Conf.*, pp. 1–4, 2019.

[101] M. Seif *et al.*, “Study of low frequency noise in advanced SiGe : C heterojunction bipolar transistors,” *44th Eur. Solid State Device Res. Conf.*, pp. 373–376, 2014, doi: 10.1109/ESSDERC.2014.6948838.

[102] F. Pascal, J. Raoult, C. Delseny, P. Benoit, M. Marin, and M. J. Deen, “Impact of Technological Parameters on the Low Frequency Noise of Advanced Heterojunction Bipolar Transistors,” *19th Int. Conf. Noise Phys. Syst. 1/f Fluctuations, Tokyo, Japan*, vol. 77–82, 2007.

[103] M. J. Deen, S. L. Rumyantsev, and M. Schroter, “Low Frequency Noise Behavior of Polysilicon Emitter Bipolar Junction Transistors - A Review,” *Noise in devices and circuits*, vol. 5113, pp. 1–5, 2003, doi: 10.1117/12.488850.

[104] J. Tang *et al.*, “Modeling and Characterization of SiGe HBT Low-Frequency Noise Figures-of-Merit for RFIC Applications,” *IEEE Trans. Microw. Theory Tech.*, vol. 50, no. 11, pp. 2467–2473, 2002, doi: 10.1109/TMTT.2002.804519.

[105] M. Seif, “Caractérisation et modélisation des sources de bruit BF dans les transistors bipolaires développés en technologie BiCMOS (sub 0 . 13 µm) pour application RF et THz,” pp. 79–81, 2015.

[106] F. M. Puglisi, L. Larcher, P. Pavan, and S. Member, “Mixed-Mode Stress in Silicon – Germanium Heterostructure Bipolar Transistors : Insights From Experiments and Simulations,” *IEEE Trans. Device Mater. Reliab.*, vol. 19, no. 2, pp. 275–282, 2019, doi: 10.1109/TDMR.2019.2912853.

[107] M. N. Tutt, D. Pavlidis, A. Khatibzadeh, and B. Bayraktaroglu, “Low Frequency Noise Characteristics of Self-Aligned AIGaAs/GaAs Power Heterojunction Bipolar Transistors,” *IEEE Trans. Electron Devices*, vol. 42, no. 2, pp. 219–229, 1995, doi: 10.1109/16.370076.

[108] M. Bouslama *et al.*, “Dynamic Performance and Characterization of Traps Using Different Measurements Techniques for the New AlGaN/GaN HEMT of 0.15-µm Ultrashort Gate Length,” *IEEE Trans. Microw. Theory Tech.*, vol. 67, no. 7, pp. 2475–2482, 2019, doi: 10.1109/TMTT.2019.2907540.

[109] M. Bouslama, J. C. Nallatamby, and M. Prigent, “Trapping Investigation of the GaN HEMT Devices Using the Low Frequency Noise Characterization,” *25th Int. Conf. Noise Fluctuations*, 2019.

[110] C. Delsen, F. Pascal, S. Jarrix, G. Lecoy, J. Dangla, and C. Dubon-Chevallier, “Excess noise in AlGaAs/GaAs heterojunction bipolar transistors and associated TLM test structures,” *IEEE Trans. Electron Devices*, vol. 41, no. 11, pp. 2000–2005, 1994, doi: 10.1109/16.333817.

[111] A. D. va. Rheenen, G. Bosman, and R. J. J. Zijlstra, “Low frequency noise measurements as a tool to analyze deep-level impurities in semiconductor devices,” *Solid. State. Electron.*, vol. 30, no. 3, pp. 259–265, 1987, doi: https://doi.org/10.1016/0038-1101(87)90181-X.

[112] J. D. Cressler, “SiGe BiCMOS Technology: An IC Design Platform for Extreme Environment Electronics Applications,” *IEEE Int. Reliab. Phys. Symp. Proc.*, pp. 141–149, 2007, doi: 10.1109/RELPHY.2007.369883.

[113] Rask J. et al., “Space Faring: The Radiation Challenge Introduction and Module 1: Radiation Educator Guide.,” *Natl. Aeronaut. Sp. Adm.*, 2008.

[114] “https://watchers.news/2011/11/05/a-guide-for-solar-watchers-pt-1/?replytocom=21991.” .

[115] “http://WWW.sec.noaa.gov, Space Environment Center of Boulder.” .

[116] F. Berghmans et al., “An introduction to radiation effects on optical components and fiber optic sensorsin Optical waveguide sensing and imaging,” *Springer*, pp. 127–165, 2008.

[117] Poivey C., “TNID Total Non Ionizing Dose or DD Displacement Damage.,” *2017. ESA–CERN–SCC Work.*

[118] V. N. Hegde *et al.*, “A Comparison of Electron , Proton and Gamma Irradiation Effects on the I-V Characteristics of 200 GHz SiGe HBTs,” *IEEE Trans. Device Mater. Reliab.*, vol. 18, no. 4, pp. 592–598, 2018, doi: 10.1109/TDMR.2018.2875064.

[119] J. D. Cressler and G. Niu, *Silicon-Germanium Heterojunction Bipolar Transistors*. Norwood, MA, USA: Artech House, 2003.

[120] D. Duan-Lee Tang and E. Hackbarth, “Junction Degradation in Bipolar Transistors and the Reliability Imposed Constraints to Scaling and Design,” *IEEE Trans. Electron Devices*, vol. 35, no. 12, pp. 2101–2107, 1988, doi: 10.1109/16.8783.

[121] A. B. Joshi and D. L. Kwong, “Dependence of radiation induced damage on gate oxide thickness in MOS capacitors with ultrathin gate oxides,” *Electron. Lett.*, vol. 28, no. 8, pp. 744–746, 1992, doi: 10.1049/el:19920471.

[122] M. Seif et al., “Characterization , modeling and comparison of 1/f noise in Si/SiGe:C HBTs issued from three advanced BiCMOS technologies,” *29th Int. Conf. Microelectron.*, pp. 1–4, 2017, doi: 10.1109/ICM.2017.8268847.

[123] B. Van Haaren *et al.*, “Low-Frequency Noise Properties of SiGe HBT’s andApplication to Ultra-Low Phase-Noise Oscillators,” *IEEE Trans. Microw. Theory Tech.*, vol. 46, no. 5, pp. 647–652, 1998, doi: 10.1109/22.668677.

[124] A. Van der Ziel, “Formulation of surface 1/*f* noise processes in bipolar junction transistors and in p−n diodes in Hooge-type form,” *Solid State Electron.*, vol. 32, no. 1, pp. 91–93, 1989, doi: https://doi.org/10.1016/0038-1101(89)90053-1.

[125] E. Zhao *et al.*, “The Effects of Radiation on 1/f Noise in Complementary (npn + pnp) SiGe HBTs,” *IEEE Trans. Nucl. Sci.*, vol. 51, no. 6, pp. 3243–3249, 2004, doi: 10.1109/TNS.2004.839138.

[126] S. C. Witczakl *et al.*, “Hardness assurance testing of bipolar junction transistors at elevated irradiation temperatures,” *IEEE Trans. Nucl. Sci.*, vol. 44, no. 6, pp. 1989–2000, 1997, doi: 10.1109/23.658978.

[127] D. M. Fleetwood, F. V. Thome, S. Tsao, P. V. Dressendorfer, and J. Schwank, “High-temperature silicon-on-insulator electronics for space nuclear power systems: requirements and feasibility,” *IEEE Trans. Nucl. Sci.*, vol. 35, no. 5, pp. 1099–1112, 1988, doi: 10.1109/23.7506.

[128] N. H. Vinayakprasanna, K. C. Praveen, N. Pushpa, J. D. Cressler, and A. P. G. Prakash, “A comparison of 100 MeV oxygen ion and 60 Co gamma irradiation effects on advanced 200 GHz SiGe heterojunction bipolar transistors,” *Indian J. Phys.*, vol. 89, 2015, doi: 10.1007/s12648-015-0654-3.

[129] S. M. S. J H. Hubbell, “Tables of X-Ray Mass Attenuation Coefficients and Mass Energy-Absorption Coefficients 1 keV to 20 MeV for Elements Z = 1 to 92 and 48 Additional Substances of Dosimetric Interest,” *Natl. Inst. Stand. Technol. Gaithersburg, MD*, 1995.

[130] P. Benoit *et al.*, “Dc and low frequency noise analysis of hot-carrier induced degradation of low complexity 0.13 µm CMOS bipolar transistors,” *Microelectron. Reliab.*, vol. 45, pp. 1800–1806, 2005, doi: https://doi.org/10.1016/j.microrel.2005.07.097.

[131] U. Gogineni, J. D. Cressler, G. Niu, and D. L. Harame, “Hot Electron and Hole Degradation of UHV/CVD SiGe HBT’s,” *IEEE Trans. Electron Devices*, vol. 47, no. 7, pp. 1440–1447, 2000, doi: 10.1109/16.848289.

[132] D. M. Fleetwood, S. T. Pantelides, and R. Schrimpf, *Defects in microelectronic materials and devices*. 2008.

[133] M. Couret *et al.*, “Scalable compact modeling of trap generation near the EB spacer oxide interface in SiGe HBTs,” *Solid. State. Electron.*, vol. 169, 2020, doi: 10.1016/j.sse.2020.107819.

[134] H. Kamrani, D. Jabs, V. D’Alessandro, N. Rinaldi, and C. Jungemann, “Physics-based hot-carrier degradation model for SiGe HBTs,” *Int. Conf. Simul. Semicond. Process. Devices*, pp. 341–344, 2016, doi: 10.1109/SISPAD.2016.7605216.

Publications

"Characterization, modeling and comparison of 1/f noise in Si/SiGe:C HBTs issued from three advanced BiCMOS technologies ", M. Seif, F. Pascal, B. Sagnes, J. El Beyrouthy, A.Hoffmann, S. Haendler, P. Chevalier, D. Gloria, 29th International Conference on Microelectronics - ICM 2017 - Beyrouth (Liban) (10^{th} - 13^{th} December 2017) proceedings IEEE 978-1-5386-4049-4/17

"Localization of 1/f noise sources in Si/SiGe:C HBTs", M. Seif, F. Pascal, B. Sagnes, J. El Beyrouthy, A.Hoffmann, S. Haendler, P. Chevalier, D. Gloria, 8th International Conference on Unsolved Problems on Noise - UPON 2018 - Gdansk (Pologne) (9^{th} - 13^{th} July 2018)

"Low frequency Noise Characterization and Modeling of HBTs developed in 55 nm BiCMOS technology for three collector architectures", J. El Beyrouthy, B. Sagnes, P. Fabien, A. Hoffmann, S. Haendler, P. Chevalier, D. Gloria, Journées Nationales du Réseau Doctoral en Micro-nanoélectronique 2019- JNRDM 2019, 3^{rd} – 5^{th} June 2019, Montpellier (France)

"Low frequency noise characterization and modeling of SiGe HBT featuring LASER annealing in a 55-nm CMOS node", J. El Beyrouthy, A. Vauthelin, B. Sagnes, F. Pascal, A.Hoffmann, M. Valenza, S. Haendler, A. Gauthier, P. Chevalier, D. Gloria, 25th International Conference on Noise and Fluctuations - ICNF 2019 - Neuchâtel (Suisse) (18^{th} – 21^{st} June 2019) proceedings DOI 10.5075-epfl-ICLAB-ICNF-269248

"Effects of Total Ionizing Dose on I-V and Low Frequency Noise characteristics in advanced Si/SiGe:C Heterojunction Bipolar Transistors ", J. El Beyrouthy, A. Vauthelin, M. Seif, B. Sagnes, F. Pascal, A.Hoffmann, M. Valenza, J. Boch, T. Maraine, S. Haendler, A. Gauthier, P. Chevalier, D. Gloria, 30th European Conference on Radiation and its Effects on Components and Systems - RADECS 2019 - Montpellier (France) (16^{th} – 20^{th} September 2019) proceedings to be published

"Low Frequency Noise modelling of BiCMOS SiGe HBTs", Johnny El Beyrouthy, Alexandre Vauthelin, Marcelino Seif, Bruno Sagnes, Alain Hoffmann, Matteo Valenza, Sébastien Haendler, Alexis Gauthier, Pascal Chevalier, Daniel Gloria, Fabien Pascal, Workshop Recent advances in SiGeBiCMOS: technologies, modelling & circuits for 5G, radar & imaging, European Microwave Week 2019 - EuMW 2019, 29^{th} Sept – 4^{th} Oct 2019, Paris (France)

“Impact of Gamma irradiation on advanced Si/SiGe:C BiCMOS technology: comparison versus X-ray”, J. El Beyrouthy, B. Sagnes, F. Pascal, M. Elsherif, J. Boch, T. Maraine, S. Haendler,

P. Chevalier, D. Gloria, 31st European Conference on Radiation and its Effects on Components and Systems - RADECS 2020 - (19th October-20th November 2020)

Abstract:

In this thesis, Si/SiGe:C heterojunction bipolar transistors (HBTs) issued from BiCMOS technologies developed for RF, THz and mm-wave applications are investigated. The BiCMOS technology (B55) studied in this work is based on a 55 nm CMOS node and is compared to a previous mature generation (BiCMOS9MW) developed on a 130 nm CMOS node. The main objective of this work is to investigate the impact of X-ray and Gamma-ray irradiations on these devices through Low Frequency Noise measurements. LFN study is considered as a highly sensitive and non-destructive measurement technique to investigate the technological development from a generation to another. Technological developments of the B55 technology, collector structures and Emitter-Base dopant activation techniques, are investigated on both DC and excess noises: forward Gummel plots, 1/f noise and Generation-Recombination components respectively. Compact models are extracted for the two excess noise components, the suspected areas of the associated noise sources are located at the E-B surface and periphery. The degradations induced by X-ray and Gamma-ray on both DC measurements (excess Base current) and LFN ones (1/f noise and G-R components) are examined in function of the Total Ionizing Dose (TID). The main result is the higher tolerance of the B55 technology. Moreover, by studying the effects versus base current and geometrical parameters, compact models are developed classically for 1/f noise and, in more innovative ways, for G-R component. The induced LFN sources are suggested to be located in the vicinity of the spacer and STI oxides. A healing effect after annealing processes is also brought to the fore.

Résumé:

Durant cette thèse, des transistors bipolaires à hétérojonction Si/SiGe:C (HBTs) issus de technologies BiCMOS développées pour des applications RF, THz et mm-wave sont étudiés. La principale technologie étudiée dans ce travail, BiCMOS B55, est basée sur un nœud CMOS 55 nm et elle est comparée à une génération plus mature BiCMOS9MW développée sur un nœud CMOS 130 nm. L'objectif principal de ces travaux est d'analyser l'impact des rayonnements X et Gamma sur ces composants par des mesures de bruit basse fréquence. Le bruit basse fréquence est une technique de mesure très sensible et non destructive utilisée comme indicateur de qualité et de performance durant le développement technologique. Les effets de certains paramètres technologiques de la filière B55, comme différentes structures de Collecteur et deux techniques d'activation des dopants de la jonction Emetteur-Base, sont étudiés à la fois sur les mesures DC et sur les composantes de bruit en excès : courbes de Gummel, bruit en 1/f et composantes de Génération-Recombination. A partir de la modélisation compacte du bruit basse fréquence, les sources de bruits associées sont localisées à la surface et à la périphérie de la jonction E-B. Ensuite, les effets induits par les rayonnements X et Gamma sur les mesures DC (courant de base excédentaire) et LFN (bruit en 1/f et composantes G-R) sont étudiés en fonction de la dose ionisante cumulée (TID). Le principal résultat est la tolérance aux irradiations plus élevée de la technologie B55. De plus, l'analyse de ces effets par rapport au courant de base et aux paramètres géométriques a permis de développer des modèles compacts, de manière classique pour le bruit en 1/f et de manière plus innovante pour les composantes G-R. Il est suggéré que les sources de bruit induites par les irradiations soient situées à proximité des oxydes spacer et STI. Enfin, un effet de guérison par recuit thermique des défauts générés est également mis en évidence.